THE DRY DEPOSITION OF MERCURY

INTO THE GREAT SALT LAKE

by

Joel R. Lisonbee

A thesis submitted to the faculty of
The University of Utah
in partial fulfillment of the requirements for the degree of

Master of Science

Department of Atmospheric Sciences

The University of Utah

December 2010

The University of Utah Graduate School

STATEMENT OF THESIS APPROVAL

The thesis of **Joel R. Lisonbee**

has been approved by the following supervisory committee members:

Kevin D. Perry	, Chair	**8 July 2010** Date Approved
John D. Horel	, Member	**8 July 2010** Date Approved
Eric Pardyjak	, Member	**8 July 2010** Date Approved

and by **W. James Steenburgh**, Chair of the Department of **Atmospheric Sciences**

and by Charles A. Wight, Dean of The Graduate School.

ABSTRACT

The Great Salt Lake (GSL) in the western United States has been identified as the most mercury laden body of water in the United States with a median water mercury concentration of 42 ng L^{-1}. When Hg enters an aquatic ecosystem, it can be converted to the toxic organic mercury compound, methylmercury. Methylmercury bioaccumulates up the food chain and has been the cause of consumption advisories for game fish in many lakes and rivers in the historically pristine Intermountain West. In 2005, the Utah Department of Health and the Fish and Wildlife Service placed a similar consumption advisory on waterfowl on the GSL. The primary goal of this study is to identify the pathway of greatest influx of Hg pollution to the GSL to give insight toward the source and an eventual solution to the Hg pollution problem.

Speciated atmospheric mercury measurements were collected at a field site on the eastern shore of the GSL for a 1-year period beginning on July 1, 2009. These atmospheric mercury concentrations, along with turbulence measurements, were used as input to a resistance-in-series dry deposition model (based on Wesley and Hicks 1977). The dry deposition flux of mercury was determined from the modeled dry deposition velocity and the measured concentrations. This dry deposition flux was compared to the wet deposition flux measured by the National Deposition Network and the riverine influx measured by the USGS.

It was found that in the 1 year from July 1, 2009 through June 30, 2010, 10.7 $\mu g\, m^{-2}$ of Hg was deposited into the GSL by dry deposition from the atmosphere. Dry deposition makes up 60% of the total Hg influx from all measured pathways. The flux from the dry deposition of the global background pool of Hg ($1.5 \pm 0.2\, ng\, m^{-2}$) dominated the dry deposition flux, making up 82.5±8.5% of the dry deposition flux and 50% of the total Hg influx to the GSL. Lake sediment cores from the GSL suggest a much larger annual flux of between 55 $\mu g\, m^{-2}$and 150 $\mu g\, m^{-2}$. This discrepancy may suggest that measurements of coarse particulate mercury and gaseous elemental mercury oxidation within the surface boundary layer above the lake may be necessary and should be a topic for future research.

TABLE OF CONTENTS

LIST OF FIGURES

LIST OF TABLES

ACKNOWLEDGEMENTS

I would like to acknowledge and express my sincere gratitude to my advisor, Dr. Kevin Perry, who recognized potential in me and then helped me to recognize that potential in myself. If not for his guidance, support, and encouragement, this thesis would be only so-so at best. Thanks also to Dr. John Horel and Dr. Eric Pardyak for being part of my committee. I would also like to thank the Department of Atmospheric Sciences, including Dr. Jim Steenburgh, Kathy Roberts, and Leslie Allaire; the faculty, especially those who have taught classes that I have taken, and my student peers. Lastly, but most importantly, I would like to thank my wife Brittany Tanner Lisonbee and my children Chloe, Ada, and Ezra for all of their patience, encouragement, and support.

CHAPTER 1

INTRODUCTION

The Great Salt Lake (GSL), in northern Utah, USA, is the largest salt lake in the western hemisphere and the fourth-largest terminal lake in the world. Its open water and adjacent wetlands support several millions of migratory waterfowl and shorebirds from the western hemisphere (Waddell et al. 2009). The GSL also supports several industries, including brine shrimping, salts and other mineral production, and recreation. The GSL ecosystem receives discharge from a 37,500 km^2 watershed which includes over 2 million people (Naftz et al. 2008).

The GSL has recently been identified as "the hottest of hot spots for mercury pollution" (*The Salt Lake Tribune*, 21 Aug 2009) with nearly 38 times more mercury (Hg) than 97% of all water bodies sampled by the United States Geological Survey (USGS) from 1998 through 2005 (Naftz et al. 2008; Scudder et al. 2009; *The Salt Lake Tribune*, 21 Aug 2009). The GSL has a very unique chemistry that may cause it to be a more efficient Hg sink than other water bodies. Within the endorheic GSL, the only Hg removal process is through sedimentation to the lake bottom; this allows for higher concentrations of Hg in the GSL than in other waterbodies.

The goal of this thesis is to identify the amount of mercury that is depositing out of the atmosphere into the GSL through dry deposition. This thesis will also compare pathways of Hg into the GSL (i.e., dry deposition, wet deposition, and riverine influx) to

determine which pathway contributes the most Hg to the lake. This thesis provides important, and quantitative, information on the atmospheric dry deposition and chemistry related to the growing problem of Hg pollution in the GSL and by extension, to other water bodies in the Intermountain West. In addition, this information could eventually lead to preservation of the lake's fragile ecosystem and potentially the health of the millions of people and birds who use and live by the GSL.

Mercury pollution is not unique to the GSL but is becoming a growing problem throughout the Intermountain West. Mercury has been an issue for water bodies in the eastern United States for several decades while the mountain lakes in the western United States have remained relatively pristine. In recent years, however, the historically pristine lakes and rivers of the Intermountain West have experienced an increase in mercury pollution both in the water and in the aquatic wildlife. When the mercury levels in fish tissue exceed 0.3 mg kg^{-1}, the fish are deemed unfit for human consumption (Utah Department of Health Bureau of Epidemiology Environmental Epidemiology Program 2007). In the State of Utah, fish consumption advisories are issued by the Utah Department of Health, the Division of Wildlife Resources, and the Utah Department of Environmental Quality. By the end of 2003, the State of Utah had issued only three fish-consumption advisories. However, by the end of 2009, a total of 32 advisories had been issued.

1.1 Effects of Hg on the Ecosystem of the GSL

When mercury is deposited in waterways, including the GSL, bacteria convert it to methylmercury (MeHg). MeHg in the GSL builds up in the tissue of brine shrimp and

brine flies that are eaten by birds, which may then be eaten by other wildlife and by people. Because methylmercury is known to bioaccumulate within the food chain, even small amounts of Hg introduced into an aquatic ecosystem can result in fish and waterfowl that are unsuitable for human consumption (Sastry et al. 2002). The transport and deposition of atmospheric Hg is an important part of this process.

Naftz et al. (2008) measured a median concentration of total Hg in the GSL of 42 ng L^{-1} in the deeper water with a significant proportion (31-60%) of the total Hg comprised of MeHg. The median concentration of MeHg in the GSL was 24 ng L^{-1}. Waddell et al. (2008) confirmed elevated levels of Hg in the water and cited that the Farmington Bay (southeast arm) of the GSL had the highest levels of Hg pollution and MeHg concentration in eggs, liver, and muscle tissue in the wildlife.

In 2005, duck-consumption advisories were issued for Common Goldeneye, Cinnamon Teal, and Northern Shoveler ducks from the GSL due to mercury contamination. A consumption advisory was issued by the Utah Department of Health and the Utah Division of Wildlife Resources stating that "Common Goldeneye, Cinnamon Teal, and Northern Shoveler ducks from the Great Salt Lake should not be consumed" (Utah Department of Health 2010). The GSL is the first body of water in the United States to have a restriction placed on waterfowl consumption.

1.2 Effects of Hg Exposure on Human Health

Mercury's toxicity varies substantially between the elemental, inorganic, and organic forms. Elemental Hg is commonly ingested, but usually poses little risk due to the difficulty the digestive tract has in absorbing the metal and normally passes through the body unabsorbed. Direct contact with the skin also poses little risk due to the high

surface tension of the elemental form, which prevents it from penetrating the skin. The primary threat from elemental Hg is through long-term exposure to high concentrations of gaseous elemental mercury, which is easily absorbed by the lungs (Carpi 1997; Langford and Ferner 1999).

Inorganic compounds of mercury (Hg(I) and Hg(II)) form mercurous and mercuric compounds, respectively, and the toxicity of each is directly related to their solubility. Mercuric compounds are more soluble than mercurous compounds, enabling them to be absorbed more easily and thus pose a greater risk when ingested. Inorganic mercury compounds are usually nonvolatile and, as a result, poisoning through inhalation is rare. Exposure to inorganic mercury can affect the kidneys, causing immune-mediated kidney toxicity. Effects may also include tremors, loss of coordination, slower physical and mental responses, gastric pain, vomiting, and gingivitis (Utah Department of Environmental Quality 2010). However, much like elemental Hg, only a fraction (~10%) of inorganic Hg is absorbed in the body with long-term exposure generally required before serious damage occurs (Langford and Ferner 1999).

Organic mercury (such as MeHg) is a potent neurotoxin, meaning that it interferes with the way nerve cells function. Mercury poisoning causes a decreased ability to see, hear, talk, and walk. It can cause personality changes, depression, irritability, nervousness, and the inability to concentrate. It can also cause damage to the brain, kidneys, and lungs. MeHg is readily absorbed into the blood stream where it is transferred to the brain, tissues, and fetus if present. This causes a particularly serious problem for pregnant women and children. Fetuses and young children suffer the greatest risk because their nervous systems are still developing. They are four-to-five times more

sensitive to mercury than adults (Utah Department of Environmental Quality 2010). The dominant pathway for human and wildlife exposure to MeHg is through the consumption of contaminated fish.

1.3 Atmospheric Mercury

The three atmospherically relevant forms of mercury in ambient air are gaseous elemental mercury (GEM), gaseous oxidized mercury (GOM) most prevalent as the forms $HgCl_2$ and $HgBr_2$, and particulate mercury or particle bound mercury (PBM) (Landis et al. 2002). These species of mercury are considered the relevant species because each has its own special, and significantly different, characteristics, atmospheric behavior, and methods of detection that will be discussed in this section and in Chapter 2.

1.3.1 GEM

GEM is usually referred to as mercury vapor when present in the atmosphere. It constitutes the most prevalent form of mercury in the atmosphere, with a global background concentration of $1.5 \pm 0.2\ ng\ m^{-3}$ in the northern hemisphere and $1.2 \pm 0.1\ ng\ m^{-3}$ in the southern hemisphere (Lindberg et al. 2007). Natural sources of GEM into the Earth's atmosphere include geothermal outgasing of mantel or crustal material, surface soil evasion from naturally-enriched geologic deposits, evaporation from water bodies (both fresh and salt-water) (Gustin et al. 2002; Gustin 2003), vegetative decomposition, wildfires (Friedli et al. 2001, 2003), and volcanoes (Schroeder and Munthe 1998; Schuster et al. 2002; Pyle and Mather 2003).

Anthropogenic sources include combustion of coal (50% of anthropogenic sources) (Driscoll et al. 2007) and oil, cement production, production of nonferrous metals including lead and zinc, caustic soda (NaOH) production, mercury and gold

production, waste disposal, and leaks where mercury is used in thermostats and other electrical switches or control instruments, batteries, wiring devices, fluorescent lighting, etc. (Pacyna et al. 2006). It was estimated by Pacyna et al. (2006) that in the year 2000, there were ~2200 tons of mercury released into the atmosphere globally from anthropogenic sources.

Although great advances have been made during the past two decades in our understanding of atmospheric mercury (e.g., Schroeder and Munthe 1998; Landis et al. 2005), the exact dynamics and chemistry of GEM once it enters the atmosphere remains an active area of research with much still to be determined (Perrone et al. 2008). It is known to have a high vapor pressure [14 $mg\,m^{-1}s^{-2}$ at 20ºC, 31 $mg\,m^{-1}s^{-2}$ at 30ºC (Horvat 2005; Landis et al. 2005)], is relatively insoluble in water [~60 $\mu g\,L^{-1}$ at room temperature (Horvat 2005; Landis et al. 2005)], and has a low deposition velocity on the order of 0.05-0.1 $cm\,s^{-1}$ (Landis et al. 2005). As a result, GEM has a residence time in the atmosphere of approximately 0.5–2 years (Munthe and McElroy 1992; Schroeder and Munthe 1998; Poissant 2000; St. Denis et al. 2005; Biswas et al. 2007; Wiedinmyer and Friedli 2007), which allows transport on a hemispheric to global scale (Schroeder and Munthe 1998). With such a large transport range, it is not uncommon to measure GEM in the western United States that has been transported from Asia (Jaffe et al. 2005), or that is associated with Asian dust or pollution events (Jaffe et al. 1999, 2003; Price et al. 2003; Weiss-Penzias and Jaffe 2004; Weiss-Penzias et al. 2006).

Ambient GEM concentrations were measured for this study using a Tekran© Model 2537 Mercury Vapor Analyzer. More details about GEM measurements and the Tekran© Model 2537 will be provided in Section 2.2.1.

1.3.2 GOM

GOM is present in the atmosphere on the order of tens to hundreds of $\mathrm{pg\,m^{-3}}$. From an operational perspective, GOM, or Hg(II) [and less commonly Hg(I)], includes as a single entity all monovalent and divalent species of vaporous mercury, and is operationally defined by the method with which it is sampled (Perrone et al. 2008). GOM species (e.g., $\mathrm{HgCl_2}, \mathrm{HgBr_2}$) are considered highly toxic (Horvat 2005), water soluble, and have an atmospheric residence time around 1-2 weeks as these species are easily deposited by both wet and dry deposition (Biswas et al. 2007; Wiedinmyer and Friedli 2007). GOM is readily scavenged by precipitation and has a relatively high deposition velocity that is often compared to that of nitric acid, about 1-5 $\mathrm{cm\,s^{-1}}$ (Landis et al. 2002). The exact deposition velocity of GOM varies by species, oxidation state, and atmospheric parameters and will be addressed in Chapter 3. The oxidation of Hg(0) to Hg(II) increases the rate of atmospheric deposition, whereas reduction of Hg(II) to Hg(0) decreases the rate of atmospheric deposition (Lindberg et al. 2007). Our knowledge of the chemistry and dynamics of GOM has improved significantly over the past two decades, but uncertainties still remain. At the very least, it would be a great step forward if we had the ability to detect and measure the different forms of GOM in the atmosphere (Perrone et al. 2008).

GOM originates from both anthropogenic and natural sources. Anthropogenic sources of GOM into the atmosphere include municipal and medical waste incinerators and combustion of fossil fuels. It has been shown that GOM makes up about 78-95% of total mercury emissions from waste incinerators (Landis et al. 2002, 2005). GOM is also produced as a secondary pollutant. For example, GEM can react with several species in

the atmosphere (e.g., O_3, OH, Br, BrO, Cl) to become oxidized (Munthe and McElroy 1992; Lindberg et al. 2007). Natural sources of GOM include volcanoes and soil erosion. However, natural GOM will often readily bind to atmospheric aerosols and would be measured as PBM (Schroeder and Munthe 1998). Selin et al. (2007) suggest that GOM dominates over GEM in the upper troposphere and in the stratosphere because Hg(0) is readily oxidized to Hg(II) by OH and ozone.

Ambient GOM concentrations were measured for this study using a Tekran© Model 1130 Mercury Speciation Unit. More details about GOM measurements and the Tekran© Model 1130 will be given in Section 2.2.2.

1.3.3 PBM

PBM is present in the atmosphere on the order of tens to hundreds of $\mathrm{pg\,m^{-3}}$. PBM, by operational definition, may encompass either solid or liquid materials, which may be either homogeneous or heterogeneous with respect to physical and/or chemical composition and shape (Lynam and Keeler 2005). PBM is considered a very important player in the deposition of mercury regardless of very small concentrations because of its relatively large settling velocity.

There is much uncertainty associated with the size and density of the PBM particles. A study by Keeler et al. (1995) attempted to measure the size distribution of PBM in urban Detroit, MI. They found that the size of PBM is dominated by two modes, one for coarse and another for fine particles. The average particle size in each mode was 0.68 μm for the fine particles and 3.78 μm for the coarse particles (Keeler et al. 1995). Because of the range of particle sizes, an exact deposition velocity is difficult to measure or model. Keeler et al. (1995) demonstrated that the dry deposition flux from the coarse

particles is 4-5 times greater than that of the fine particles. PBM is generally not transported great distances due primarily to its high deposition velocity, and the fact that particulate matter is readily scavenged by precipitation.

PBM may enter the atmosphere from both anthropogenic and natural sources. Anthropogenic sources include coal combustion, nonferrous metal smelters, and waste incineration. PBM is also produced secondarily in the atmosphere. For example, it has been shown that GEM and GOM are both readily absorbed by thermally activated carbon particles, especially sulfur-impregnated activated carbon particles (Krishnan et al. 1994; Vidic et al. 1998).

PBM has an annual variability with higher values typically measured in the winter. This variability is probably caused by less acidic and oxidative gases present in colder temperatures, less sunlight available for photochemical reactions, cold pool inversions concentrating particles near the surface, and a higher likelihood of condensation onto particles (Lynam and Keeler 2005).

Ambient PBM concentrations were measured for this study using a Tekran© Model 1135 Particulate Mercury Unit. More details about PBM measurements and the Tekran© Model 1135 will be given in Section 2.2.3.

1.4 Dry Deposition

Dry deposition is “the process by which atmospheric gases and particles are transferred to the surface as a result of random turbulent air motions” (*AMS Glossary of Meteorology*, 2d ed., s.v. “Dry Deposition”). Gravitational settling also affects the deposition of particles. Dry deposition can account for a large portion of the removal of trace chemicals from the troposphere. There is currently no universally accepted

procedure to accurately measure dry deposition of trace gases and particles and estimates are usually arrived at using numerical models.

Previous studies of the dry deposition of Hg have suggested significant regional variation in the amount and type of Hg deposited (Gbor et al. 2006; Lin et al. 2006; Lindberg et al. 2007; Strode et al. 2007; Selin and Jacob 2008). For example, dry deposition, especially at remote locations, is dominated by input from the global mercury pool (Gbor et al. 2006; Lindberg et al. 2007). However, in some very industrial and highly populated locations, the global background comprises only about 30% of total the Hg contribution (Gbor et al. 2006, Selin and Jacob 2008). Gbor et al. (2006) found that the spatially averaged global background contribution to the total mercury deposition is 89% within the continental United States. The literature, furthermore, shows that deposition rates are generally higher in the eastern United States than the western United States, as expected from the emission distribution (Gbor et al. 2006, Selin and Jacob 2008). Wet deposition is comparable to dry deposition in the southeast and northwest United States, whereas in the Rocky Mountains and parts of the northern Great Plains, the wet deposition contribution is relatively small (Selin and Jacob 2008). This may suggest that generalized models may be inadequate to represent site-specific deposition.

It has also been shown that the net flux of GEM is bidirectional (Poissant et al. 2000; Converse et al. 2010) while the net flux of GOM and PBM are generally considered to be unidirectional, especially when considering wet surfaces (Poissant et al. 2000). Newly-deposited mercury is more available than soil-bound mercury for emission (or re-emission) on a time scale of days to months after deposition (Selin et al. 2007). The net flux of GEM across a water surface is dependent on the Henry's law coefficient for

GEM (Poissant et al. 2000; Anderson et al. 2008) and is highly correlated with solar radiation but poorly correlated with water temperature (Marsik and Keeler 2005). More information about the directionality of the flux of Hg across the surface of the GSL is given in Section 3.3 of this thesis.

A study by Peterson and Gustin (2008) measured atmospheric Hg concentrations at the GSL and modeled the dry deposition of GOM into the GSL using an average deposition velocity derived from the settling of similar chemical species onto surrogate surfaces and a general dry deposition model developed by Zhang et al. (2003) and modified by Lyman et al. (2007). This study found that an average GOM flux of about 4.3 $\mu g\ m^{-2}\ yr^{-1}$ was settling into the GSL.

Naftz et al. (2009) compared Hg found in lake sediment cores with Hg measured from riverine tributaries entering the lake, Hg wet deposition, and the Hg dry deposition values given by Peterson and Gustin (2008). Naftz et al. (2009) concluded that better and more complete measurements of dry deposition of Hg into the GSL are needed. A comparison of the results of this thesis and the GSL sediment cores is found in Chapter 5 of this thesis.

1.5 Resistance-in-Series Dry Deposition Model

The most widely used method for modeling the dry deposition velocity was first suggested by Wesely and Hicks (1977) who introduced a series of resistances, analogous to Ohm's law referring to electrical resistances. Wesely and Hicks (1977) suggested that the deposition velocity, or the rate at which a gas or small particle settles out of the atmosphere, is equal to the inverse of the resistance that it experiences. Wesely and Hicks (2000) suggest that this method is most reliable over homogenous flat terrain and caution

that “although this approach is practical, it can lead to oversimplification of the physical, chemical, and biological properties of the atmosphere of surface that affects deposition.”

There are three major divisions of resistances in the atmosphere. These are 1) the aerodynamic resistance above the surface which has the same value for all substances (R_a), 2) the quasi-laminar resistance to transport through the thin layer of air in contact with the surface which varies with the diffusivity of a substance (R_b), and 3) the resistance associated with direct interaction with the surface which is specific to both the depositing substance and the surface characteristics (R_c). More detail about each of these resistances and the resistance-in-series model will be given in Chapter 3.

This thesis will first discuss, in Chapter 2, the speciated atmospheric mercury measurements taken for this study, the instruments used, and the strengths and weaknesses of the data collected. Chapter 3 will introduce the resistance-in-series model, the physics used, and the assumptions made within the model to calculate dry deposition velocities for GEM, GOM, and PBM. The results of this model will be discussed in Chapter 4, including a quantitative analysis of the dry deposition flux of Hg from the atmosphere into the GSL and its contribution to the mercury pollution in the lake. Lastly, the conclusions of this study will be discussed in Chapter 5.

CHAPTER 2

INSTRUMENTATION

Brosset (1986) noted that the gradients of total mercury across industrialized northern Europe could not be explained by GEM alone and that reactive gaseous forms of mercury should also be analyzed (Brosset 1986). The Brosset (1986) study was the first indication of the need for speciated atmospheric mercury measurements. Atmospheric mercury has been monitored for over three decades, beginning with relatively crude and laborious manual methods of collecting "total gaseous Hg," and evolving to "semi-continuous measurements of the three environmentally relevant forms of Hg in the ambient air" (Landis et al. 2005). A suite of instruments developed in partnership by the U.S. EPA, the Florida Department of Environmental Protection, and Tekran© Inc. is designed to take automated and semicontinuous measurements of GEM, GOM, and PBM.

To better understand the measurements taken, this chapter will describe the location, instruments, and procedures used to measure ambient speciated mercury concentrations.

2.1 Site Description

The Tekran© atmospheric mercury measurement system was deployed at a field site located on the eastern shoreline of the GSL, in Davis County, Utah. The site has been

assigned the location identification “UT96” by the national Mercury Deposition Network.

The site is collocated with a Utah Department of Air Quality (DAQ) weather station. The site is located on the west side of Davis County which has an estimated population of 282,700. The majority of homes in the area use gas and electric heating. Interstate-15 is located roughly 7 miles to the east of the site and is a significant source of pollution for the area.

The site is subjected to alternating land/lake breezes depending on the time of day and the weather patterns. The heating differential between the lake surface and the land lake creates an afternoon breeze from the lake to the west (Fig. 2.1) thereby providing an excellent backdrop to measure ambient trends because of uniformity of topography, landscape composition, and a lack of local pollution sources from the west-northwest. The mountain canyons create an easterly wind overnight. All communities in the area, the interstate, and other major roadways are located to the east of the site. The proximity of an urban area to the east allows for ideal monitoring of urban pollution trends in the overnight hours.

The land immediately to the north and south of the site is rural, being either agricultural or entirely undeveloped. The town of Syracuse is to the east of the site. The coordinates of the UT96 site are 41.08851˚N, 112.11880˚W (+/- 5 m) as determined by a Garmin eTrex® Summit GPS unit. The elevation of the site is 4212 ft (1280 m), only a couple meters above the elevation of the GSL. The Wasatch Mountains are located 11 miles to the east and extend to elevations beyond 10,000 ft.

The Leaf Area Index (LAI) was determined using two Li-Cor LAI-2000 Plant Canopy Analyzers. These instruments calculate LAI based on light transmittance

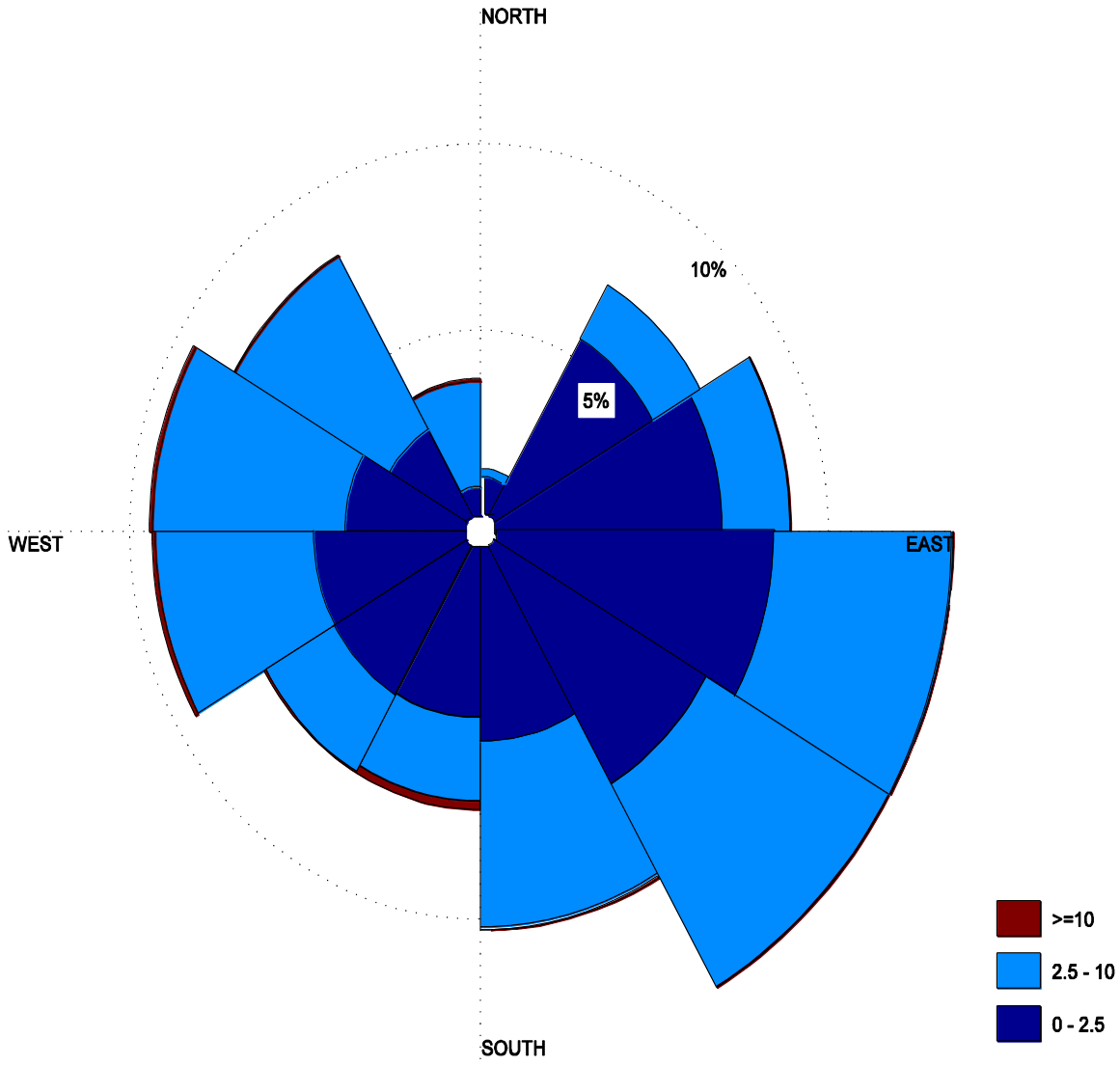

Figure 2.1. Wind rose for the site UT96 from July 1, 2009 through June 30, 2010.

through a canopy of vegetation. First measurements are made above the canopy to get a background measurement, and then subsequent measurements are taken below. To get an estimate of the site's overall LAI, the area within a radius of 0.5 km of the site was broken up into five basic LAI categories or vegetation types: reeds/cattails, pavement/mudflats, open water, wetlands, and pasture/field. The surface area of each category or vegetation type was estimated and recorded. Several measurements were taken in each vegetation area to estimate an average LAI. Pavement/mudflats and open water were assumed to have LAI values of zero. The average LAI for the entire plot is 0.229 m^2 m^{-2}.

The dominant feature in the area is the endorheic Great Salt Lake. The part of the lake that is adjacent to the site is very shallow. As a result, small changes in the lake elevation can have a dramatic impact on the surface area of the lake and the proximity of the lake to the sampling site. During wet periods, the lake can come within 100 meters of the site. During dry periods, the lake may recede several miles from the site.

2.2 Mercury Speciation Measurements

The Tekran© system consists of an instrument to measure GEM (model 2537), a thermally controlled denuder to capture GOM (model 1130), and a thermally controlled regenerative particulate filter (RPF) module to collect and subsequently desorb PBM (model 1135). This suite of devices began operating at UT96 on July 1, 2009. The Tekran© model 2537 is housed in a climate-controlled trailer and is connected to the Tekran© models 1130 and 1135 that are mounted on a 4 m tower (Fig. 2.2).

The Tekran© system automatically collects the three mercury species and then quantifies the amount of mercury collected in the following three steps (Fig. 2.3).

Figure 2.2. Tekran© models 1130 and 1135 mounted on a 4 m tower at the UT96 site. The Tekran© model 2537 is housed in the climate-controlled trailer.

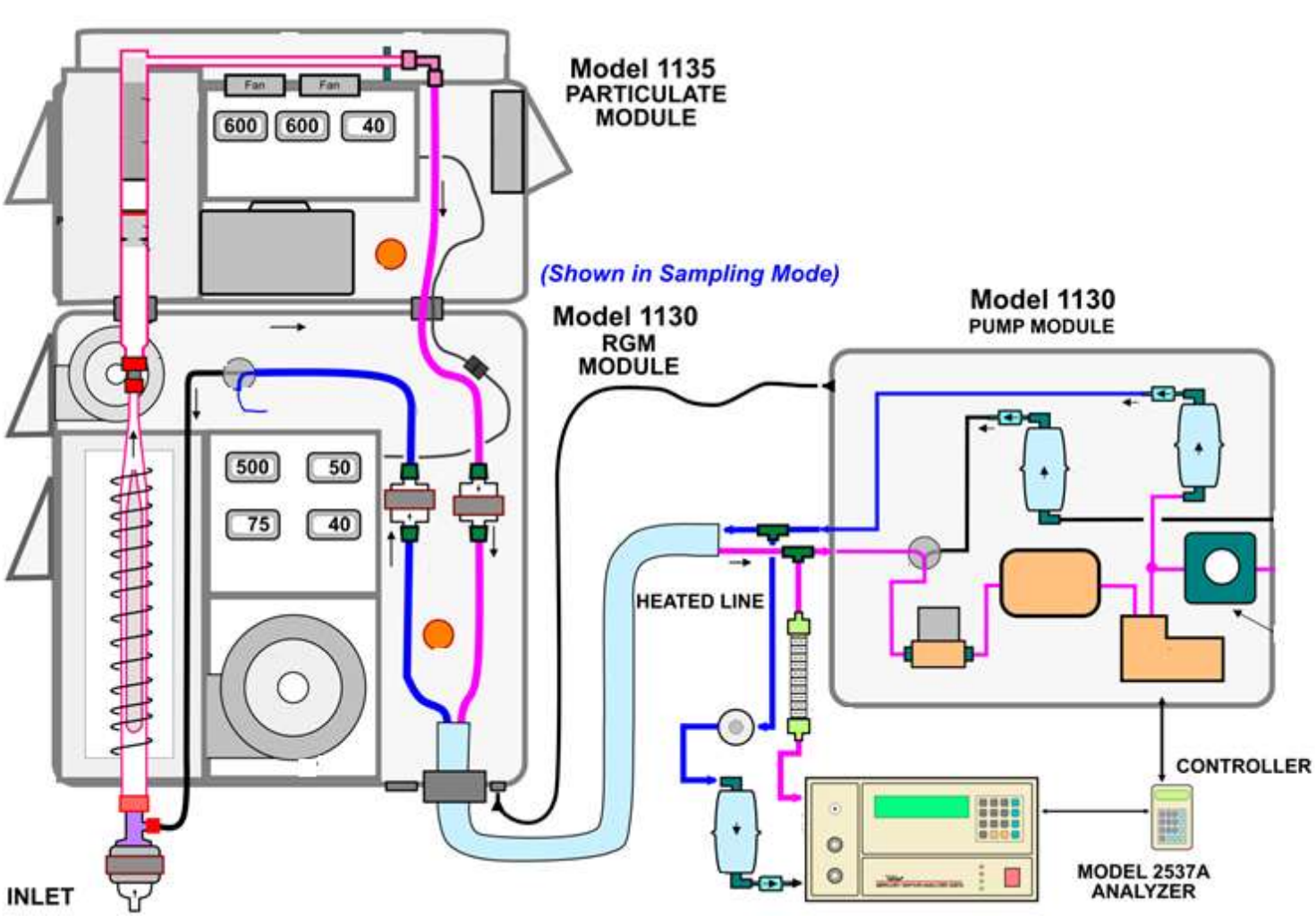

Figure 2.3. Schematic diagram of the Tekran© 2537, 1130, and 1135 Ambient Mercury Analyzers. Used with permission (Lucas Hawkins, Tekran Instruments Corporation, 2010, personal comunication).

Step 1: Ambient air is pulled under vacuum through an impactor inlet to remove particulate matter with aerodynamic diameters > 2.5 μm and then through a potassium chloride (KCl)-coated, quartz, annular denuder to selectively adsorb GOM, with GEM and PBM2.5 passing through the denuder.

Step 2: The air stream then passes through a RPF assembly to selectively capture PBM while the remaining mercury fraction, GEM, passes through and is captured on gold cartridges to complete the quantitative separation and collection of the mercury fractions.

Step 3: The mercury fractions must be in the form of GEM for quantitative transfer and preconcentration on gold cartridges and subsequent detection by the automated cold-vapor atomic fluorescence spectrometer (CVAFS). Mercury is thermally desorbed from the gold cartridges in an ultra high purity argon stream that carries the released GEM into the CVAFS for detection. During the GOM and PBM sample collection, GEM is continuously being collected on alternative A and B gold cartridges and analyzed by the automated CVAFS detector at 5-minute intervals.

For the specific purposes of this project, the system adsorbs GOM and PBM for a 2-hour period, and then switches to PBM and GOM analysis. During this period, the system thermally desorbs and converts in succession the PBM and GOM into GEM. The newly formed GEM is transported in a stream of zero air from the Tekran© 1130 (KCl-coated denuder) and 1135 (RPF) through a 25 foot long (7.26 m) heated (50ºC) line to the Tekran© 2537 ambient mercury vapor analyzer for preconcentration on gold cartridges and subsequent CVAFS detection. The data are recorded by DataCom© logging software, and then downloaded for analysis.

2.2.1 GEM Measurements (Tekran© Model 2537)

The Tekran© 2537 capitalizes on the fact that elemental mercury has a high affinity for noble metals (Au, Ag, Pt, Pd) and amalgamates readily (Schroeder and Munthe 1998; Landis et al. 2005). Specifically, the amalgamation with gold provides the basis for preconcentration of mercury vapor from samples of ambient air prior to analytical determination (Schroeder and Munthe 1998). The GEM is subsequently thermally extracted, and the extracted mercury can then be analyzed using CVAFS.

The Tekran© 2537 features two gold cartridges, cartridge A and cartridge B. "While cartridge A is adsorbing mercury during a sampling period, cartridge B is desorbed and analyzed" (Tekran© 2006c). After a set amount of time (300 seconds under standard operating procedures), the roles of the cartridges are reversed. This alternate action allows for continuous 5-minute-integrated samples with a 0.1 $\mathrm{ng\,m^{-3}}$ detection limit (Landis et al. 2005).

The extracted mercury is carried in a stream of inert, ultra high purity Argon carrier gas to a detector cell. The detector cell uses CVAFS for the mercury detection. The detector cell is a quartz cuvette illuminated by a low-pressure mercury vapor lamp. Radiation at 253.7 nm excites any mercury atoms present, which fluoresce and re-radiate at the same wavelength. A photomultiplier tube (PMT) is set at a right angle to the incident beam and detects the luminescence of the mercury through a monochromatic filter. The intensity of the illumination is directly proportional to the amount of mercury in the cuvette. The PMT outputs the intensity as a voltage that is measured against a reference baseline voltage (Tekran© 2006c).

There are two types of calibrations performed on the Tekran© 2537: internal (automatic) calibration and an external (manual) calibration. An internal calibration utilizes an internally housed permeation source that contains a small tube of Hg that has a known emission rate. During an internal calibration, a known amount of mercury is released into mercury free air and the instrument response is used for a one-point calibration. An external calibration serves primarily as a check of the internal calibration source. When an external calibration is performed, a known amount of mercury is injected into the volume of mercury free air that is passing onto the gold cartridges. Internal source calibrations are performed automatically every 3 days and ensure accurate data while in automatic sampling mode. The manual injection is performed at least once every 3 months, and is considered the primary standard method because it is directly based on the vapor pressure of mercury at a known temperature (Tekran 2006c).

2.2.2 GOM Measurements (Tekran© 1130)

GOM is typically present in the atmosphere in the 1-100 $\mathrm{pg\,m^{-3}}$ range. Because of these low concentrations, it can be very difficult to measure. There have been three successful methods to measure GOM (Landis et al. 2002, 2005). One of these utilizes cation-exchange membranes that are extracted with BrCl reduced to elemental mercury with a $SnCl_2$ solution purged onto a gold trap and analyzed with CVAFS. This method is slow and cumbersome, requiring a sampling time of ~24 hours. Another method, the refluxing mist chamber method, was adapted from a process to measure ambient nitric acid. This method provided some of the first high-resolution (1-2 hour) GOM measurements. In the mist chamber method, ambient air is drawn into a glass chamber where it comes in contact with a fine mist of diluted HCl and NaCl that adsorb soluble

mercury species. The droplets are then collected onto a Teflon filter, reduced to elemental mercury with $SnCl_2$ purged onto a gold trap, and analyzed with CVAFS. Mist chambers have their limitations in that they cannot be used in cold environments and the sampling durations are limited to the evaporation rate of the adsorbing solution (Landis et al. 2002, 2005). The third method used KCl-coated denuders. A denuder is a tube that is chemically coated to remove selected gas-phase species that diffuse to the walls and react or adhere to the coated surface. The first GOM-collecting denuders were tabular denuders, which are limited to a low flow rate (~1 L min^{-1}) to keep the flow laminar, and required the GOM to be extracted in $SnCl_2$ solution like the other methods.

To meet the growing need for speciated Hg measurements, an international panel of experts was assembled to discuss the strengths and weakness of the different methods and develop a consistent methodology to be used throughout the research community. Landis et al. (2002) describes how a coated denuder was decidedly the best option:

> We recognized that an advanced [GOM] methodology must meet the following criteria: (i) could be operated and maintained by a trained technician, (ii) could be operated under a wide temperature range (e.g., -40ºC to 50ºC), (iii) would be specific for [GOM] (e.g., no interference from Hg(p) and the much larger Hg0 component), (iv) has a method detection limit (MDL) low enough to allow background concentrations to be quantified at 1-h resolution, and (v) would minimize the possibility of contamination. Neither the impregnated ion-exchange membrane nor the refluxing mist chamber ambient air [GOM] measurement methodologies being used at the time satisfied all five criteria. (Landis et al. 2002)

In collaboration between the U.S. EPA, the Florida Department of Environmental Protection, and Tekran© Inc., three key modifications were made to the denuder method that allowed it to meet all the aforementioned criteria. First, a quartz annulus was built into the denuder. This increased the surface area to which the GOM could be collected.

The annular denuder also allowed for a higher flow rate through the denuder. Second, the active collection surface within the quartz annular denuder was etched to increase the KCl holding-capacity and produce a uniform coating. Third, thermal desorption was used, rather than chemical, to convert the GOM to GEM which can then be directly measured using CVAFS as described previously. The thermal desorption process is possible because the GOM species of interest (e.g., $HgBr_2$, $HgCl_2$) have a decomposition temperature on the order of 300ºC while the melting point of KCl is 771ºC (Landis et al. 2002).

The Tekran© 1130 Mercury Speciation Unit is a "front end accessory" to the Tekran© 2537. It allows the 2537 Mercury Vapor Analyzer to "simultaneously monitor and differentiate between elemental and reactive gaseous mercury species in ambient air" (Tekran© 2006b). The Tekran© 1130 consists of a heated impactor that allows only smaller particles (i.e., D_p < 2.5 μm) to pass into an annular denuder that has been coated with KCl, a heater, temperature sensors, and particulate filter packs all enclosed within a heated case and connected to the Tekran© 2537 with a heated sample line (Tekran© 2006b). The sample line is held at a constant 50ºC to prevent any deposition of Hg onto the inner wall of the tube.

During the sampling phase, the denuder is heated to 50ºC to prevent water vapor from hydrolyzing the KCl coating. The warmed denuder captures GOM in ambient air while GEM passes through the denuder and the sample lines to be measured by the detector in the Tekran© 2537. A normal flow rate of 10 $\mathrm{L\,min^{-1}}$ through the denuder is maintained by the Tekran© 1130 pump module (Tekran© 2006b). The flow rate through the Tekran© 1130 is ten times the flow utilized by the 2537. This higher flow rate is

necessary because GOM concentrations are typically one to two orders of magnitude less than GEM (Tekran© 2006b,c)

When the sampling cycle is complete and the desorb cycle begins, zero air, or air that is completely devoid of mercury, is introduced into the denuder so that ambient air is flushed from the system. During this stage in the cycle, the detector measures very low or zero mercury. This is the "pre-desorb blank" and is used to check for possible contamination before the denuder is heated. In the next stage, the denuder is thermally desorbed at 500ºC in mercury free air. When heated, the GOM is released from the KCl and thermally decomposed into GEM for measurement. The release is not instantaneous, but is usually completed within two or three 5-minute measurement cycles. The newly formed GEM is ushered through a heated sample line and directed into the Tekran© 2537 for detection. When the sampling phase is complete, the denuder has been cleaned of any mercury and is sufficiently cool to allow for adsorption in the next sampling stage (Tekran© 2006b).

The Tekran© 1130 desorption cycle includes multiple 5-minute detection periods. The mercury measurements from each 5-minute detection period must be added, and pre-desorb blanks accounted for, to obtain the true GOM measurement. Figure 2.4 shows the data reduction routines that must be applied to every desorb cycle (Tekran© 2006b; Miller 2009).

Tekran Desorb Program			Tekran GOM and PBM Data Reduction Routines	
Cycle ID	Description	Flag	PBM2.5 Calculation	GOM Calculation
A	Flush	1		
B	Flush	1	(E+F+G) - 3*C	(H+I+J) - 3*C
C	Flush	1		
D	Pyro-Ht	2		
E	Part-Ht	2		
F	Part-Ht	2		
G	Part-Ht	2		
H	GOM-Ht	3		
I	GOM-Ht	3		
J	GOM-Ht2	3		
K	Cool	1		
L	Cool	1		

Figure 2.4 Data reduction routines for the Tekran© desorb program used to calculate the GOM and PBM concentrations from raw ambient mercury data files (Miller 2009).

2.2.3 PBM Measurements (Tekran© Model 1135)

Measurement of PBM typically entails the collection of the particles onto a filter, then an analysis of the filter. In practice, however, it is not that easy. Some have suggested that making accurate and precise measurements of this species might be the most difficult to perform (Lynam and Keeler 2004). Very small concentrations and the existence of artifacts associated with the measurements make PBM quite difficult to measure. PBM is present in the atmosphere in the order of tens to hundreds of $\mathrm{pg\,m^{-3}}$. Large sources of error may emerge from the presence of high concentrations of GOM or ozone, and when possible, these should be removed from the sampling stream before the particles are collected by the filter (Lynam and Keeler 2004; Landis et al. 2005).

The Tekran© Model 1135 Particulate Mercury Unit, together with the Tekran© Model 1130 Mercury Speciation Unit allows for the capture and direct measurement of PBM in connection with the measurement of GOM and GEM. The Tekran© 1135 is considered an accessory to the Tekran© 2537 and can be used only in conjunction with the Tekran© 1130 (Tekran© 2006c). The dependence of the Tekran© 1135 on the Tekran© 1130 to remove GOM prior to measuring PBM introduces the size limitation on PBM measurements. Particles with aerodynamic diameters > 2.5 μm must be removed at the inlet to the denuder, in the Tekran© 1130, to prevent the collection of particles on the denuder's inner surface. This allows for accurate measurements of PBM on small particles, but eliminates any information about the amount of PBM that may be bound to coarse particles (i.e., D_p > 2.5 μm).

The active sampling element for the Tekran© 1135 is a quartz RPF. The quartz RPF assembly is housed in a vertical, dual-zone, ceramic oven. This dual-zone oven is

engineered with a high-powered heating element and a high-speed blower allowing it to heat and cool quickly. This allows for temperature control of the two main elements of the RPF. The first stage of the RPF consists of the quartz wool and a 0.1 μm quartz fiber disk. These provide enough surface area to collect the majority of the particulate matter over many cycles without becoming clogged. The second section of the RPF is the pyrolyzer. The pyrolyzer is filled with small quartz chips that act to maximize contact with the sample gas. A quartz wool plug is inserted above the chips to keep them in place. The purpose of the pyrolyzer and chips is to ensure that any compounds released from the particulate filters have ample opportunity to be converted to GEM prior to entering the sampling line (Tekran© 2006b).

2.3 Quality Assurance

The raw data from the Tekran© 2537 are run through a rigorous quality assurance process that includes 26 automated checks and 7 manual checks. These checks, or flags, are used to ensure that only valid data are used when calculating statistics for each month. The quality assurance of raw data will be described in this section.

2.3.1 Automated Quality Assurance Checks

Eleven automated checks with 26 individual flags are used to ensure that only valid data are used when calculating statistics for each month. Following the nomenclature suggested by Miller et al. (2009), data that have been quality assured by the automated system is labeled “QA level 1.” These automated checks, or flags, are output in the final quality assured data file in the "notes" column. If a data flag appears, but the data point is not invalidated, then the data are considered suspect and action may need to

be taken. The individual quality assurance checks and flags are shown in Tables 2.1 and 2.2.

The automated quality assurance checks in Table 2.1 meticulously examine each data point, calibrations, and trends to identify any potential malfunctions in the equipment. Data flags include checks that the baseline voltage is not too large or too small, and that background instrument noise, indicated by the baseline voltage standard deviation, is not out of allowable range. Flags can also mark where the volumetric flow rate drops below operational limits or where measurement peaks are inconsistent. The calibration quality assurance includes checks of the calibration frequency, response factor, and calibration blanks. GEM data, taken every 5 minutes, are checked for consistency from one point to the next and from one cartridge to the next. The entire QA process is intentionally both rigorous and thorough.

After the data pass through the automated quality assurance process, they are marked as “QA level 1.” The GOM and PBM data are then separated and concentrations for each desorb cycle are calculated using the data reduction algorithm shown in Fig. 2.4. Finally, quality assured data for all three Hg species are saved into three separate files to be annually checked.

2.3.2 Manual Quality Assurance Checks

Before "QA level 1" data can be upgraded to "QA level 2" they must be manually examined and flagged according to the manual quality assurance flags found in Table 2.2. These manual flags primarily concern standard maintenance routines that are performed on the equipment. For example, during biweekly maintenance, the glassware (the annular denuder and the RPF) and the soda lime trap are replaced. When the glassware is

Table 2. 1. Automated quality assurance flags.

Flags	Flag Type	Description	Conditions for Activation	Range	Valid/ Invalid	Data Flagged
A1	Ambient	Ambient Air Trap Bias	10% Difference over 24 hour period	24-hr means of each trap	V	All
A2	Ambient	Ambient Air Trap Bias	15% Difference over 24 hour period	24-hr means of each trap	I	GEM
B1	Baseline	Baseline Voltage	Baseline <0.05 or >0.25 V	Each observation	V	GEM
B2	Baseline	Baseline Voltage Change	Change > 0.01 from previous obs.	Compare prev. vs. current obs.	V	All
B3	Baseline	High Baseline Deviation	5 consecutive deviations > 0.1 V	Compare prev. 5 in a row obs.	V	All
B5	Baseline	High Baseline Deviation	Baseline deviation >0.2 V	Each observation	I	All
B0	Baseline	Low Baseline Voltage	Baseline voltage <0.01 V	Each observation	I	All
M2	Readout	Multiple Peaks Detected	Status = M2	Each observation	V	All
M3	Readout	Multiple Peaks Detected	Status > M2	Each observation	I	All
OL	Readout	Detector Overload	Status = OL	Each observation	V	All
NP	Readout	No Peak Detected	Status = NP	Each observation	I	GEM
E5	Elemental	Suspect GEM Concentration	If GEM concentration change > 50%	Compare obs. on same trap	V	GEM
E1	Elemental	Suspect GEM Concentration	If GEM concentration < 1.00 ng m^{-3}	Compare obs. on same trap	V	GEM
E0	Elemental	Post Desorb GEM	First GEM concentration from each trap	First obs. on each trap	I	GEM
V5	Volume	Sample Volume	Volume 5% from expected	Each observation	V	All
V7	Volume	Sample Volume	Volume 7% from expected	Each observation	I	All
F1	Freq	Calibration Interval	Previous calibration > 72 but <144 hrs ago	Past 144 hrs of obs.	V	All
F2	Freq	Calibration Interval	Previous calibration > 144 hrs ago	Past > 144 hrs of obs.	I	All
R1	Response	Detector Sensitivity	Response factor < 6 M or > 12 M units	Each observation	V	All
R2	Response	Detector Sensitivity	Response factor < 4 M units	Each observation	I	All
C5	Calibration	Calibration Change	Calibration is 5% from previous	Compare prev. vs. current obs.	V	All
C0	Calibration	Calibration Change	Calibration is 10% from previous	Compare prev. vs. current obs.	V	All
Z1	Zero	Calibration Blanks	Zero > 1500 PA units	Each observation	V	All
Z2	Zero	Calibration Blanks	Zero > 1% SPAN	Each observation	I	All
C1	Calibration	Calibration Trap Bias	Trap response factor > 10% different	Compare last RF Cart A + B obs.	V	All
C2	Calibration	Calibration Trap Bias	Trap response factor > 20% different	Compare last RF Cart A + B obs.	I	All

Table 2.2. Manual quality assurance flags.

Flags	Flag Type	Description	Conditions for Activation	Range	Valid/ Invalid	Data Flagged
RM		Routine Maintenance	User Defined	Each observation	I	All
I2	Injection	Manual Injection	Calibration Source Verification	Each observation	I	All
I1	Injection	Pre Injection	Pre Calibration Verification	Each observation	I	All
I3	Injection	Ambient Air Injection	Matrix Spike	Each observation	I	All
Q3	QA	Flow Check	Flow Verification	Each observation	I	All
O1	Other	Other	User Defined	Each observation	V	All
O2	Other	Other	User Defined	Each observation	I	All
Q2	AQ	Glassware Changed	First Desorption Cycle	Each observation	I	GOM & PBM
XV	Invalid	Invalid Data	Invalidated Data, Per Site Liaison	Individual observations	I	All
Q1	QA	Soda Lime Changed	First Elemental	Each observation	I	All
V1	Valid	Valid Data	Valid Data, Per Site Liaison	Individual observations	V	All

changed, at least the first (and occasionally the second or third) desorb cycle after the change is invalidated to account for contamination on the denuder or RPF and any possible contamination that may have entered the system while it was open.

2.4 Sonic Anemometer

A Campbell Scientific, Inc. (CSAT3) 3-D sonic anemometer is used for all meteorological measurements needed for the deposition calculations. This device is mounted on the DAQ meteorological tower at 8 meters above the ground and oriented 200 degrees from north, toward the southwest. At this height above relatively uniform terrain, the flux foot print has a variable range of 100 m to as much as 2 km. The CSAT3 provides 10 Hz measurements of wind speed, wind direction, and a "sonic" temperature, which for operational purposes is equivalent to virtual temperature. These measurements are logged using a Campbell Scientific CR1000 datalogger.

The meteorological data were averaged to synchronize with the mercury measurements. GOM and PBM measurements are taken once every 3 hours and therefore, the meteorological data were averaged into 3-hour periods to synchronize with the mercury data. GEM measurements are taken every 5 minutes. Figure 2.5 shows the variance of the wind components compared with different averaging times. From Fig. 2.5, it was determined that any averaging time > about 10 minutes would be sufficient to make the data uniform with the longer averaging time needed for the GOM and PBM measurements. An averaging period of 30 minutes was used for convenience.

All valid mercury data are aligned with meteorological parameters taken from the sonic anemometer. The aligned data are now ready to be input into the resistance-in-series dry deposition model that will be described in Chapter 3.

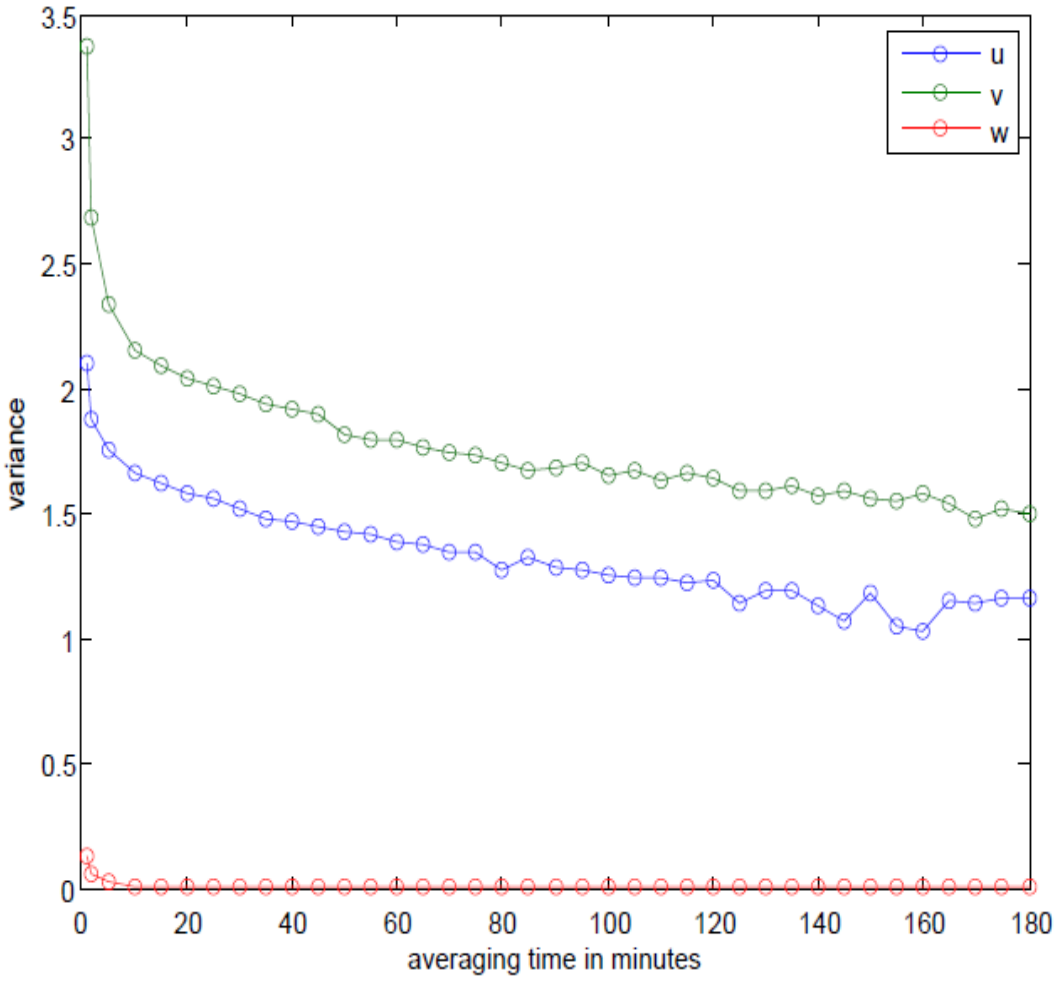

Figure 2.5. Variance versus averaging period in minutes. An averaging period was chosen based on the slope of the curve.

CHAPTER 3

MERCURY DRY DEPOSITION

MODEL METHODOLOGY

The goal of this project is to quantify the dry deposition of atmospheric mercury to the GSL over a 1-year period. In situ measurements of speciated mercury and atmospheric turbulence parameters were collected from July 1, 2009 through June 30, 2010 and will be used as input to a dry deposition resistance-in-series model (adapted from Giorgi 1986; Liss and Merlivat 1986; Hicks et al. 1987; Zhang et al. 2001; Seinfeld and Pandis 2006). The downward flux of a species to a surface can be calculated by:

$$F = -V_d C \qquad (3.1)$$

where F is the flux, V_d is the deposition velocity, and C is the measured concentration. The negative sign is a directional indicator indicating downward transport.

There is no universally accepted technique capable of directly measuring the deposition velocity of particles or trace gases to a surface. As a result, researchers are forced to rely upon model estimates for this important quantity. Wesley and Hicks (1977) proposed a resistance-in-series method that calculates the resistance to transfer in a manner analogous to electrical resistance to the flow of electrons. Using this analogy, the deposition velocity is defined as:

$$V_d = \frac{1}{(R_a + R_b + R_c + R_a R_b V_s)} + V_s \qquad (3.2)$$

where R_a is the aerodynamic resistance, R_b is the quasi-laminar resistance, R_c is the surface resistance, and V_s is the gravitational setting velocity (Fig. 3.1).

3.1 Aerodynamic Resistance (R_a)

Gases and particles can only be removed from the atmosphere by dry deposition if they impact the surface. There are two mechanisms that can transport gases and particles to the surface (turbulent mass transport and molecular diffusion). R_a is the resistance from turbulent mass transport. The turbulent intensity is primarily dependent upon the stability of the boundary layer and the surface roughness. Turbulent intensity typically reaches a maximum and extends over the greatest depth in the late afternoon when the sensible heat flux from the surface is the greatest. As the boundary layer deepens, it becomes well-mixed and exposes a correspondingly ample reservoir of material to potential surface deposition. At night, the atmosphere often becomes stable near the surface due to radiative cooling. This stable stratification often diminishes the intensity and vertical extent of the turbulence and effectively reduces the dry deposition flux. With the exception of large particles that have appreciable gravitational settling velocities, R_a is independent of the specific gas or particle composition.

The aerodynamic component of the overall dry deposition resistance is quantitatively based on gradient transport theory and mass transfer similarity theory. The turbulent transport of a particle or gas species through the atmospheric surface boundary

:

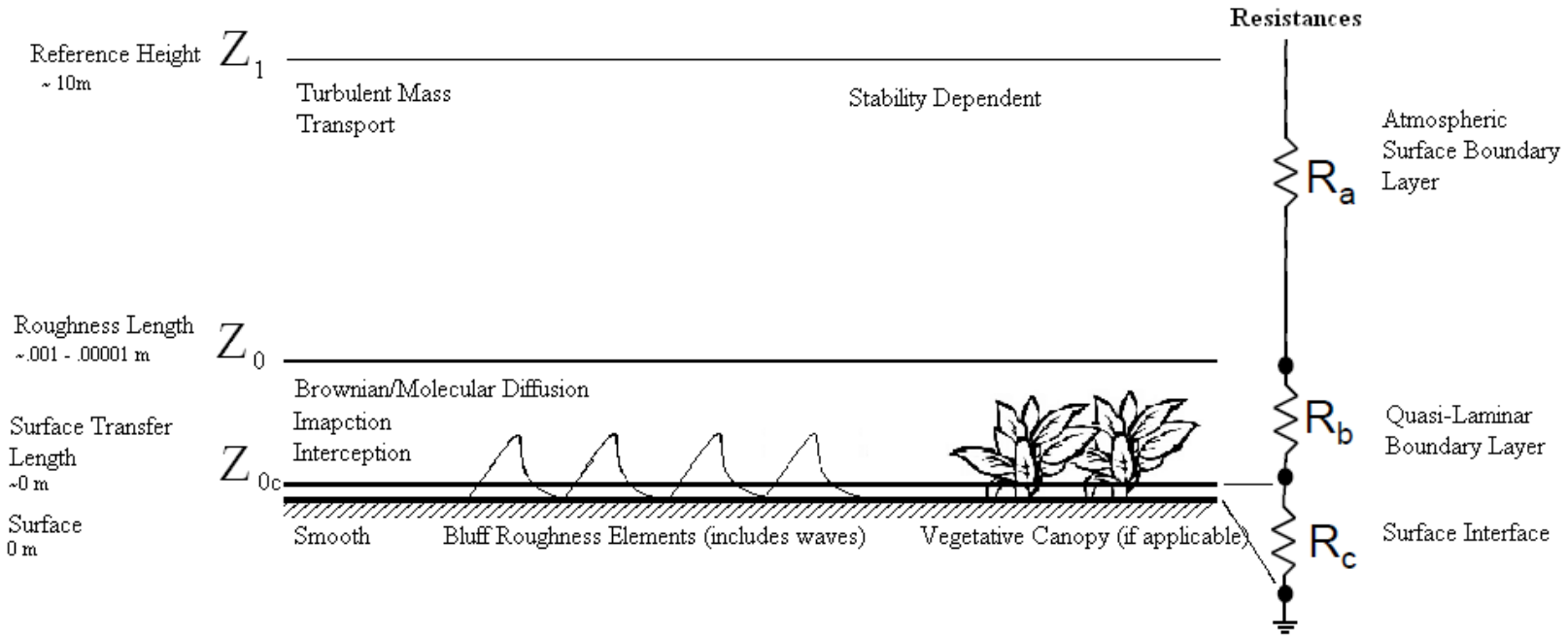

Figure 3.1. Diagram of the atmospheric surface layer showing the associated resistances with each sublayer, approximate heights of layer boundaries, and physical transport mechanisms.

layer (Fig. 3.1) can be expressed in terms of a concentration gradient of the quantity $\left(\frac{\partial C}{\partial z}\right)$ multiplied by eddy diffusivity (*K*). Turbulent transport of materials occurs by mechanisms that are similar to those for turbulent heat and/or momentum transport. As a result, the measurements obtained for one of these quantities (heat is usually used as a better representation of a scalar) can be applied, using appropriate scaling parameters, to calculate the corresponding behavior of the scalar. Expressions for R_a are most easily obtained by integrating the micrometeorological flux-gradient relationships. Applications of similarity theory to turbulent transfer through the surface layer suggest that *K* is proportional to the friction velocity (u_*) and the height above the ground. Under diabatic conditions, *K* must be adapted from its neutral form by a stability dependent function, $\phi(\zeta)$, in which ζ is the dimensionless height scale given by $\zeta = {}^{z}/_{L}$ where *z* is the reference height (or the measurement height) and *L* is the Monin-Obukhov length (Businger et al. 1971; Seinfeld and Pandis 2006, 906–907).

The vertical turbulent flux (F_a) of a species with concentration *C* through the surface layer (assuming a constant flux across a layer) is expressed as:

$$F_a = K_T \frac{\partial C}{\partial z} \qquad (3.3)$$

where K_T is the eddy diffusivity for heat transfer and $\frac{\partial C}{\partial z}$ is the concentration gradient. K_T was chosen instead of the eddy diffusivity for momentum transfer (K_M) because it more closely relates to the movement of a scalar quantity, such as GEM and GOM, through the atmosphere (Giorgi 1986; Hicks 1987). From dimensional analysis and micrometeorological measurements, the eddy diffusivity can be expressed as:

$$K_T = \kappa \frac{u_* z}{\phi_T(\zeta)} \quad (3.4)$$

where κ is the von Karman constant (usually taken to be 0.4), u_* is the friction velocity, and $\phi_T(\zeta)$ is an empirically determined, dimensionless temperature profile function that is a function of stability (Seinfeld and Pandis 2006; Bretherton 2010). $\phi_T(\zeta)$ acts as a diabatic correction to account for effects of buoyancy-induced changes in flux-gradient relationships (Wesely and Hicks 1977). The generally accepted forms of the temperature profile function are those of Businger et al. (1971):

$$\phi_T(\zeta) = Pr + 4.7\zeta \quad \text{for stable conditions (i.e., } \zeta > 0) \quad (3.5)$$

$$\phi_T(\zeta) = Pr \quad \text{for neutral conditions (i.e., } \zeta = 0) \quad (3.6)$$

$$\phi_T(\zeta) = Pr(1 - 9\zeta)^{-1/2} \quad \text{for unstable conditions (i.e., } \zeta < 0) \quad (3.7)$$

where Pr is the Prandtl number (taken to be 7.3).

If integrated across the depth of the surface boundary layer from z_1 to z_0 (Fig. 3.1), F_a may be written as:

$$F_a = (C_1 - C_0)\left(\int_{z_0}^{z_1} \frac{\phi_T(\zeta)}{\kappa u_* z} dz\right)^{-1} \quad (3.8)$$

where C refers to the concentration at the top (1) and bottom (0) of the flux layer. Thus, the aerodynamic resistance is given by:

$$R_a = \int_{z_0}^{z_1} \frac{\phi_T(\zeta)}{\kappa u_* z} dz \qquad (3.9)$$

Upon integration from the bottom of the surface boundary layer (at the roughness length, z_0) to the top (some reference height, z_1), and upon substitution of ϕ_T for different stability regimes using Eqs. 3.5 through 3.7, R_a becomes:

$$R_a = \begin{cases} \frac{Pr}{\kappa u_*}\left[\ln\left(\frac{z_1}{z_0}\right) + 4.7(\zeta - \zeta_0)\right] & (stable) \\ \frac{Pr}{\kappa u_*}\ln\left(\frac{z_1}{z_0}\right) & (neutral) \\ \frac{Pr}{\kappa u_*}\left[\ln\left(\frac{z_1}{z_0}\right) + 2\ln\left(\frac{(1+\eta_0)}{(1+\eta)}\right)\right] & (unstable) \end{cases} \qquad (3.10)$$

where $\eta = \sqrt{(1-9\zeta)}, \eta_0 = \sqrt{(1-9\zeta_0)}$, and $\zeta_0 = z_0/L$.

From Eq. 3.10, it is evident that the model is stability dependant with the Monin-Obukhov length (L) being the defining stability parameter. L is calculated as:

$$L = -\frac{u_*^3 T_v}{\kappa g \overline{w' T_{v0}'}} \qquad (3.11)$$

where T_v is the virtual potential temperature, g is gravitational acceleration, κ is the von Karman constant, u_* is the friction velocity, and $\overline{w' T_{v0}'}$ is the virtual surface heat flux. A positive L indicates a stable atmosphere and a negative L indicates instability. R_a increases with increasing stability. As a qualitative physical description of the stability dependence of R_a, turbulent motions bring Hg laden air from the upper surface boundary layer to the surface where deposition may occur. When the atmosphere is very stable,

gravitational settling velocity is the only physical process acting to bring a substance toward the surface. For gases, the gravitational settling velocity is negligible and the resistance across the stable layers is very large.

3.2 Quasi-Laminar Resistance (R_b)

The resistance-in-series model asserts that adjacent to every surface is a quasi-laminar sublayer (Fig 3.1). The transfer of material across this quasi-laminar sublayer depends highly upon the specific properties of the substance being transferred and the surface characteristics. For example, R_b is strongly influenced by the diffusivity of the material being transferred. Materials with higher diffusivities will have much less resistance to transfer across the sublayer. In addition, gases and small particles behave quite differently in terms of their resistance to transport across this layer. The quasi-laminar sublayer is likely formed as a consequence of many very thin viscous layers adjacent to the obstacle constituting the overall effective surface seen by the atmosphere (Seinfeld and Pandis 2006, 907–908). The depth of this layer constantly varies as a result of turbulent shear stresses adjacent to the surface or surface elements. In fact, the layer may disappear from time to time on some surfaces. For example, surfaces such as plant leaves, which are often in motion, may see this layer appear only when the leaf is still. "Whether a quasi-laminar layer actually exists physically depends on the smoothness and the shape of the surface or surface elements, and to some extent the variability of the near-surface turbulence, but, in terms of the theory, it is considered to exist" (Seinfeld and Pandis, 2006, p. 908).

3.2.1 Gases

The viscous boundary layer adjacent to most surfaces (Fig 3.1) acts to impede the deposition of all gaseous species and very small particles with negligible fall speeds, regardless of the orientation of the depositing surface. Molecular (and Brownian) diffusion in the atmosphere occurs independently of direction. Therefore, a gas molecule or small particle can deposit to the underside of a surface just as easily as it can deposit to the top surface. Similar to Eq. 3.3, the flux through this layer can be expressed as:

$$F_b = K_T \frac{\partial C}{\partial z} \qquad (3.12)$$

(Seinfeld and Pandis 2006, p. 908; Bretherton 2010). However, unlike R_a within the surface boundary layer, neutrality may be assumed which gives the temperature profile function a constant value of unity (i.e., $\phi_T(\zeta) = 1$). The limits of integration across this surface boundary will be from the surface roughness length (z_0) on the upper bound to a "surface transfer length" on the lower bound. This revised roughness length (z_{0c}) was introduced by Wesley and Hicks (1977) and is specific to the gas or particle of interest. The flux through the surface boundary may now be represented as:

$$F_b = (C_z - C_{0c}) \left(\int_{z_{0c}}^{z_0} \frac{1}{\kappa u_* z} dz \right)^{-1} \qquad (3.13)$$

Thus, the aerodynamic resistance is given by:

$$R_b = \int_{z_{0c}}^{z_0} \frac{1}{\kappa u_* z} dz \qquad (3.14)$$

Upon integration the resistance becomes:

$$R_b = \frac{1}{\kappa u_*} \ln\left(\frac{z_0}{z_{0c}}\right) \qquad (3.15)$$

Field studies of sensible heat and water vapor transfer yield a limiting value of $\kappa u_* R_b = \ln\left(\frac{z_0}{z_{0c}}\right) \cong 2$ (Hicks et al. 1987). As suggested by the literature and shown by specialized surface transfer models (Garratt and Hicks 1973; Brutsaert 1975, 1979; Deacon 1977; Hicks et al. 1987; Schwarzenbach et. al. 2003, 909–910; Seinfeld and Pandis 2006, p. 908), R_b has a functional dependence on the dimensionless Schmidt number (*Sc*) and surface roughness. This would indicate that mass transfer at the interface must be controlled by the simultaneous influence of the diffusivity of the species across the layer and the transport of turbulence across the layer (described by the coefficient of the kinematic viscosity) (Schwarzenbach et al. 2003, 909–910). *Sc* is defined as:

$$Sc = \frac{\nu}{D} \qquad (3.16)$$

where ν is the kinematic viscosity and D is the molecular diffusivity. This functional dependence of R_b on *Sc* gives a general form of the resistance as:

$$R_b = \frac{2}{\kappa u_*}\left(\frac{Sc}{Pr}\right)^p \qquad (3.17)$$

were p is taken to be 2/3 for smooth surfaces and decreases for rougher surfaces (often taken to be 1/2 for very rough surfaces) (Hicks et al. 1987; Schwarzenbach et al. 2003, 909–910). Hicks et al. (1987) suggest that for most gases, the uncertainty associated with the value of p is not critical except for very slowly diffusing quantities. Within the deposition model, p is assigned the value 2/3 when the 10 m wind is less than or equal to 5 m s^{-1} (for smooth water) and is reassigned the value 1/2 when the 10 m winds exceed 5 m s^{-1} (for rough water) (Schwarzenbach et al. 2003, 909–910). *Pr* for air is ~ 0.73 and is included in Eq. 3.17 to account for the fact that the basic observations are primarily of heat transfer (Wesely and Hicks 1977; Hicks et al. 1989).

The following explanation by Schwarzenbach et al. (2003, p. 910) is useful to understand, at least qualitatively, the dependence of R_b on *Sc*.

> Imagine a border between two [political] states which—for whatever reason—can only be crossed on foot. People use taxis to get to the border, yet when approaching the border the streets become increasingly narrow and the cars get stuck. The passengers in the taxis (they must all be trained mathematicians!) know exactly the optimal time to jump out of the cars, in order to walk or run the remaining distance and to cross the border after the shortest possible time. Obviously, the distance from the border where people leave the taxis is not the same for all persons and all road conditions. People who are fast runners (that is, have "large diffusivities") leave their cars earlier than people who can walk only with difficulty ("small diffusivities"). The latter will remain in their taxis as long as possible, even if the cars move only very slowly through the congested streets, but they have got to get out of their vehicles sometime as well. In turn, one and the same person does not always leave the taxi at the same distance from the border. In some areas the roads leading to the border are narrower and thus more strongly congested ("large viscosity" damping the motion of the cars, that is, of the eddies); in others they are broader (small viscosity)…To summarize, the time needed to cross the border, that is, the *border transfer velocity*, depends on the individual mobility of foot (diffusivity) and the quality of the roads (viscosity). Or

> stated differently: the distance from the border where the passengers leave the taxi since the speed of the cars…drops below the speed of the individual pedestrian (molecular transport), depends on the relative size of the pedestrian mobility and car mobility. Transfer velocities are large for fast runners and permeable road systems and small for physically handicapped passengers and narrow streets. (Schwarzenbach et al. 2003)

To calculate *Sc* using Eq. 3.16, information is needed about the kinematic viscosity of the air and the molecular diffusivity of mercury vapor in the air. It is assumed that the kinematic viscosity of the mercury vapor that is present in well-mixed air in parts per trillion for GEM and parts per quadrillion for GOM is the same as the kinematic viscosity of the air. Sutherland's formula (Eq. 3.18) can be used to calculate the dynamic viscosity of the air:

$$\mu = \mu_0 \left(\frac{T_0 + C}{T + C}\right)\left(\frac{T}{T_0}\right)^{3/2} \qquad (3.18)$$

for which μ is the dynamic viscosity in units of Pa s at input temperature *T*, μ_0 is a reference viscosity in units of Pa s at reference temperature T_0, and *C* is Sutherland's constant. *C* is taken to be 120 for well-mixed dry air and is valid up to 550 K (Crane Company 1988). The kinematic viscosity and dynamic viscosity are related by:

$$\nu = \frac{\mu}{\rho_a} \qquad (3.19)$$

where ρ_a is the density of air. The molecular diffusivity of gaseous elemental mercury vapor in the air was taken from Massman (1999) to be 0.12 ± 6% $cm^2\ s^{-1}$ at *T* = 0ºC and is dependent upon the temperature according to the function:

$$D_{GEM} = 0.1194\left(\frac{T}{T_0}\right)^{1.81} \; cm^2 s^{-1} \qquad (3.20)$$

Although the exact species that compose GOM are unknown and an area of active research, it is generally believed that GOM in the atmosphere is primarily composed of gaseous $HgCl_2$. Marsik et al. (2007) was able to recreate the results from Massman (1999) and used the same approach to calculate the molecular diffusivity for gaseous $HgCl_2$ and obtained an estimated value of $D_{GOM} = 0.09\ \mathrm{cm^2\ s^{-1}}$ with no further explanation of associated uncertainty. Massman (1999) shows that a fixed exponent value of $\alpha = 1.81$ can be used for all gases at standard temperature and pressure (STP) in Eq. 3.20. Therefore, the temperature dependence of the molecular diffusivity of GOM in air would follow the same form as that of GEM, (i.e., Eq. 3.20). It should be noted that for both studies referenced, the molecular diffusivity of mercury vapor in the atmospheric models were run for, and observations were taken at, STP. Thus, more site-specific values for D_{GEM} and D_{GOM} should be an area of future research.

3.2.2 Particles

Particles can be transported across the quasi-laminar sublayer by Brownian diffusion, impaction, and by interception. Brownian diffusion dominates for small particles while impaction dominates for large particles. An expression for the overall quasi-laminar resistance (R_b) for particles has been developed by Zhang et al. (2001):

$$R_b = \frac{1}{\varepsilon_0 u_* (E_B + E_{IM} + E_{IN}) R_1} \quad (3.21)$$

where $E_B, E_{IM},$ and E_{IN} are the collection efficiencies from Brownian diffusion, impaction, and interception, respectively. The correction factor, R_1, is introduced to represent the fraction of those particles that stick to the surface as opposed to those which bounce off upon impaction. ε_0 is an empirical constant and is taken to be 3 for all land use categories (Zhang et al. 2001).

For Brownian diffusion, there is evidence that E_B is related to the Schmidt number in the following manner:

$$E_b = Sc^{-\gamma} \quad (3.22)$$

Sc is calculated using Eq. 3.15 and γ represents the roughness of the surface. γ usually lies between 1/2 and 2/3 with the larger values for rougher surfaces (Zhang et al. 2001). A value of 1/2 for γ was chosen because the present model is for deposition onto the surface of the GSL, and 1/2 should be used for water surfaces (Slinn and Slinn 1980; Zhang et al. 2001).

The impaction of a particle onto a surface is governed by the Stokes number (*St*) (Gioegi 1986). *St* is a dimensionless number corresponding to the behavior of particles suspended in a fluid flow. *St* is defined as the ratio of the stopping distance of a particle to a characteristic dimension of the obstacle. For *St* >> 1, particles will continue in a straight line as the fluid flows around the obstacle and impact the obstacle. For *St* << 1,

particles will follow the fluid streamlines closely and avoid impacting the obstacle. Giorgi (1986) defines the Stokes number as:

$$St = \tau_{rel}\frac{u_*}{a} \quad (3.23)$$

for rough or vegetated surfaces and:

$$St = \tau_{rel}\frac{u_*^2}{\nu} \quad (3.24)$$

for smooth surfaces or surfaces with bluff roughness elements. Giorgi (1986) states that, "Brutsaert (1982) defines bluff roughness elements as 'impermeable obstacles with a height which is not large compared to their aspect width normal to the mean flow.' Surfaces with bluff roughness elements are, for example, developing water waves, irregular ice and snow surfaces, bare soil fields, and many urban environments." In these equations, a is a characteristic "projected radius" of the surface roughness elements, or collectors, and τ_{rel} is the relaxation time:

$$\tau_{rel} = \frac{V_s}{g} \quad (3.25)$$

where V_s is the settling velocity and g is gravity (Giorgi 1986, 1988; Zhang et al. 2001). Eq. 3.24 is used for deposition onto a smooth surface such as the GSL. ν is calculated using Eq. 3.19 and V_s will be discussed in Section 3.4.

There have been many proposed expressions for E_{IM}; however, the most common expressions are detailed in Zhang et al. (2001). The particular form adapted by Zhang et al. (2001) is that of Peters and Eiden (1992):

$$E_{IM} = \left(\frac{St}{\alpha + St}\right)^{\beta} \quad (3.26)$$

where $\beta = 2$ and α is dependent on land use category. Giorgi (1986) suggests a formula for impaction efficiency that is specific to smooth surfaces and surfaces with bluff roughness elements:

$$E_{IM} = \frac{St^2}{400 + St^2} \quad (3.27)$$

Giorgi (1986) derived this formula by processing the observational data of Liu and Agarwal (1974) through a two-layer model and producing an empirical fit to the model results. A side-by-side comparison of both methods shows that the Peters and Eiden (1992) method, using $\alpha = 100$ for the land use category of ocean, is a factor of 25 larger than the method of Giorgi (1986). However, for particles with aerodynamic diameters < 2.5 μm, E_B dominates over E_{IM} by three orders of magnitude. The current deposition model uses Eq. 3.27 because it was developed specifically for smooth surfaces and surfaces with bluff roughness elements such as the surface of the GSL.

According to theory, a particle may also be removed by interception with surface elements, denoted as interception efficiency (E_{IN}). An example of removal by interception would be a particle colliding with the hairs of a fuzzy leaf surface, cactus

needles, etc. Where the current deposition model is calculating the deposition onto the water surface of the GSL, the collection efficiency from interception is assumed to be zero. In the case that the current model may be adapted to suit different situations, further explanation and mathematical representation may be found in Slinn (1982), Giorgi (1988), and Zhang et al. (2001), with a brief synopsis in Seinfeld and Pandis (2006, p. 910).

The correction factor in Eq. 3.21 (R_1) is introduced to represent the fraction of those particles which stick to the surface. An estimate for the fraction of particles that stick to the surface was suggested by Slinn (1982) as:

$$R_1 = exp(-St^{0.5}) \qquad (3.28)$$

As *St* approaches 0, R_1=1. It has been suggested that particles with aerodynamic diameters < 5 μm lack enough inertia to rebound from a surface (Zhang et al. 2001). Also, if the surface is wet, particles are assumed to stick to the surface regardless of size (Seinfeld and Pandis 2006, p. 910). The in situ measurements of particulate mercury are limited to particles with aerodynamic diameters < 2.5 μm (see Sections 2.2.2 and 2.2.3). Therefore, the current deposition model is limited to smaller particles that are impacting a water surface and $R_1 = 1$.

3.3 Surface Resistance (R_c)

The surface resistance for dry deposition of gases to water was modeled following closely the process outlined by Seinfeld and Pandis (2006, 911–918). It should be noted that the model for the surface resistance of gases onto a water surface is significantly

different from the model for dry deposition of gases onto vegetation or any other surface. For the calculation of R_c for dry deposition of gases onto vegetation and other surfaces, or land use types, the reader is referred to Wesely (1989).

The transfer of a species from the gas-phase to the liquid-phase at an air-liquid interface is traditionally represented using a two-film model. To implement the two-film model, the gas is assumed to be well-mixed as it is transported to the water's surface by turbulent transport in the atmosphere, allowing for the concentrations at the boundaries to remain constant long enough that the concentration profile reaches a steady state. The two-film model also uses the assumption that the chemical does not undergo any reaction within the layers (Poissant et al. 2000). Immediately above the air-water interface is a stagnant film where the concentration of the species is altered by the concentration of the species in the water. The water may act as a source or a sink to change the concentration of the species across this microlayer depending on the concentration on either side of the interface. All the resistance to mass transfer in the gas-phase is assumed to occur in this thin film adjacent to the air-water interface. Similarly, on the underside of the air-water interface, it is assumed that all the resistance to mass transfer of the dissolved gas away from the interface into the bulk liquid is confined to a thin stagnant layer of liquid just below the air-water interface. At the interface, the partial pressure of the species in the gas-phase (P_A) is in equilibrium with the concentration of the species in the liquid-phase (C_A).

The gas-phase flux (F) of the species across the thin stagnant layer to the interface may be represented by a gas-phase mass transfer coefficient (Seinfeld and Pandis 2006, p. 915):

$$F = k_G\left(P_{A_G} - P_{A_i}\right) \quad (3.29)$$

where k_G is the gas-phase mass transfer coefficient, P is the partial pressure, and the subscripts A_G and A_i indicate the species as a gas in the atmosphere and at the air-water interface, respectively. Likewise, the liquid-phase flux away from the air-water interface into the bulk liquid can be represented using a liquid-phase mass transfer coefficient:

$$F = k_L\left(C_{A_i} - C_{A_L}\right) \quad (3.30)$$

where k_L is the liquid-phase mass transfer coefficient, C is the liquid-phase concentration and the subscripts A_G and A_i are the same as in Eq. 3.29.

In steady state, the flux of the species across the stagnant layer to the air-water interface and away from the interface must be equal. In other words, the partial pressure of the species in the gas-phase at the interface, P_{A_i}, must equal the interfacial concentration of the species in the liquid-phase, C_{A_i}. However, the partial pressures and concentrations exactly at the interface are usually not known, so, according to Seinfeld and Pandis (2006), "it is customary to express the flux in terms of *overall* mass transfer coefficients," K_G and K_L as:

$$F = K_G\left(P_{A_G} - P_A^*\right) = K_L(C_A^* - C_{A_L}) \quad (3.31)$$

where P_A^* is the gas-phase partial pressure that would be in equilibrium with the bulk liquid-phase concentration $\left(C_{A_L}\right)$ and C_A^* is the liquid-phase concentration that is in

equilibrium with the bulk, or free-atmospheric, partial pressure of the species. Therefore, these may be related to one another using Henry's law.

Henry's law states that if a species is in equilibrium between gas and aqueous phases, the amount of solute (in moles) present in a given amount (usually 1 liter) of the saturated solution can be related to the partial pressure of the surrounding, or adjacent gas, by a Henry's law coefficient in the following manner:

$$H_A = \frac{[A(aq)]}{P_A} \qquad (3.32)$$

where A indicates the species, P_A is the partial pressure (usually in atm), and the square brackets indicate a concentration ($\mathrm{mol\,L^{-1}}$). The unit $\mathrm{mol\,L^{-1}}$ is usually expressed as M, or the molarity or molar concentration. Therefore, the Henry's law coefficient usually has the units of $\mathrm{M\,atm^{-1}}$ (Hobbs 2000, 121–123; Seinfeld and Pandis 2006, 286–291).

Using Henry's law to relate the gas-phase partial pressure and the liquid-phase yields:

$$C_A^* = P_{A_G} H_A \qquad (3.33)$$

$$P_A^* = \frac{C_{A_L}}{H_A} \qquad (3.34)$$

These relations can indicate the direction of the flux (from gas-to-liquid-phase, or vice-versa). If $C_{A_L} < H_A P_{A_G}$, then the net flux of species A is from the bulk gas-phase to the

bulk liquid-phase. In the case that the opposite is true (i.e., $C_{A_L} > H_A P_{A_G}$), the net flux will be from the liquid-phase to the gas-phase.

It is assumed in the current mercury dry deposition model that the net flux is always from the gas-phase to the liquid-phase. Most established dry deposition models assume a unidirectional surface flux (Wesley and Hicks 2000). Anderson et al. (2008) showed that the Henry's law coefficient for GEM is slightly higher for saltier water, providing less opportunity for the evasion of GEM from the surface of the GSL. However, recent flux measurements of GEM strongly suggest bidirectionality (Poissant et al. 2000; Converse et al. 2010) and even with a larger Henry's law coefficient, a unidirectional flux may be an invalid assumption. Preliminary examination of the Henry's law coefficient with GEM and GOM concentrations indicate that this assumption is probably valid most of the time. However, due primarily to the facts that the Henry's law coefficient is temperature dependent, the concentrations of GEM and GOM are ever-changing, and the exact chemistry of GOM and the mercury interaction with the very salty surface layer of the GSL are unknown, the direction of the flux based on chemical processes and Henry's law should be an area of future research.

Upon substitution of Eqs. 3.33 and 3.34 into Eq. 3.31, the flux of mercury across the interface can be defined as:

$$F = K_G \left(P_{A_G} - \frac{C_{A_L}}{H_A} \right) = K_L (P_{A_G} H_A - C_{A_L}) \qquad (3.35)$$

which indicates that the two overall mass transfer coefficients are related through the Henry's law coefficient as:

$$K_L = \frac{K_G}{H_A} \qquad (3.36)$$

This allows the surface resistance to be defined as either $R_c = \frac{1}{K_G}$ or $R_c = \frac{1}{K_L}$. Now the overall mass transfer coefficients can be related to the individual mass transfer coefficients so that the resistances can be clearly defined. Seinfeld and Pandis (2006, p. 916) show that from Eqs. 3.34, 3.35, and the relation $C_{A_i} = H_A P_{A_i}$ (the interface must be in equilibrium) that:

$$\frac{1}{K_G} = \frac{1}{k_G} + \frac{1}{k_L H_A} \qquad (3.37)$$

$$\frac{1}{K_L} = \frac{H_A}{k_G} + \frac{1}{k_L} \qquad (3.38)$$

These relations indicate that for a highly soluble gas, such as GOM, for which $H_A \gg \frac{k_G}{k_L}$, the gas-phase mass transport controls the deposition process, whereas for a slightly soluble gas, such as GEM, the liquid-phase mass transport dominates.

Up to this point, the gas-phase concentration has been defined in units of a partial pressure so that the Henry's law coefficient would be in units of M atm^{-1}. However, the units of the individual and overall mass transfer coefficients need to be in cm s^{-1}. Thus, gas-phase concentration must be expressed in units of mol cm^{-3}, which furthermore requires that the Henry's law coefficient must be dimensionless. The Henry's law

coefficient can be made dimensionless by $\widetilde{H}_A = H_A RT$ which has units of $\frac{mol\ A(gas)\ cm^{-3}}{mol\ A(liquid) cm^{-3}}$. For example, at 298 K, $\widetilde{H}_A = 24.44 H_A$ (Seinfeld and Pandis 2006, p. 917).

For use in the current dry deposition model, a dimensionless Henry's law coefficient was calculated for GEM using a best fit equation to laboratory measurements of Andersson et al. (2008). Andersson's experiments were conducted at five different temperatures between 278 K and 308 K and direct measurements of the partitioning of mercury were taken in the gas- and aqueous-phases. The measurements were repeated using pure water, sea water (~0.6 M NaCl), and for a 1.5 M NaCl solution to account for a salting-out effect for elemental mercury (The GSL is approximately 2.6 M NaCl, making the 1.5 M solution a better fit than the sea water solution). The fit used for a 1.5 M NaCl solution is:

$$\widetilde{H}_A = exp\left(\frac{-1871.6}{T} + 5.28\right) \qquad (3.39)$$

where *T* used is the surface temperature of the GSL in Kelvin [calculated using an equation for GSL temperature as a function of day of the year (Crosman and Horel 2009)].

The general form of the surface resistance to deposition of a gas onto a water surface is therefore:

$$R_c = \frac{1}{k_G} + \frac{1}{k_L \widetilde{H}_A} \qquad (3.40)$$

Hicks and Liss (1976) show that k_G is about 0.13% of the wind speed at a 10 m reference height. For wind speeds between 3 and 15 m s^{-1}, values of k_G range from 0.4 to 2 cm s^{-1}. Seinfeld and Pandis (2006, p. 917) show the two most widely used relationships between k_L and wind speeds are those of Liss and Merlivat (1986) and Wanninkhof (1992). The current dry deposition model uses the relationship from Liss and Merlivat (1986) (i.e., Eq. 3.40) because it accounts for the roughness and turbulent mixing of the water due to increased wind speed. Thus:

$$k_L = \begin{cases} 0.17 u_{10} S_A^{2/3} & u_{10} \leq 3.6\ m\ s^{-1} \\ 0.612 S_A^{2/3} + (2.85 u_{10} - 10.26) S_A^{1/2} & 3.6 < u_{10} \leq 13\ m\ s^{-1} \\ 0.612 S_A^{2/3} + (5.9 u_{10} - 49.9) S_A^{1/2} & u_{10} > 13\ m\ s^{-1} \end{cases} \quad (3.41)$$

where u_{10} is the wind speed at 10 m, and S_A is the ratio of the *Sc* for CO_2 at a temperature of 293 K over the *Sc* of the species of interest, (i.e., elemental mercury in water), at the temperature of interest:

$$S_A = \frac{Sc_{CO_2}(293\ K)}{Sc_{Hg(aq)}} \quad (3.42)$$

Wanninkhof (1992) gives the value of $Sc_{CO_2}(293\ K)$ to be 660. $Sc_{Hg(aq)}$ is calculated from Eq. 3.16 using a saltwater viscosity model developed by Isdale et al. (1971), and the diffusivity calculated using the method of Kuss et al. (2009). There are many uncertainties associated with the current model, especially in application of models developed for the ocean being applied to the GSL. For example, Wanninkhof (1992) points out surfactants can have a large inhibitory effect on gas transfer which is not

accounted for in this model. The presence of surfactants is a bigger issue in the saltier north arm of the GSL. Thus, gas transfer across the air-water interface of the GSL, with the specific chemistry and behavior of the lake in account, should be an area of future research.

3.4 Settling Velocity (V_s)

The particle settling velocity is given by Seinfeld and Pandis (2006) as:

$$v_s = \frac{D_p^2 \rho_p g C_c}{18\mu} \qquad (3.43)$$

where D_p is the aerodynamic diameter of the particle, ρ_p is the particle density, g is gravity, C_c is a slip correction factor that is introduced as part of Stokes drag force and will be discussed shortly, and μ is the dynamic viscosity of the air calculated from Eq. 3.18.

Keeler et al. (1995) attempted to measure a size distribution of PBM in urban Detroit, Michigan, and found that the distribution was bimodal with an obvious fine and coarse mode. The average PBM particle size of the fine and coarse modes were 0.68 μm and 3.78 μm, respectively. Although it may not be a safe assumption that the size distribution at an urban site is the same as at UT96, the aerodynamic diameter of 0.68 μm is used in the current deposition model as a reasonable "best guess." An exact, and site-specific, size distribution of PBM would eliminate this uncertainty and should be an area of future research.

With no guidance with respect to a density distribution of PBM in the literature, a "best guess" of 2 g cm^{-3} ± 1 g cm^{-3} was chosen for the model simply because intuition tells us that PBM will be denser than water. An upper bound of 3 g cm^{-3} was chosen for symmetry. An exact, and site-specific, density distribution of PBM would eliminate this uncertainty and should be an area of future research.

C_c is the slip correction factor that is introduced from Stokes' law to account for noncontinuum effects that become important as D_p becomes very small (Seinfeld and Pandis, 2006, p. 407). It is calculated as:

$$C_c = 1 + \frac{2\lambda}{D_p}\left[1.257 + 0.4exp\left(-\frac{1.1D_p}{2\lambda}\right)\right] \quad (3.44)$$

where λ is the mean free path of the gas (or other suspension medium) and is calculated as:

$$\lambda = \frac{2\mu}{p\left(\frac{8M}{\pi RT}\right)^{1/2}} \quad (3.45)$$

where p is pressure (in Pa), μ is the dynamic viscosity of the gas calculated using Sutherland's formula as described in Eq. 3.18 , R is the universal gas constant in units of J K^{-1} mol^{-1}, T is temperature in K and M is the molecular weight of the gas in kg mol^{-1} (Seinfeld and Pandis 2006, p. 407).

The slip correction factor is generally neglected for particles with aerodynamic diameters > 10 μm as the correction is less than 2%. On the other hand, the drag force for a 0.1μm particle is reduced by almost a factor of 3 as a result of this slip correction factor

(Seinfeld and Pandis 2006, p. 407). At the best guess value of D_p = 0.68 μm at STP, $C_c \approx 1.24$. At the elevation of the UT96 site, C_c has a mean value of 1.73.

CHAPTER 4

THE FLUX OF MERCURY INTO THE GREAT SALT LAKE

This chapter will use speciated atmospheric mercury and 3-D sonic anemometer measurements collected at the UT96 site in conjunction with a resistance-in-series dry deposition model to estimate the dry deposition of Hg to the GSL for a 1-year period (i.e., July 1, 2009 through June 30, 2010). The dry deposition flux estimates will then be compared to the riverine influx and the wet deposition of Hg to determine which pathway is dominant. Recall that the downward Hg flux is calculated by multiplying the deposition velocity of each Hg species by its corresponding ambient (atmospheric) mercury concentration. This procedure yields a flux, in units of ng m^{-2} h^{-1}, that must be integrated over time to get a total flux in units of ng m^{-2}.

This section will begin with the dry deposition velocity (V_d) results from the resistance-in-series model. This will be followed by an abbreviated summary of the measured concentrations of the atmospheric mercury (*C*) and the downward mercury flux (*F*) as the product of V_d and *C*. The final sections of this chapter will compare the dry deposition flux of mercury into the GSL to the wet deposition flux and the riverine input.

4.1 Dry Deposition Velocity

The dry deposition velocity of a tracer in the atmosphere is calculated as the inverse of a series of atmospheric resistances as shown in Eq. 3.2. Figures 4.1, 4.2, and 4.3 show a time series of the individual resistances (i.e., $R_a, R_b,$ and R_c) and the deposition velocity (V_d) for the entire measurement period for GEM, GOM, and PBM, respectively.

V_d for GEM is most affected by the transfer of Hg vapor across the air-water interface, R_c. This transfer of gas across the air-water interface is highly dependent upon the Henry's law coefficient for Hg vapor and salt water. The Henry's law coefficient is a function of water temperature. Thus, as shown in Fig. 4.1, R_c becomes larger during the winter months. Throughout the year, R_c is the largest of the resistances and acts as the limiting factor to the magnitude of V_d for GEM. The average V_d for GEM was ~ 0.02 cm s^{-1}. The literature suggests a general range of V_d for GEM of 0.015 cm s^{-1} to 0.1 cm s^{-1} (Landis et al. 2005; Lin et al. 2006).

GOM has a much smaller average R_c than GEM (Fig 4.2) because it is a much more soluble gas that is more readily absorbed by the lake surface. R_a and R_b seem to be smaller for GOM (Fig 4.2), but have been calculated in the same manner for both GOM and GEM. The discrepancy is most likely a result of different averaging times for the two species (recall that GEM measurements are taken every 5 minutes and have been averaged to half-hour intervals, whereas GOM measurements have been taken once every 3 hours and the wind data have been averaged accordingly). Therefore, with smaller resistances, the V_d for GOM is largest, with an average value around 0.21 cm s^{-1}. The literature suggests using the V_d for HNO_3 as a surrogate V_d for GOM because it has a

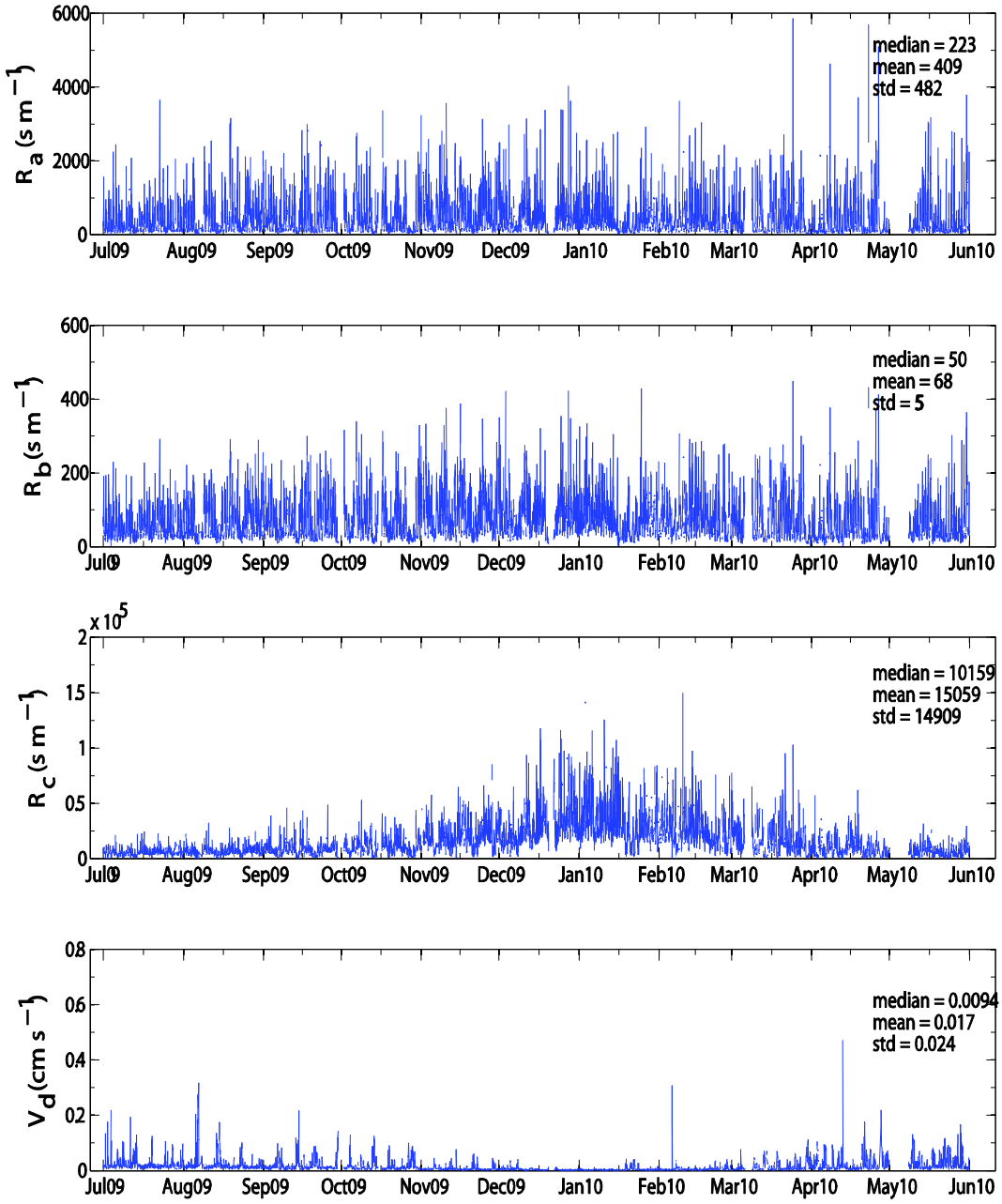

Figure 4.1. A time series of the three modeled resistant components ($R_a, R_b,$ and R_c) and dry deposition velocity (V_d) for GEM from July 1, 2009 through June 30, 2010 at the UT96 site.

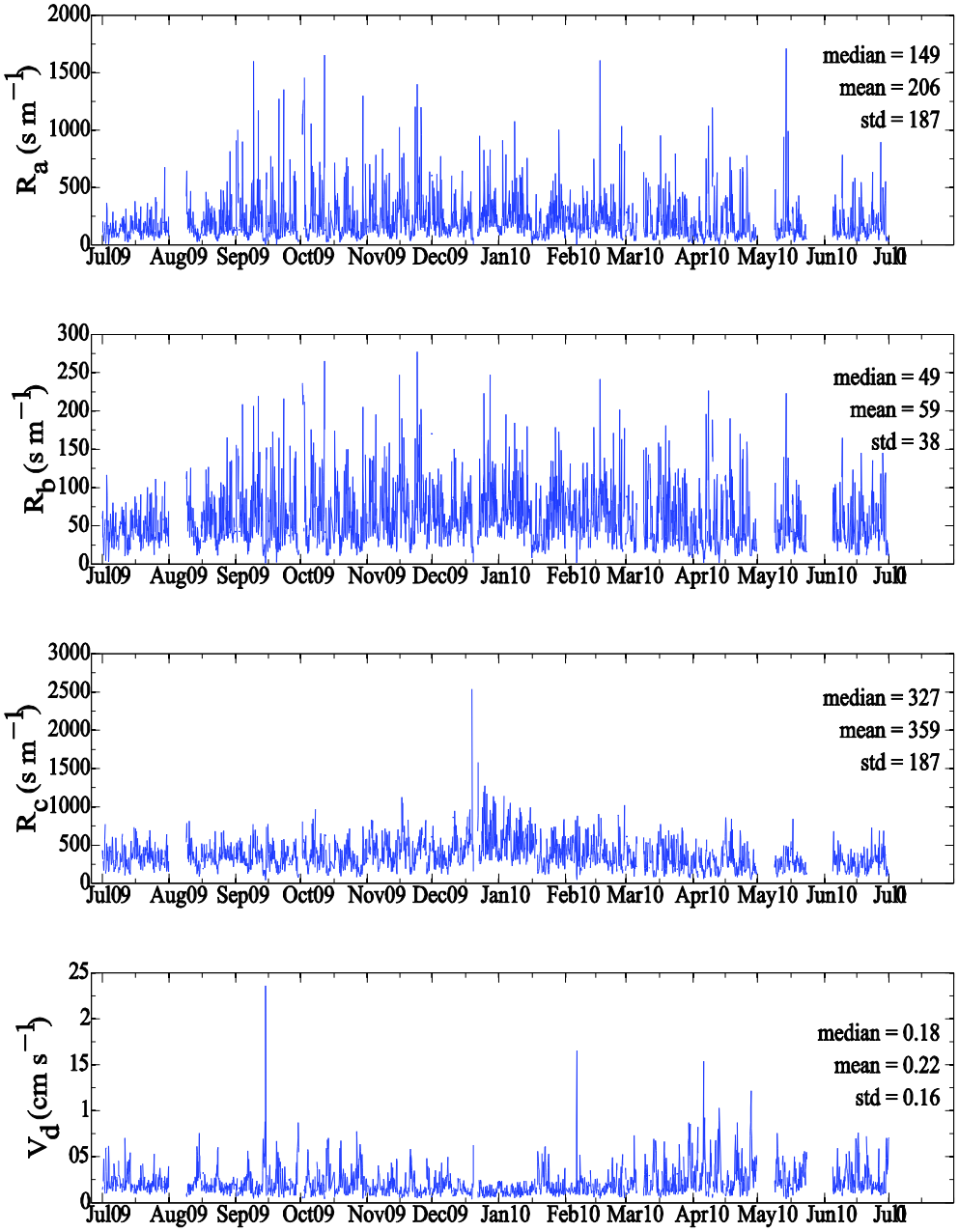

Figure 4.2. Similar to Fig. 4.1 but for GOM.

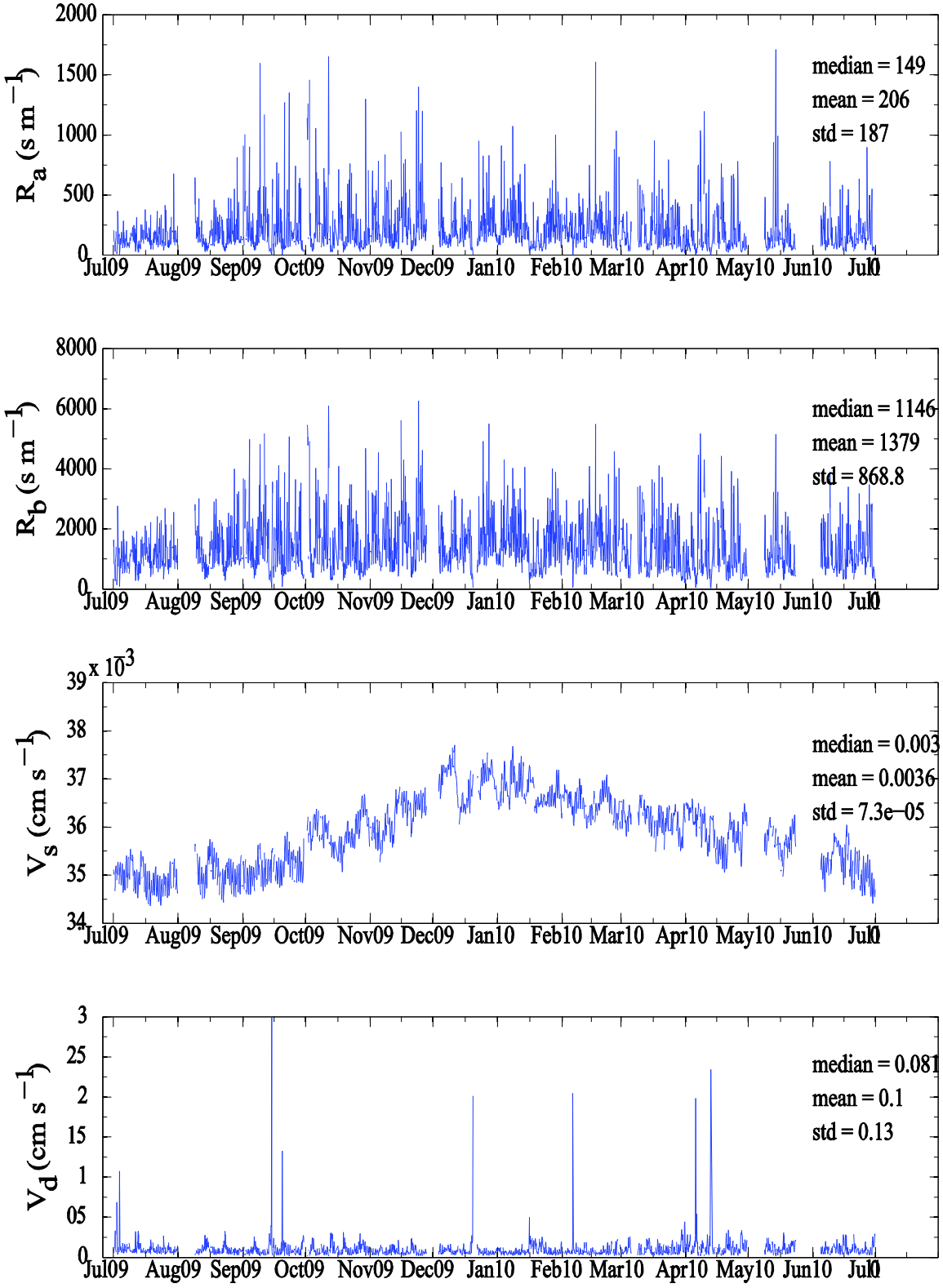

Figure 4.3. Similar to Figs. 4.1 and 4.2 but for PBM.

similar Henry's law coefficient. This substitution produces a range for V_d of 0.5 cm s^{-1} to 4 cm s^{-1} (Lin et al. 2006).

For PBM, the resistance from the quasi-laminar boundary layer immediately above the surface is the largest (Fig 4.3). The large R_b values come about from the inverse relationship of this resistance on the diffusivity of the particles. Furthermore, the diffusivity (Brownian diffusivity for the particulate case) is inversely proportional to the particle size making the resistance directly proportional to particle size. Furthermore, R_c is zero for PBM and V_s is significant. The average V_d for PBM was 0.21 cm s^{-1}. The literature usually treats V_d for PBM as that of any fine (e.g., accumulation mode size regime) particle.

Figure 4.4 shows the monthly-averaged V_d for GEM, GOM, and PBM. In the winter months, the boundary layer is mostly stable due to surface layer inversions. During this time period, V_d decreases primarily because R_a increases significantly during very stable periods. The V_d for GOM and PBM is most sensitive to atmospheric stability changes. Therefore, V_d for GOM and PBM peak in the spring and fall when synoptic-scale frontal passages are common. The V_d for GOM and PBM are also consistently high in the summer when warmer surface temperatures produce boundary layer turbulence. The larger summertime values of V_d for GEM most likely result from warmer lake surface temperatures which would result in a higher Henry's law coefficient.

V_d also exhibits a diurnal pattern that follows the pattern of increased turbulence in the afternoon. Figure 4.5 shows the daily cycle of V_d for GOM averaged over every day throughout the seasons. The maximum in V_d occurs in the midafternoon with higher

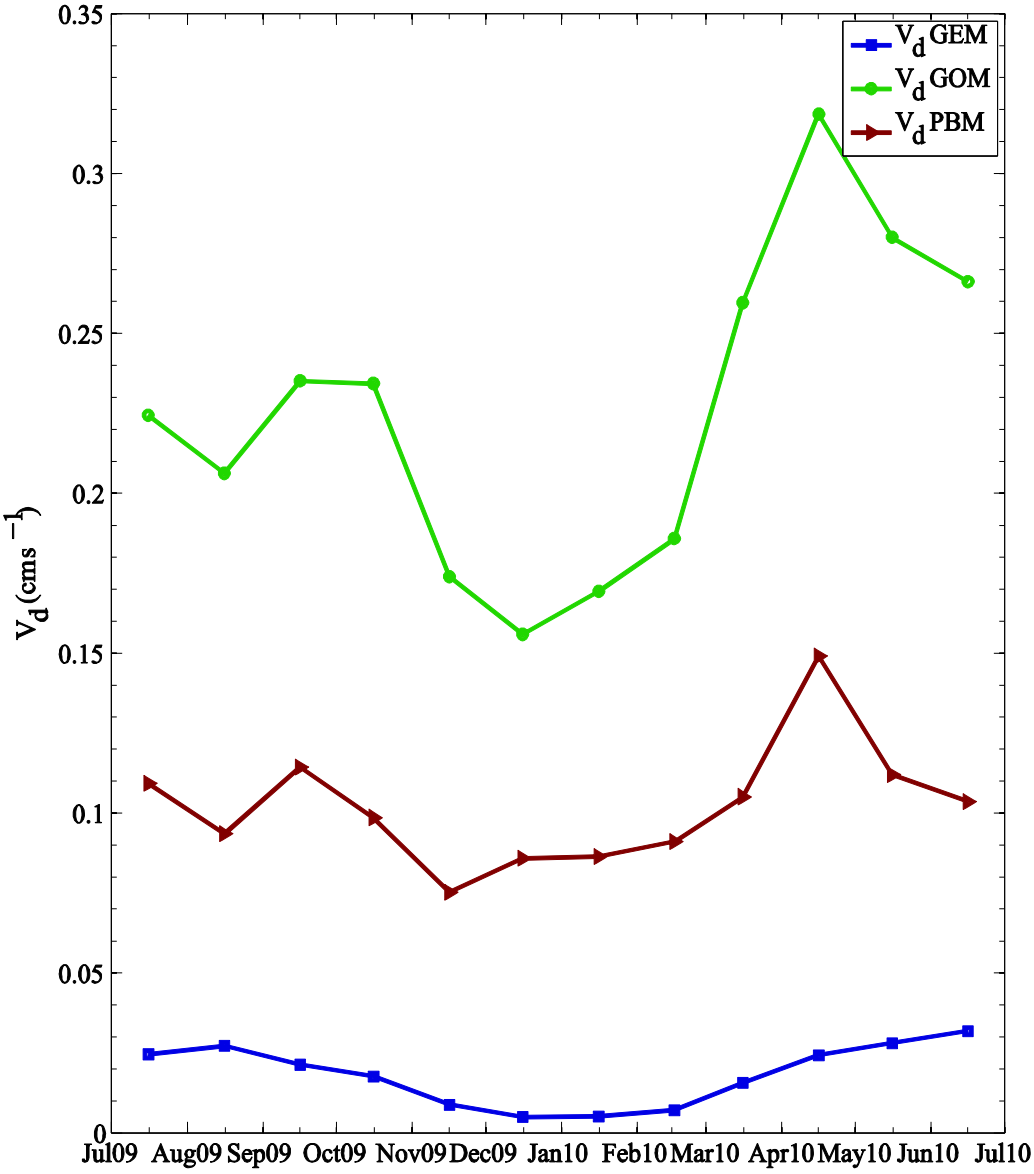

Figure 4.4. Monthly-averaged V_d for GEM, GOM, and PBM for the 1-year period from July 1, 2009 through June 30, 2010 at the UT96 site

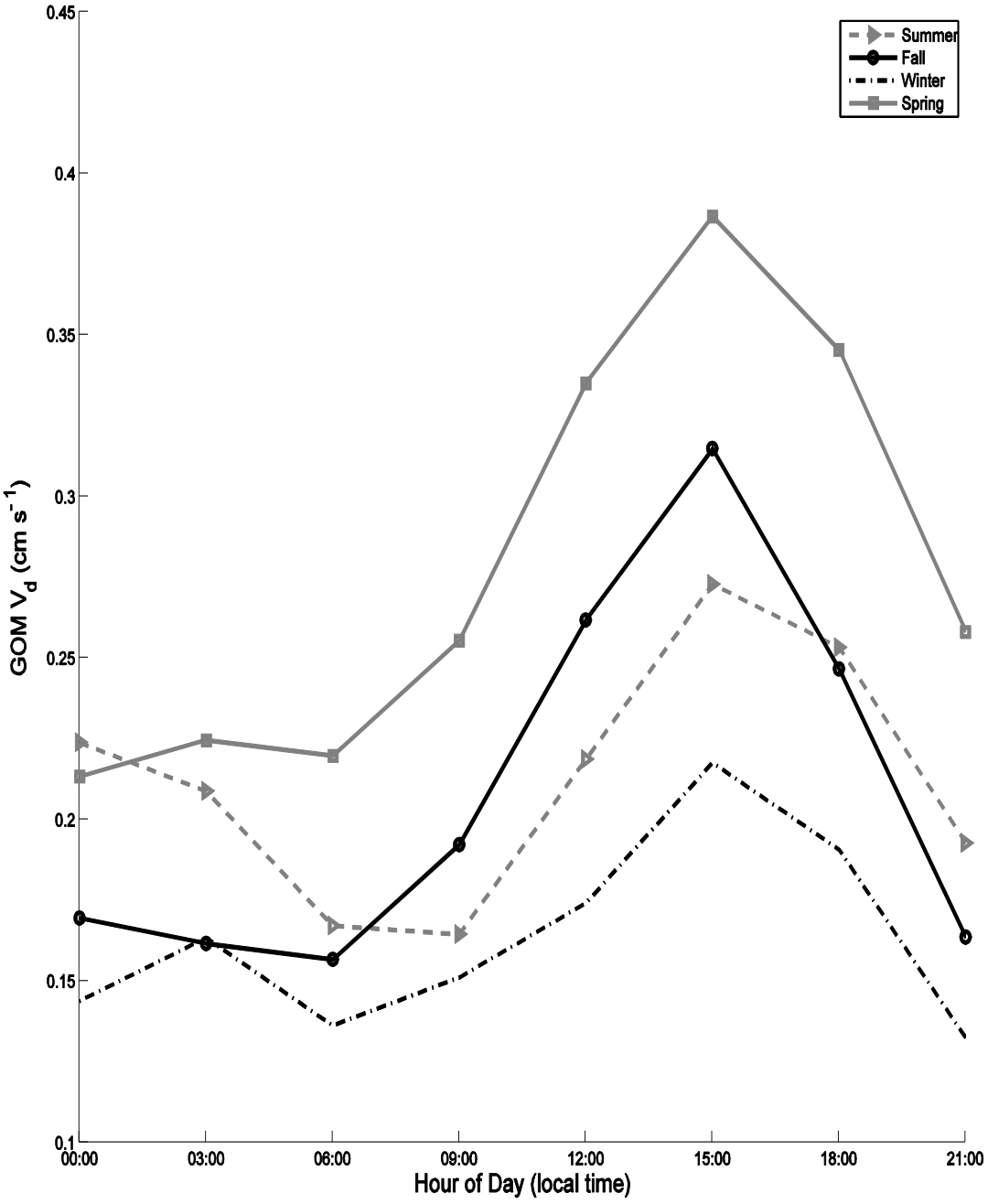

Figure 4.5. The diurnal pattern of the deposition velocity of GOM for all four seasons.

V_d values in the spring and fall. GEM and PBM exhibit a similar pattern but less pronounced.

4.2 Mercury Concentrations

4.2.1 GEM

Figure 4.6a shows the 2-hr-averaged GEM concentrations and the global background (indicated by the dashed line). The term global background, or global pool, of mercury is referring to the concentration of Hg from all sources (both natural and anthropogenic) that is always present in the atmosphere because of the long residence time of GEM (Lindberg et al. 2007). While all sources of mercury are "local," all sources have the capacity to contribute to the global pool because of the long residence time of GEM. The global background concentrations exhibit a slight seasonal variability with lowest values in the late summer when both deposition velocity and conditions for potential photochemical oxidation of GEM are high. The GEM global background peaks in late winter when conditions for GEM removal are not as ideal as in summer months. The global background of GEM in the northern hemisphere is currently taken to be 1.5 ± 0.2 ng m^{-3} (Lindberg et al. 2007). The uncertainty in background measurements comes from seasonal variability and from the difficulty in separating measurements of GEM from the global background pool from measurements of local/regional GEM.

From our measurements, the average GEM concentration for the measurement period is 1.60 ng m^{-3} which is within the global background uncertainty range. Figure 4.6b shows the monthly-averaged GEM concentrations with the global background also indicated. In Figures 4.7a and 4.7b, the global background has been subtracted from the

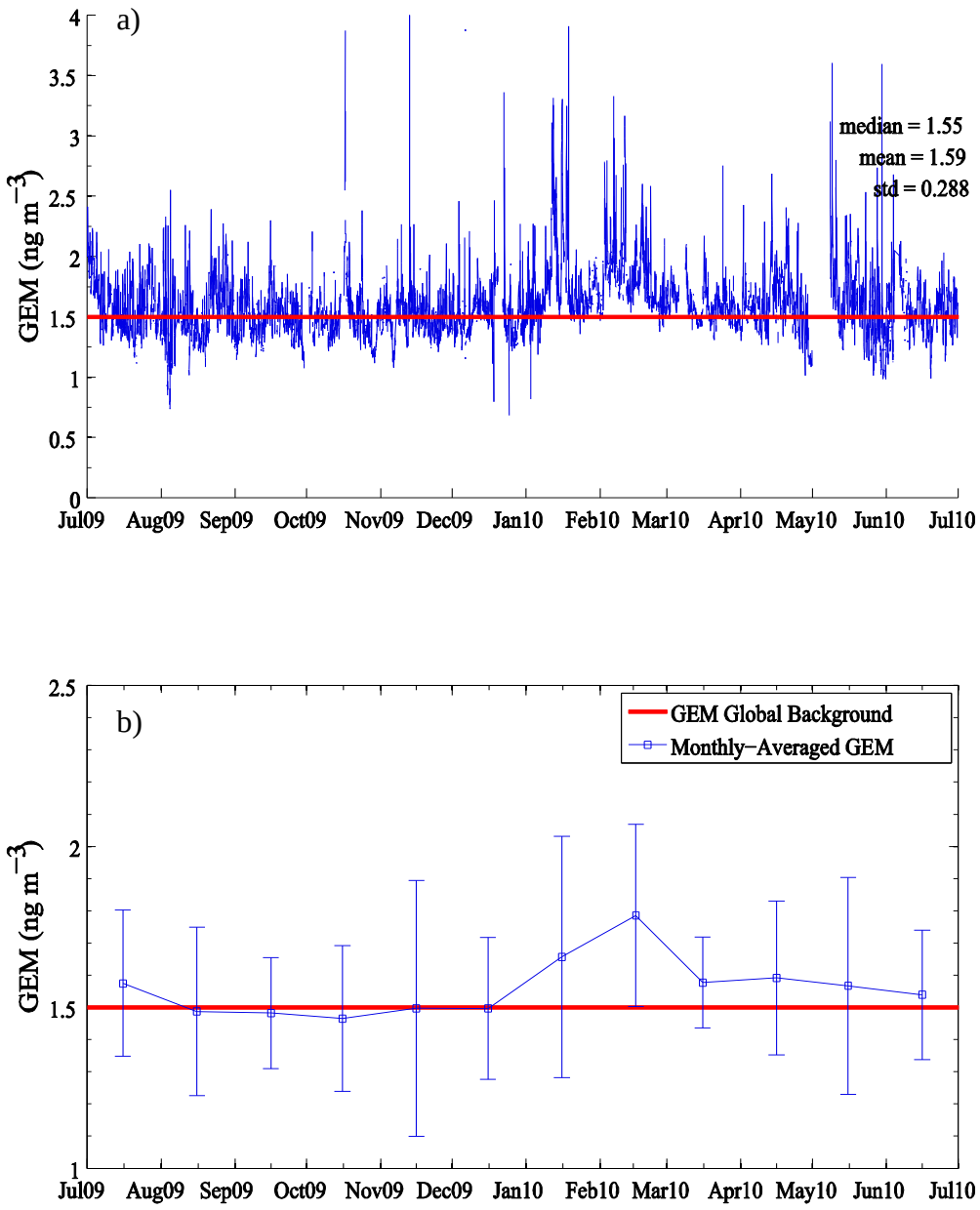

Figure 4.6. A time series of (a) the measured 2-hr-averaged GEM concentrations and (b) the monthly-averaged GEM concentrations in ng m^{-3} at the UT96 site with the GEM global background marked with the dashed line. The GEM global background concentration was set at a constant value of 1.5 ng m^{-3}.

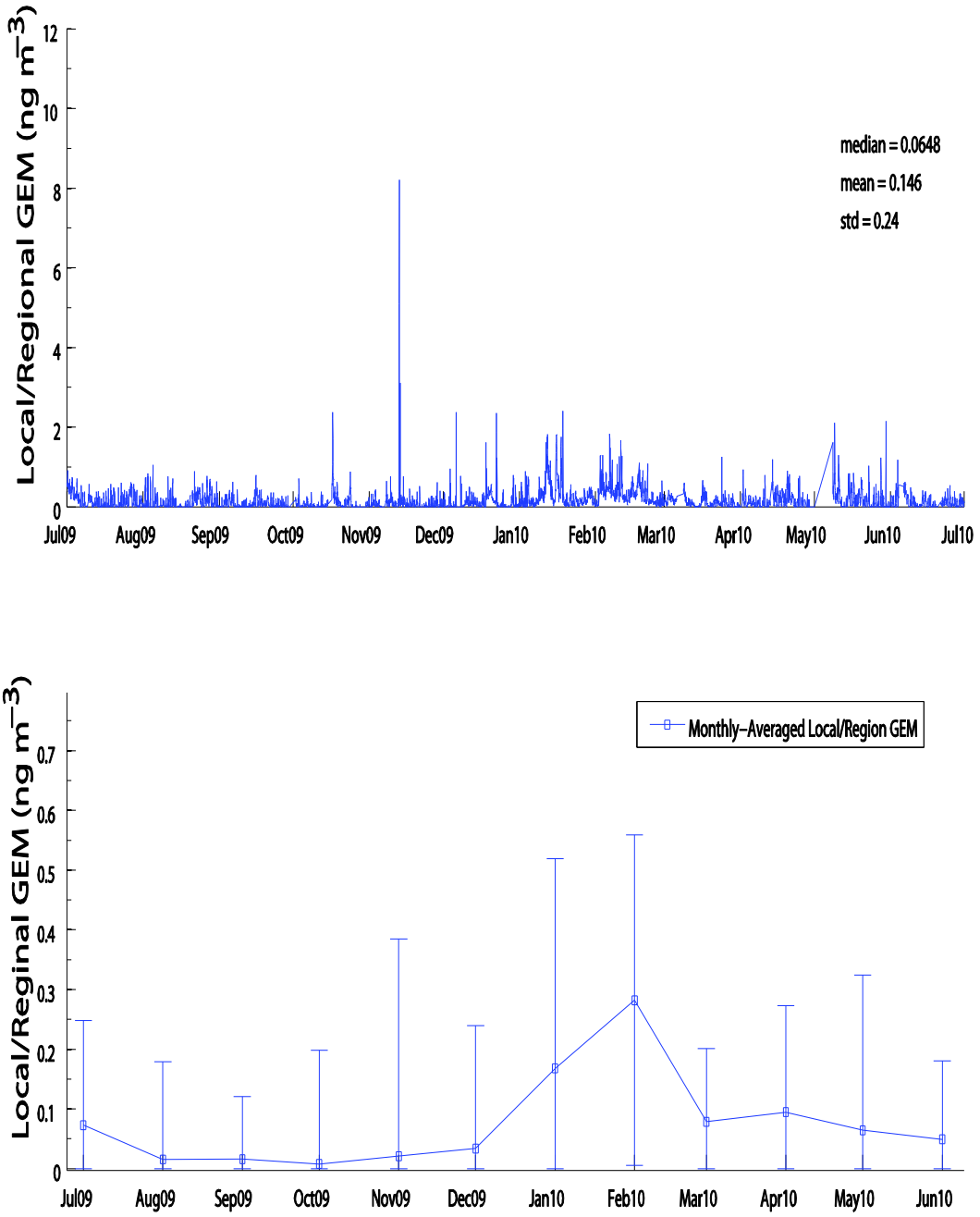

Figure 4.7. A time series of (a) the 2-hr-averaged GEM concentrations and (b) the monthly-average GEM concentrations in ng m^{-3} at the UT96 site with the GEM global background removed. The GEM global background concentration was set at a constant value of 1.5 ng m^{-3}.

measured GEM concentration, indicating the amount of mercury contribution that may be attributed to local/regional sources. We will later consider the downward fluxes of GEM from the global background pool and local/regional sources separately.

4.2.2 GOM

The 2-hr-averaged GOM concentrations are shown in Figure 4.8a along with the monthly-averaged GOM values shown in Figure 4.8b (both in units of $\mathrm{pg\,m^{-3}}$). Due primarily to the small residence time of around 1-2 weeks in the atmosphere, GOM is often considered to originate from local/regional sources. However, the exact sources of these species are not yet known. It may be possible that GOM is present in the upper troposphere and is mixed down to the surface by entrainment into the boundary layer which may account for higher levels of GOM in the summer months (Banic et al. 2003; Hedgecock and Pirrone 2004; Weiss-Penzias et al. 2009). It may also be possible that GOM is formed secondarily through photochemical reactions with GEM and other species near the surface (Hedgecock and Pirrone 2004; Peterson and Gustin 2008). In either case, GOM would not be considered from local sources. There are still many uncertainties regarding the formation and transport of GOM and this should be an area of future research.

4.2.3 PBM

The 2-hr-averaged PBM concentrations are shown in Figure 4.9a along with the monthly-averaged values in Figure 4.9b, (both in units of $\mathrm{pg\,m^{-3}}$). The higher concentrations of PBM in the winter most likely result from the surface-layer temperature inversions which effectively trap the local, urban pollution in a relatively shallow layer

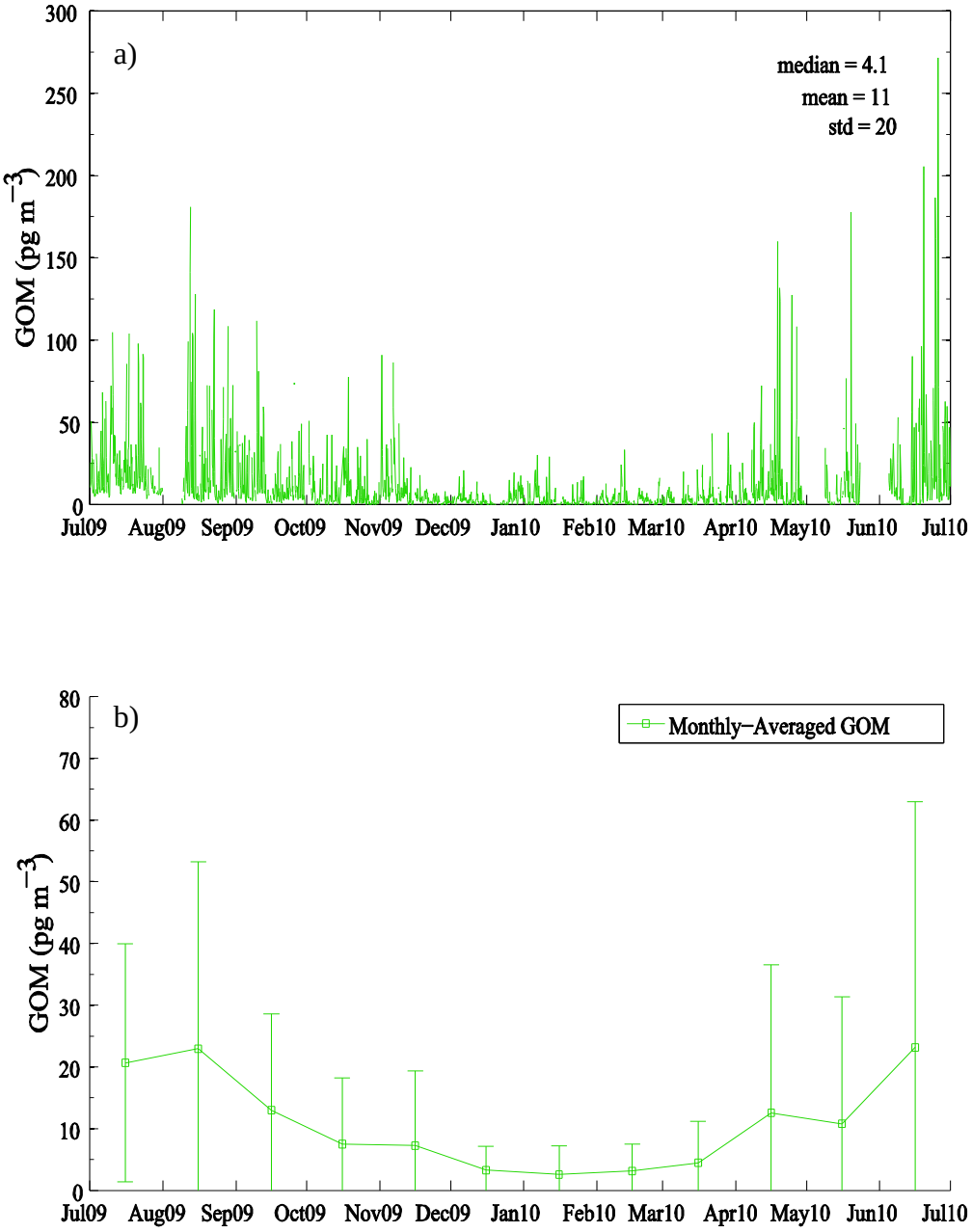

Figure 4.8. A time series of (a) the 2-hr-averaged GOM concentrations and (b) the monthly-averaged GOM concentrations in pg m^{-3} at the UT96 site.

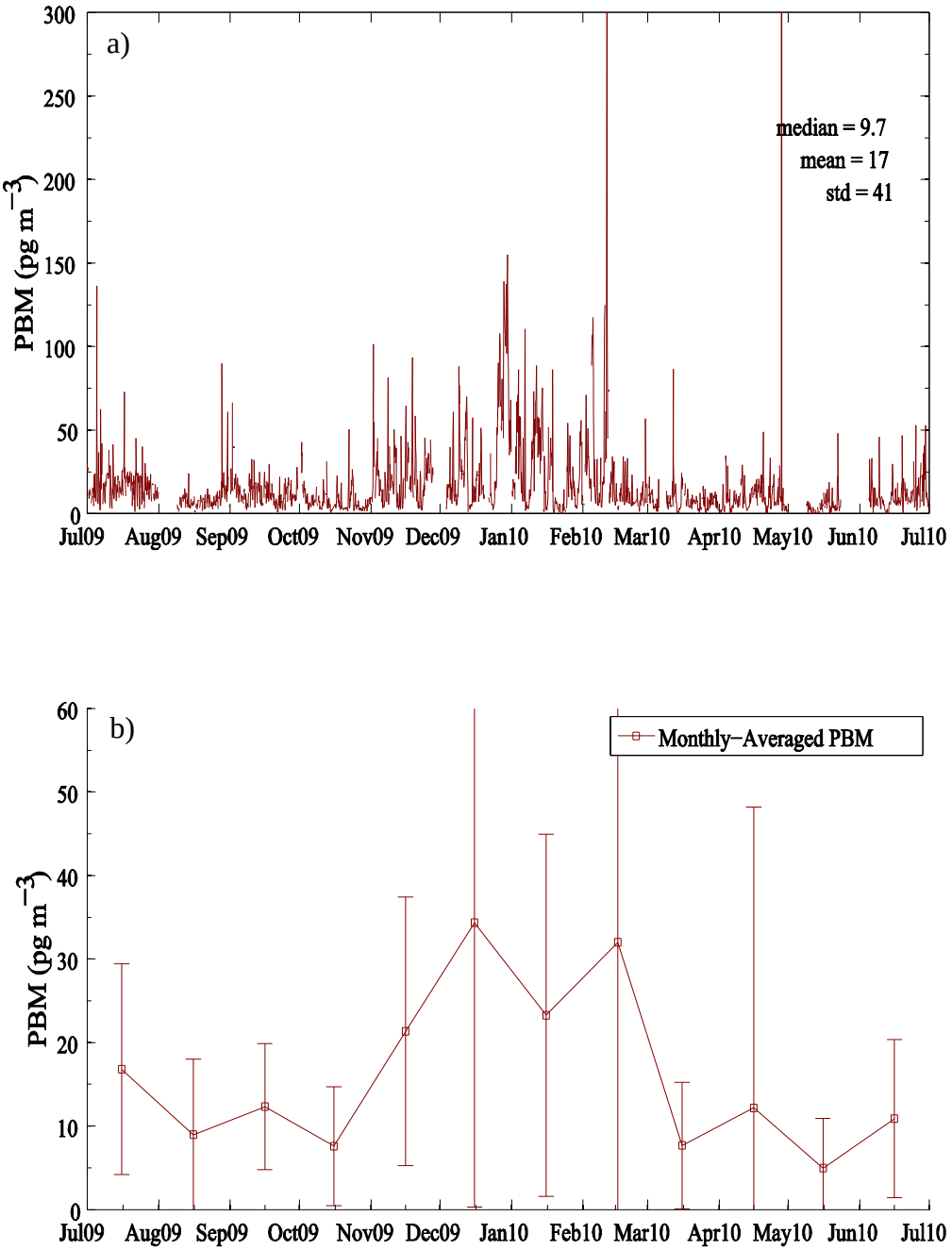

Figure 4.9. A time series of (a) the 2-hr-averaged PBM concentrations and (b) the monthly-average PBM concentrations in pg m^{-3} at the UT96 site.

near the surface. Not only is particulate matter increased during these inversions, but cold temperatures encourage condensation of mercury onto particles (Lynam and Keeler 2005).

4.3 Mercury Dry Deposition Flux

The flux of mercury onto the surface is calculated using Eq. 3.1. Figures 4.10, 4.11, and 4.12 show the time series of the calculated fluxes throughout the measurement period for GEM, GOM, and PBM, respectively. It should be noted that the concentrations of GOM and PBM have been converted from $\mathrm{pg\,m^{-3}}$ to $\mathrm{ng\,m^{-3}}$ prior to the fluxes being calculated to give all the fluxes consistent units of $\mathrm{ng\,m^{-2}\,h^{-1}}$. Tables 4.1, 4.2, and 4.3 show the final results of the model-calculated fluxes for GEM, GOM, and PBM, respectively. The total GEM was also broken down into fluxes from the local/regional sources and fluxes calculated using $1.5 \pm 0.2\ \mathrm{ng\,m^{-3}}$ to represent the global background in Table 4.1.

The dry deposition flux of mercury, as measured at UT96, is dominated by GEM with the total GEM making up on average 88% of the flux and GOM and PBM making up only an average of 12% collectively over the measurement period (Figs. 4.13 and 4.14). However, about 2.5% of the measured fluxes are derived from individual GOM and PBM events (i.e., > 3 standard deviations above the mean) which should not be ignored (Fig. 4.15).

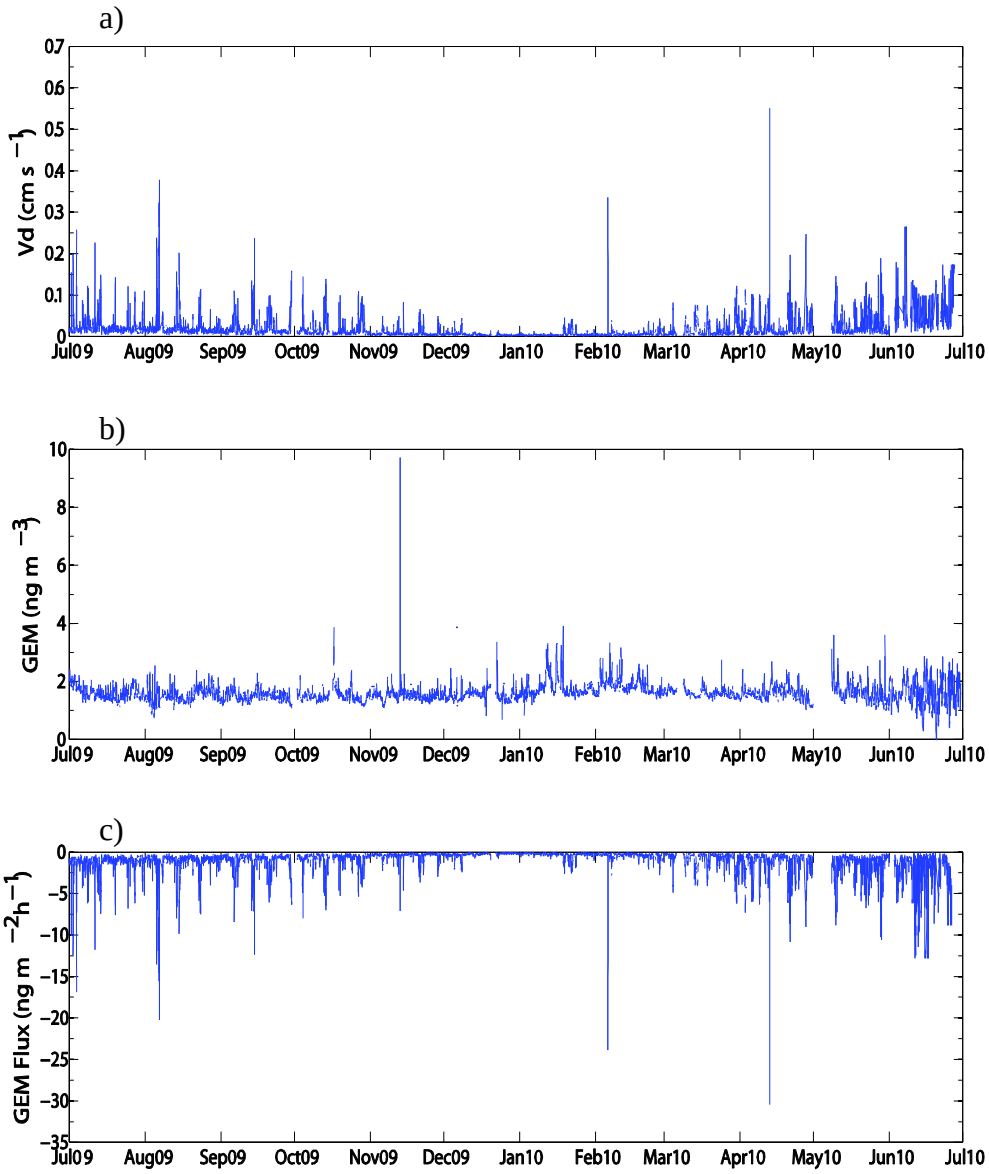

Figure 4.10. The product of the dry deposition velocity (a) and the measured GEM concentration (b) yields the flux of GEM into the GSL (c).

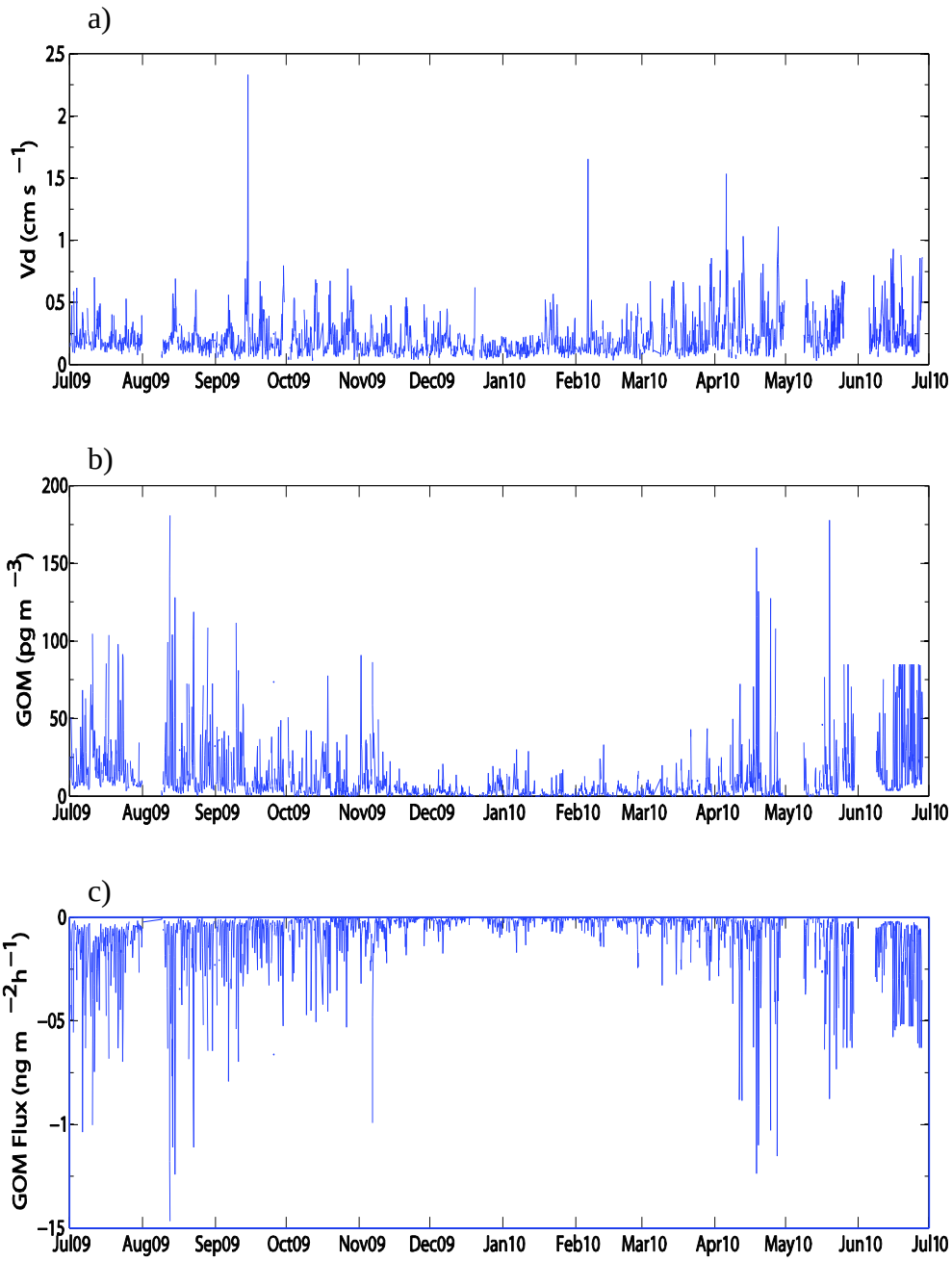

Figure 4.11. The product of the dry deposition velocity (a) and the measured GOM concentration (b) yields the flux of GOM into the GSL (c).

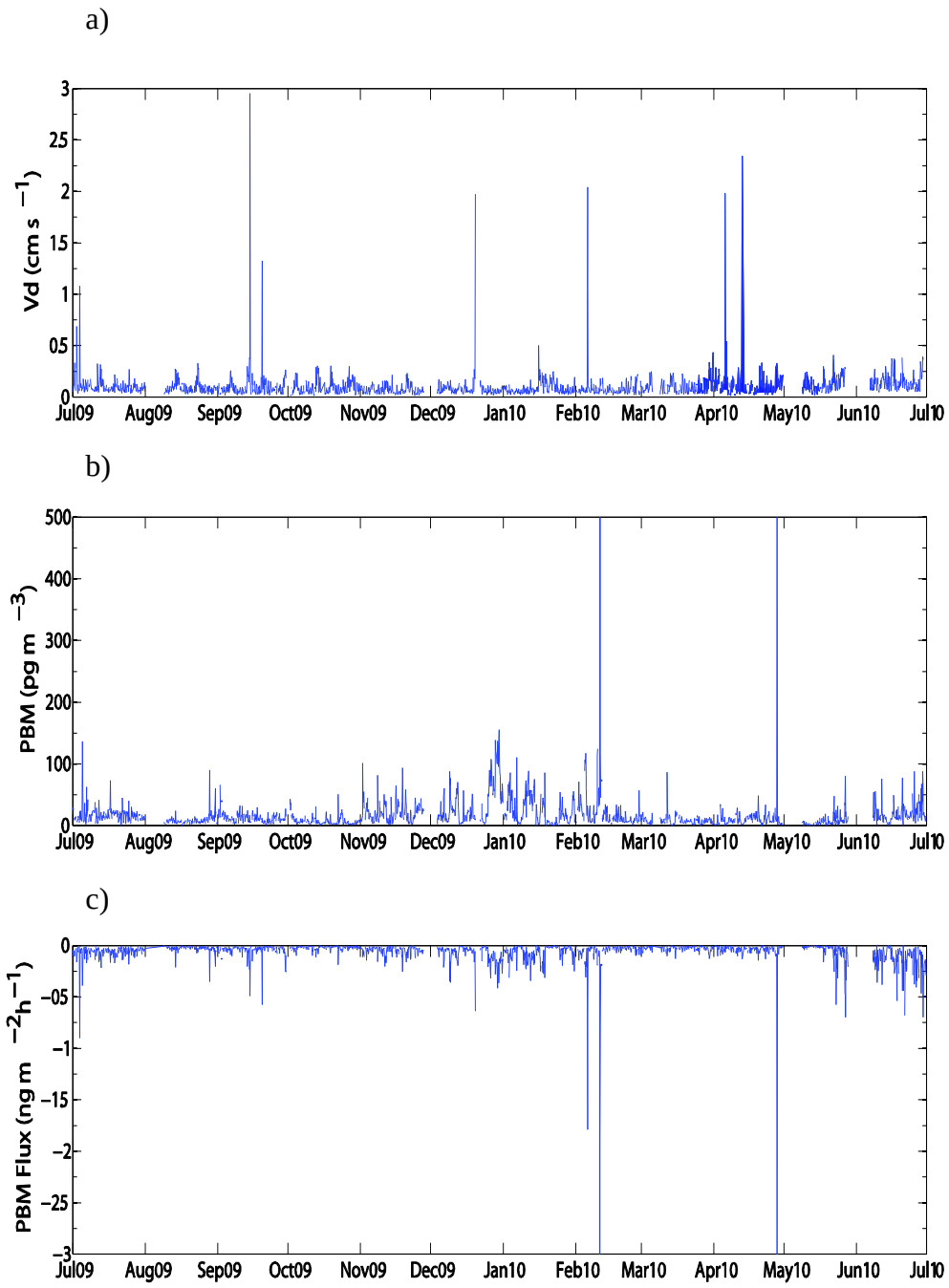

Figure 4.12. The product of the dry deposition velocity (a) and the measured PBM concentration (b) yields the flux of PBM into the GSL (c). Note: the PBM concentrations exceed the 500 pg m^{-3} scale on two occasions.

Table 4.1. Resistance-in-series model output for GEM for year of July 1, 2009 through June 30, 2010.

Month/ Year	R_a ($s\ m^{-1}$)	R_b ($s\ m^{-1}$)	R_c ($s\ m^{-1}$)	V_d ($cm\ s^{-1}$)	GEM ($ng\ m^{-3}$)	Total		Background		Background Removed	
						Avg. Flux ($ng\ m^{-2}\ h^{-1}$)	Total Flux ($ng\ m\ month^{-1}$)	Avg. Flux ($ng\ m^{-2}\ h^{-1}$)	Total Flux ($ng\ m^{-2}\ month^{-1}$)	Avg. Flux ($ng\ m^{-2}\ h^{-1}$)	Total Flux ($ng\ m^{-2}\ month^{-1}$)
Jul09	260	59.6	6071.2	2.50e-02	1.6	1.4	1043.7	1.3±0.2	981±130	.11±.1	84±100
Aug09	307.6	70.4	6785.4	2.70e-02	1.5	1.45	1076.4	1.3±0.2	981±130	.09±.1	69.3±83
Sep09	342.2	78.2	8431.9	2.10e-02	1.49	1.14	820.5	1.1±0.2	822±109	.04±.1	32.0±73
Oct09	300.9	72.4	10787.5	1.80e-02	1.5	0.91	680	1.0±0.2	708±95	.03±.1	19.4±51
Nov09	421.4	102.2	20112.6	8.80e-03	1.53	0.5	362.7	0.5±0.2	342±46	.03±.04	23.8±30
Dec09	406.9	95	34120.9	5.00e-03	1.55	0.3	224.2	0.3±0.2	202±27	.01±.03	10.5±18
Jan10	338.5	81.1	33019.7	5.20e-03	1.78	0.35	258.4	0.3±0.1	209±28	.04±.4	32.4±27
Feb10	348.7	81.7	26697.4	7.20e-03	1.84	0.48	325.6	0.4±0.1	256±35	.08±.5	55.6±34
Mar10	310.5	71.2	15666.7	1.60e-02	1.6	0.87	648.5	0.9±0.2	629±84	.04±.1	29.0±72
Apr10	284.3	81.5	9912.8	2.40e-02	1.6	1.36	978.8	1.3±0.2	941±125	.11±.1	76.0±94
May10	270	64.6	6478.9	2.80e-02	1.58	1.56	1158.9	1.5±0.2	1123±149	.14±.1	101±96
Jun10	229.5	57.4	5666.7	3.20e-02	1.54	1.74	1249.9	1.15±0.2	627.31±38	0.41±.1	93.38±96
Avg	317.7	76.1	15426.1	1.80e-02	1.59	1.01	735.63	0.9±0.2	582.5	.17±01	86.71
Total ($ng\ m^{-2}\ yr^{-1}$)							7513.7		7194±935		531±67

Table 4.2. Resistance-in-series model output for GOM for year of July 1, 2009 through June 30, 2010.

Month/ Year	R_a ($s\ m^{-1}$)	R_b ($s\ m^{-1}$)	R_c ($s\ m^{-1}$)	V_d ($cm\ s^{-1}$)	GOM ($pg\ m^{-3}$)	Avg. Flux ($ng\ m^{-2}\ h^{-1}$)	Total Flux ($ng\ m^{-2}\ month^{-1}$)
Jul09	142.0	47.3	340.5	0.22	21.7	1.6e-01	120.8
Aug09	178.0	56.6	366.3	0.21	25.2	1.7e-01	127.4
Sep09	228.8	64.2	346.4	0.24	14.1	1.1e-01	81.6
Oct09	234.9	68.1	339.1	0.23	7.9	8.0e-02	59.2
Nov09	266.2	78.0	425.8	0.17	7.4	6.8e-02	49.1
Dec09	236.1	71.6	535.3	0.16	3.1	4.6e-02	34.0
Jan10	224.6	66.8	465.2	0.17	2.6	4.1e-02	30.2
Feb10	233.3	71.4	403.2	0.19	3.1	5.0e-02	33.8
Mar10	187.2	57.9	311.8	0.26	4.8	5.7e-02	42.5
Apr10	174.5	59.2	274.1	0.32	12.9	1.2e-01	86.5
May10	176.3	56.6	262.4	0.28	11.1	1.1e-01	80.8
Jun10	173.3	55.5	279.8	0.27	22.9	1.90e-01	140.4
Avg	209.5	63.2	369.2	0.22	11.0	0.1	68.18
Yearly Total GOM Flux 745.9 $ng\ m^{-2}\ yr^{-1}$							

Table 4.3. Resistance-in-series model output for PBM for year of July 1, 2009 through June 30, 2010.

Month/ Year	R_a ($s\ m^{-1}$)	R_b ($s\ m^{-1}$)	V_s ($cm\ s^{-1}$)	V_d ($cm\ s^{-1}$)	PBM ($pg\ m^{-3}$)	Avg. Flux ($ng\ m^{-2}\ h^{-1}$)	Total Flux ($ng\ m^{-2}\ month^{-1}$)
Jul09	142.3	1139.9	3.5e-03	0.11	16.5	6.3e-02	47.1
Aug09	179.4	1361.7	3.5e-03	0.09	9.1	3.0e-02	22.2
Sep09	228.8	1532.7	3.5e-03	0.11	12.4	4.2e-02	29.9
Oct09	234.9	1583.5	3.6e-03	0.10	7.7	2.4e-02	18.1
Nov09	269.3	1805.4	3.6e-03	0.08	21.3	4.9e-02	35.2
Dec09	234.1	1599.9	3.7e-03	0.09	32.4	7.7e-02	57.2
Jan10	224.9	1503.5	3.7e-03	0.09	23.2	6.1e-02	45.2
Feb10	233.3	1620.9	3.6e-03	0.09	30.7	8.4e-02	56.6
Mar10	187.2	1339.9	3.6e-03	0.10	8.0	2.7e-02	20.0
Apr10	175.6	1396.2	3.6e-03	0.15	12.4	5.7e-02	40.8
May10	176.3	1335.4	3.6e-03	0.11	4.8	2.3e-02	17.1
Jun10	175.1	1336	3.50e-03	0.1	10.9	3.40e-02	24.5
Avg	206.3	1466.2	3.6e-03	0.102	16.4	4.8e-02	31.84
Yearly Total PBM Flux 389.4 $ng\ m^{-2}\ yr^{-1}$							

Note: The dry deposition flux of PBM with aerodynamic diameters > 2.5 µm was not measured as part of this project.

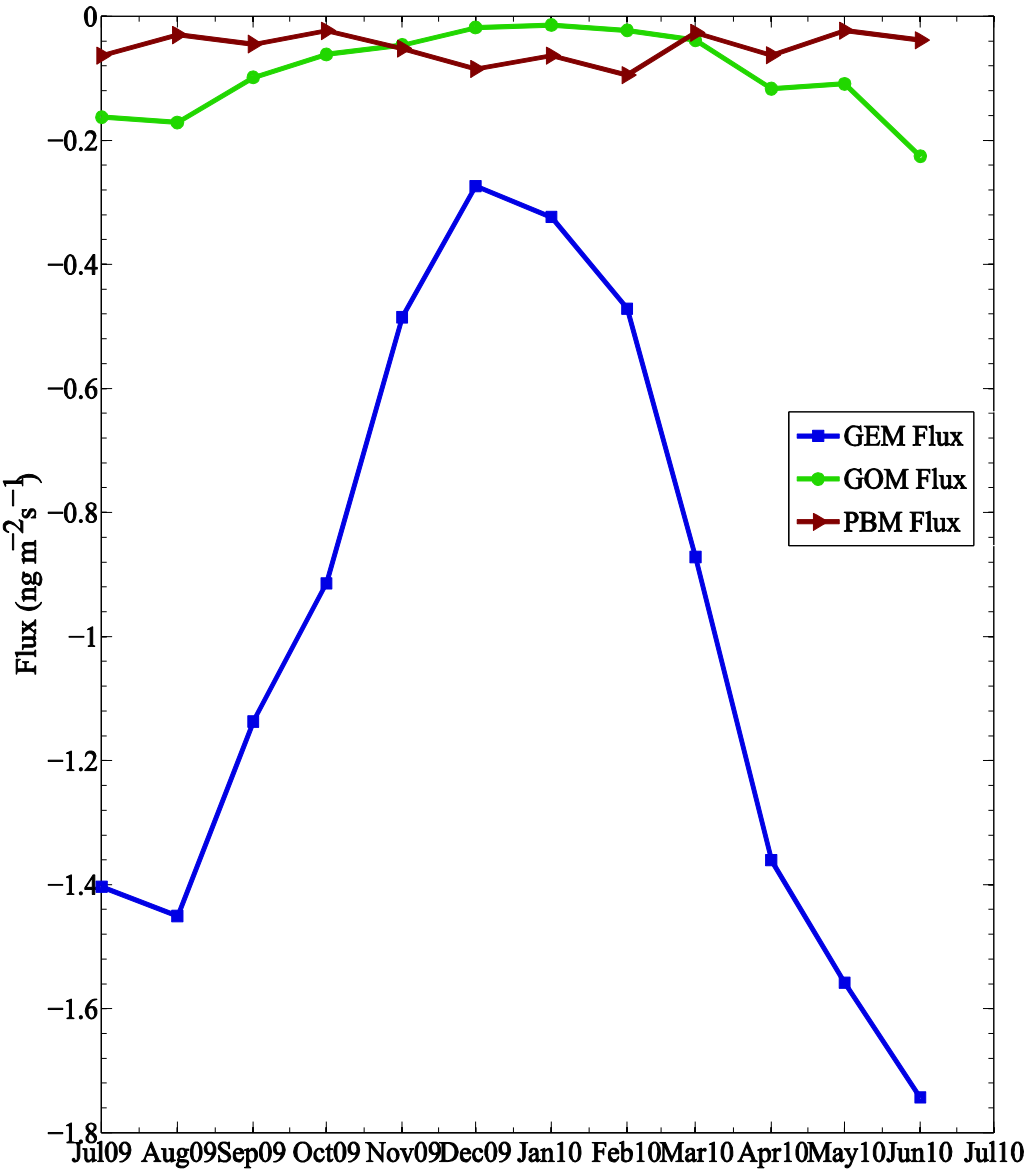

Figure 4.13. Monthly-averaged total mercury dry deposition flux from each Hg species.

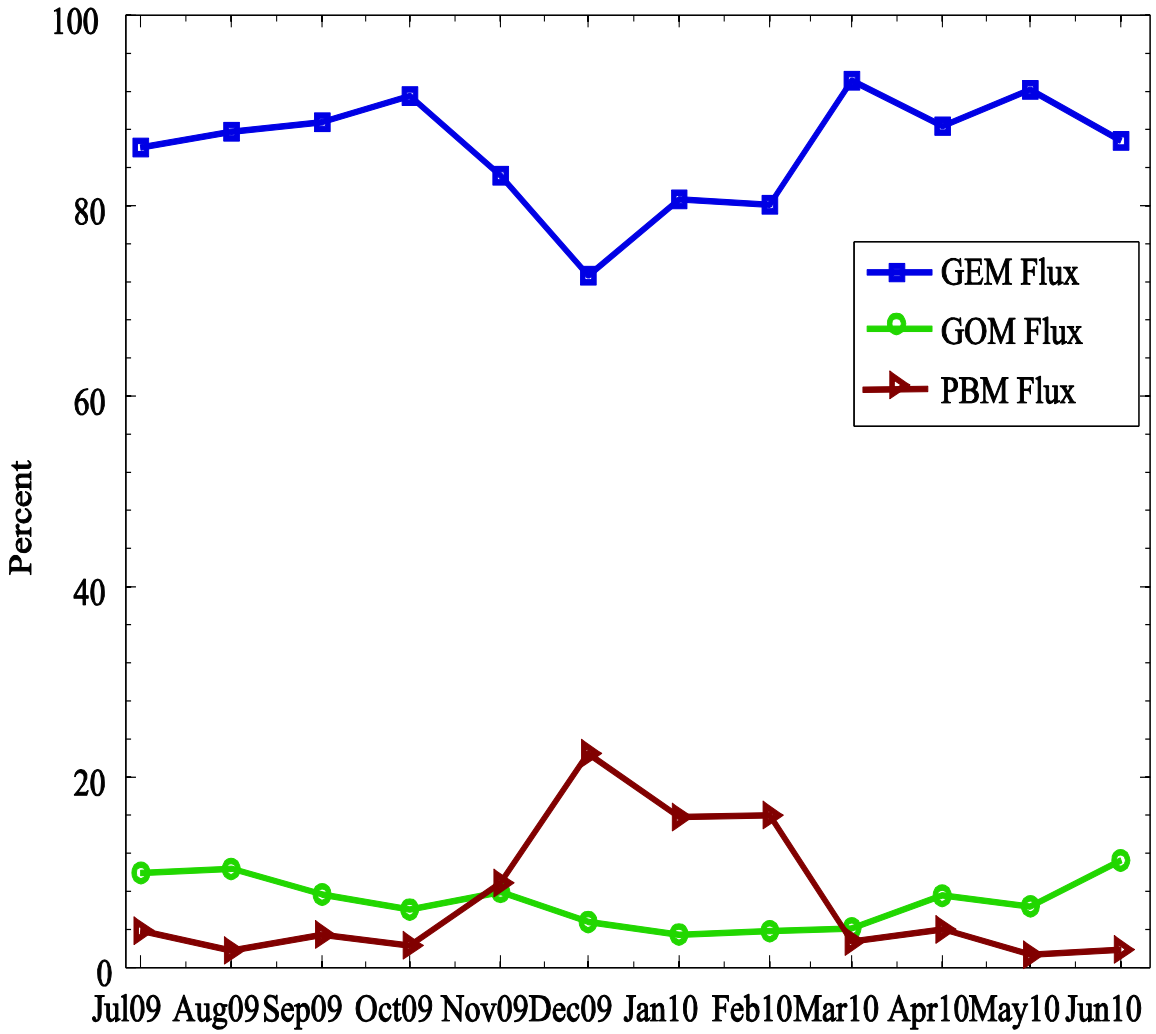

Figure 4.14. Percentage of the total mercury dry deposition flux contributed from each Hg species.

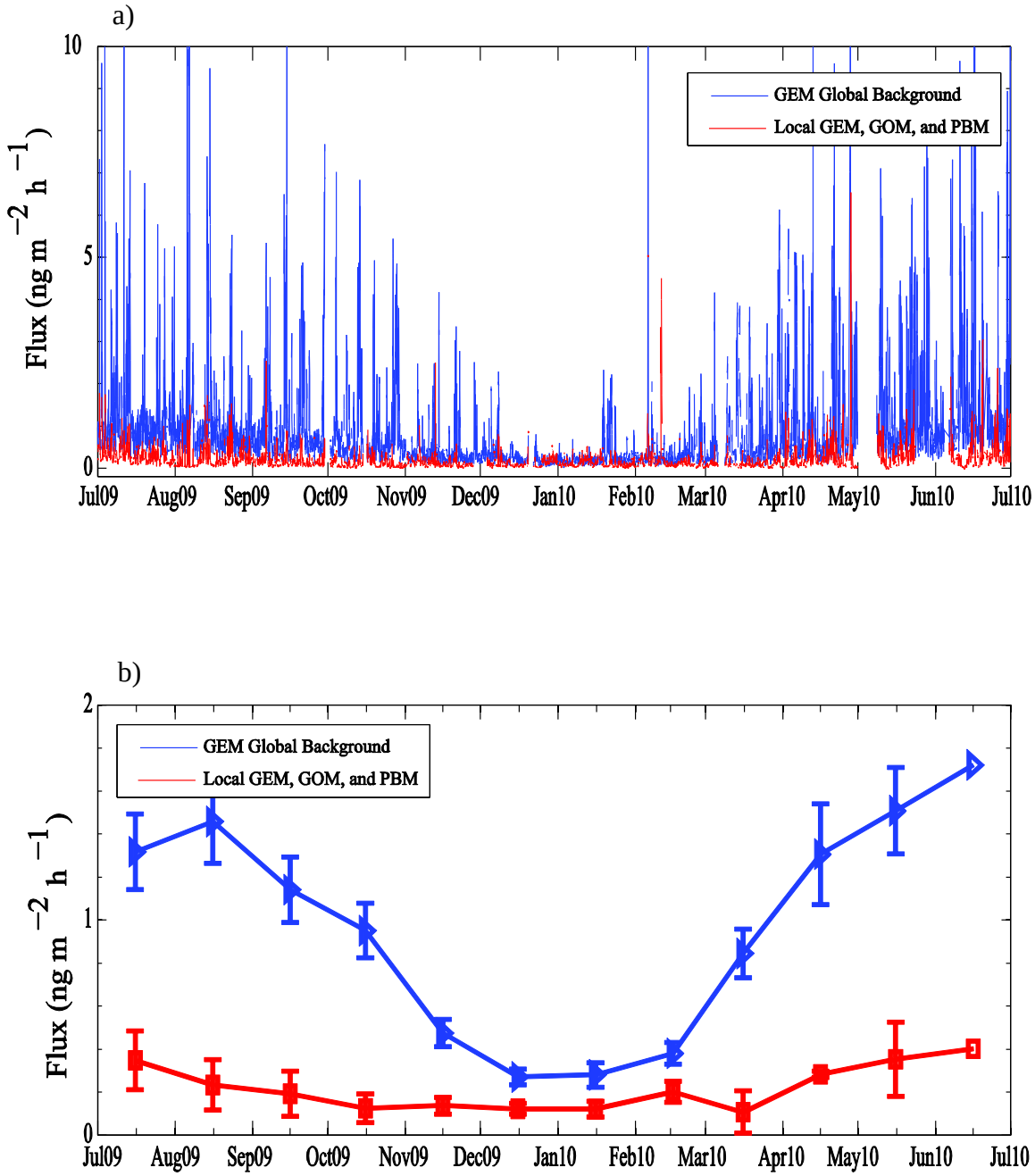

Figure 4.15. A time series of (a) the 2-hr-averaged and (b) monthly-averaged dry deposition fluxes from the GEM global background (1.5±0.2 ng m^{-3}) and the combined dry deposition fluxes of GEM from local/regional sources, GOM, and PBM.

4.3.1 Local/Regional GEM and Global Background

It has been shown that the flux of GEM is large compared to that of GOM and PBM (Figs. 4.12 and 4.13). The next question becomes: how much of that flux is from the global background GEM pool and how much can be attributed to local/regional sources? The dry deposition resistance-in-series model was run using a GEM concentration of 1.5±0.2 ng m^{-3} to represent the global background and then run again with the global background concentration subtracted from the measured concentrations to represent local/regional sources. [GEM depletion events were not considered in this experiment. The frequency, chemistry, and importance of GEM depletion events are a topic of current and future research (Skov et al. 2006 ; Lindberg et al. 2007; e.g., Peterson and Gustin 2008)]. Figure 4.15 is a comparison of the atmospheric dry deposition flux of the GEM global background and the composite flux of local/regional GEM, PBM, and GOM. The dry deposition flux from the global background is clearly larger, accounting for 83±8.5% of the total atmospheric dry deposition (Figs. 4.16, 4.17).

4.4 Model Sensitivity Analysis

There are a few select input parameters to the resistance-in-series model that are not well constrained and could add significant uncertainty to the model results. These are the particle aerodynamic diameter (D_p), particle density (ρ_p), the dynamic viscosity (μ), the diffusivity of GEM (D_{GEM}) and GOM (D_{GOM}) in the air, the Henry's law coefficient for GEM (*H*), and the aerodynamic roughness length (z_0). The model sensitivity to these

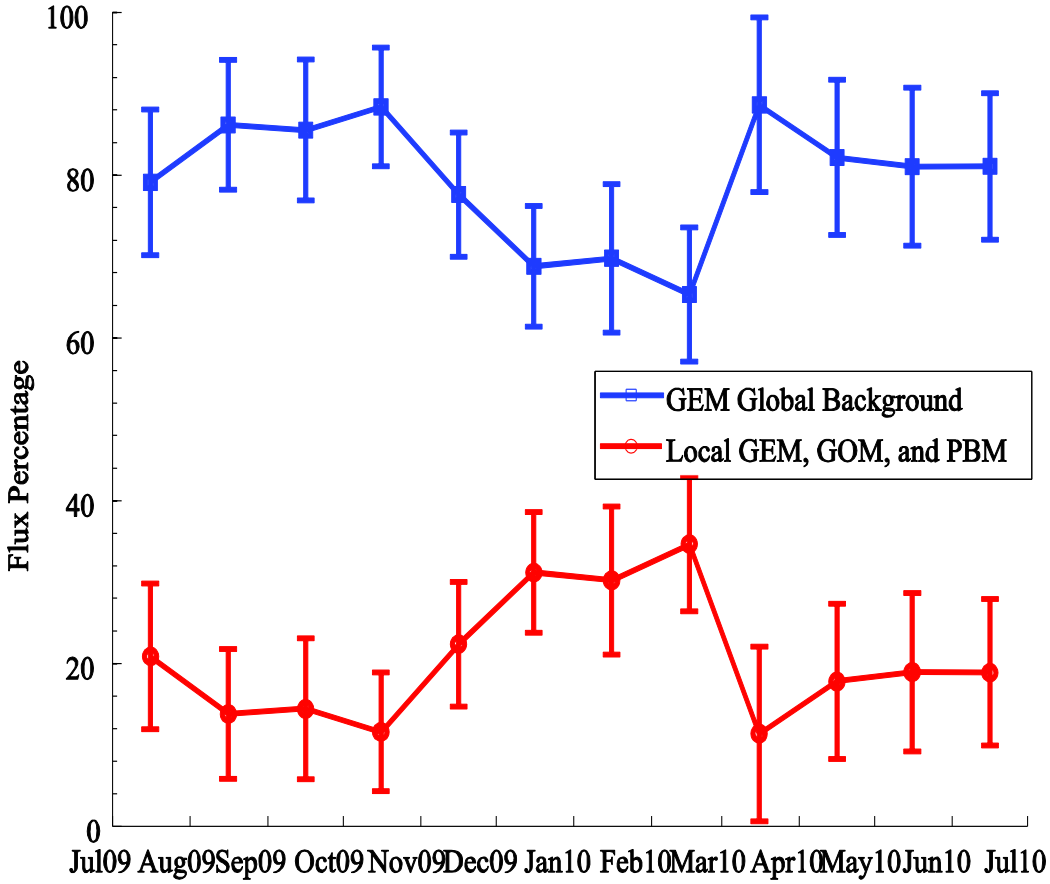

Figure 4.16. As in Figure 4.14b but now represented as a percentage of the monthly-averaged total atmospheric dry deposition.

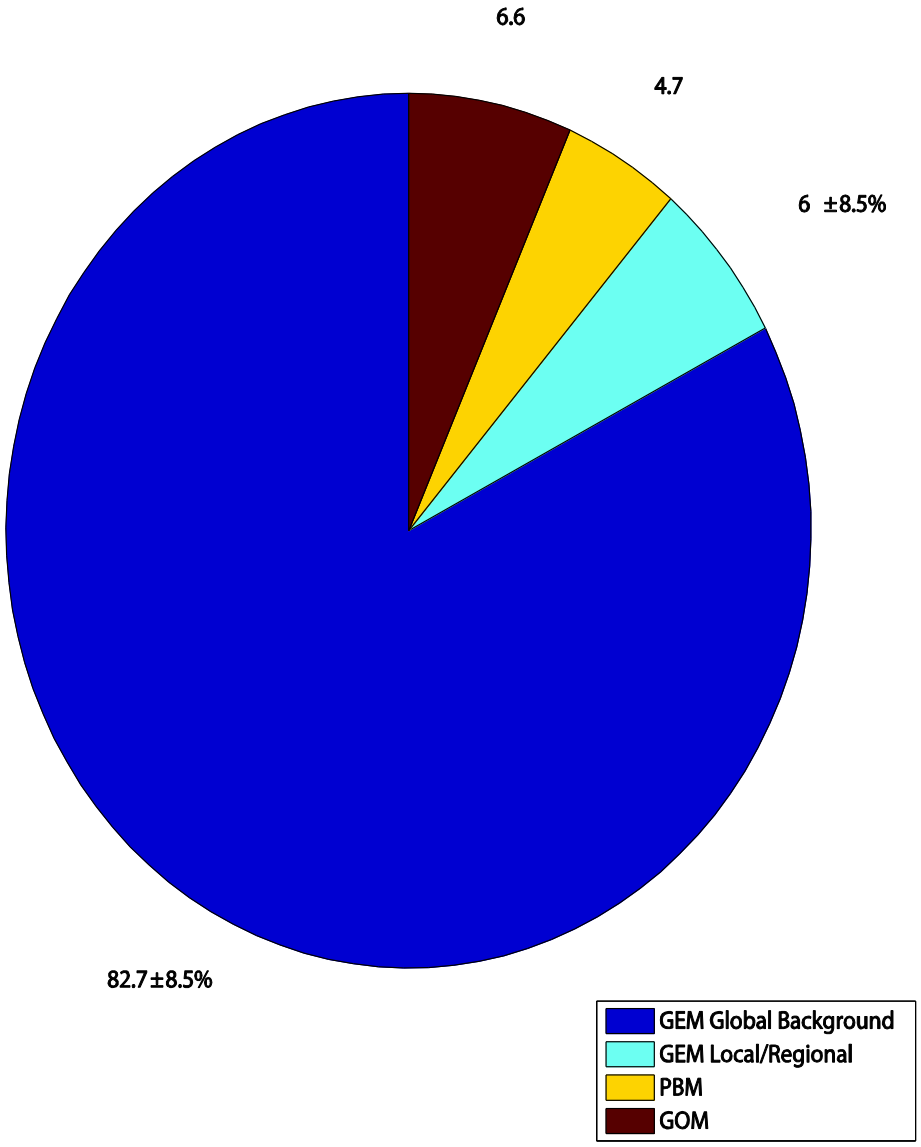

Figure 4.17. Atmospheric mercury dry deposition flux for July 1, 2009 through June 30, 2010 at the UT96 site.

input parameters was tested by first establishing a range and a "best guess" for each variable (Table 4.4). The model was run multiple times for each possible variation and combination using data from October 2009. This period was chosen for being a transition period between seasons and for being a period with relatively few interruptions to data collection. The average flux for the run consisting of the "best guess" values for each parameter was established as "truth" to use as a comparison to the other model runs. Then each variable was compared as the percentage change in flux to the change of the variable. The maximum change in the average flux was taken to be the percent of change in the model associated with that variable.

D_p for particulate mercury is the largest source of uncertainty in the PBM model results (Table 4.4) accounting for 272% uncertainty in PBM deposition model output. The upper bound of the particle diameter is given as 2.5 μm because that is the cutoff point of the Tekran© 1130 inlet valve. It is very likely that PBM particle diameters exceed this cutoff, but those larger particles must be removed by an inlet impactor to prevent spurious GOM measurements (Sections 2.2.2 and 2.2.3). The lower bound of the particle diameter was chosen to be 0.1 μm because particles with sizes much smaller than this are transient due to coagulation and are unlikely to dominate the paticulate mass. Also at ~0.07 μm, the assumption that the diameter of the particle is larger than the mean free path is no longer valid.

Uncertainty in the PBM density accounts for ~3% of the uncertainty in the model results. A best guess of 2 g cm^{-3} with a possible range of 1 to 3 g cm^{-3} was chosen based on intuition and experience. Figure 4.18 shows the percent change of the average flux as a function of both particle size and particle density.

Table 4.4. Results of model sensitivity test.

Input Parameter	Minimum Value	"Best Guess"	Maximum Value	% Change in Avg. GEM Flux	% Change in Avg. GOM Flux	% Change in Avg. PBM Flux
μ (Pa s)	1.72×10^{-5}	1.75×10^{-5}	1.78×10^{-5}	< 0.1%	<0.1%	3%
z_0 (m)	1×10^{-5}	9×10^{-5}	1×10^{-3}	16%	1%	4%
ρ_p (g cm^{-1})	1	2	3			2%
D_p (µm)	0.1	0.68	2.5			272%
D_{GEM} (cm^2 s^{-1})	0.10	0.12	0.14	< 0.1%		
D_{GOM} (cm^2 s^{-1})	0.07	0.09	0.10		0.4%	
H (dimensionless)	0.1	0.2912	0.5	65%		

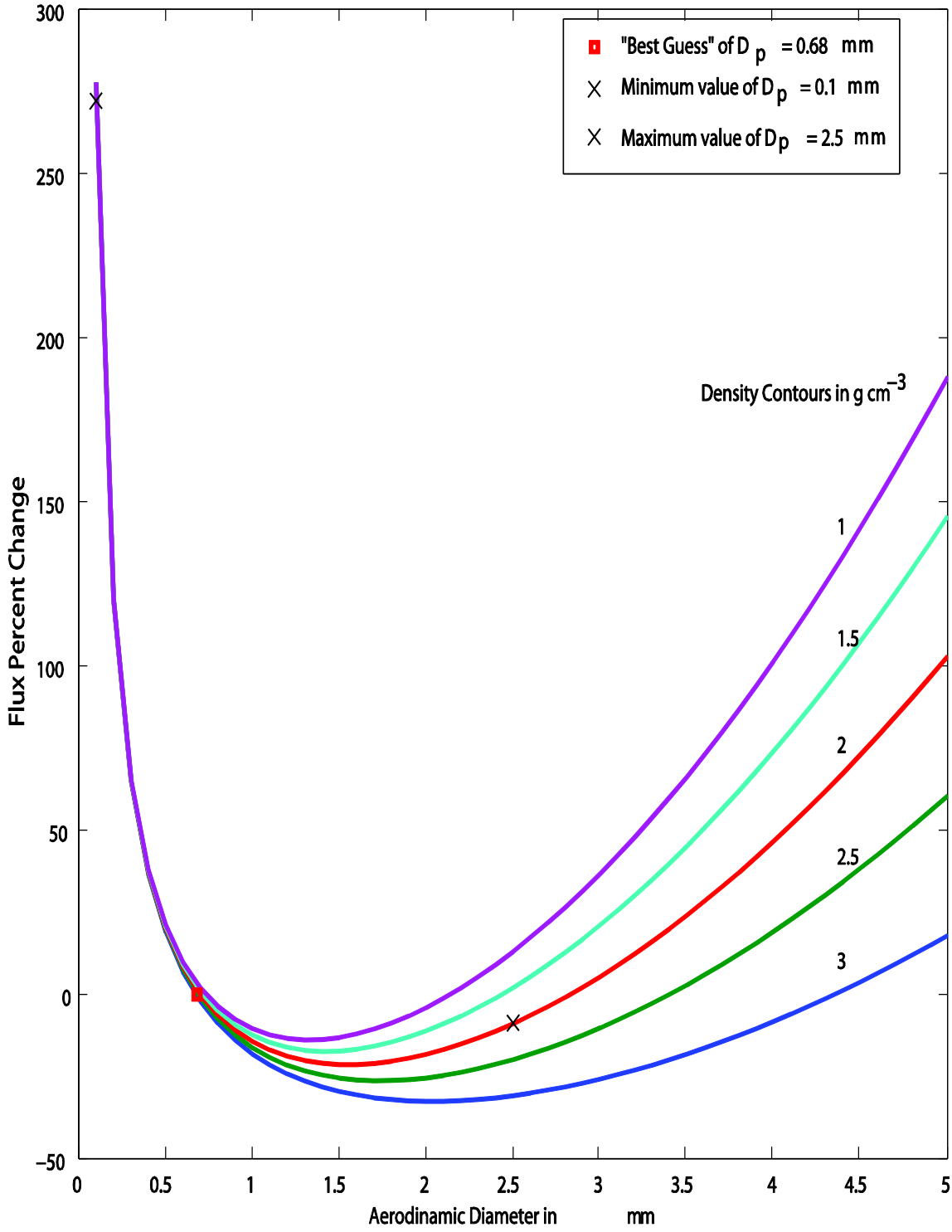

Figure 4.18. Contour plot of the change in average PBM flux compared with the changes in D_p *and* ρ_p as part of the model sensitivity analysis.

Another source of potential uncertainty in the model comes from the algorithm choice for μ. Literature suggests two possible equations for the calculation of μ as a function of air temperature. The first equation is known as Sutherland's formula (Eq. 3.17) and the other is:

$$\mu = 1.8 \times 10^{-5}\left({}^{T}/_{298}\right)^{0.85} \left(kg\ m^{-1}\ s^{-1}\right) \qquad (4.46)$$

where T is the temperature in K. The difference between the results of these two equations is only 0.002% for μ. This difference affects the model output by < 0.1% for GEM and GOM and 3% for PBM.

Input values of D_{GEM} and D_{GOM} (collectively D_{HG}) account for 0.4% and < 0.1% uncertainty for GOM and GEM fluxes, respectively. D_{GOM} is given as 0.09 $cm^2\ s^{-1}$ by Marsik et al. (2007), while D_{GEM} is given as 0.12 $cm^2\ s^{-1}$. A temperature correction for both diffusivities is given by Massman (1999) and is shown in Eq. 3.19. The sensitivity analysis for D_{Hg} tested the models sensitivity to temperature variations. The range for D_{Hg} was established using the maximum and minimum temperatures measured at the UT96 site. The "best guess" for D_{Hg} was determined for the mean temperature at the site in October (i.e., 9.5ºC). The model output showed minimal sensitivity to changes in D_{Hg}.

The dimensionless Henry's law coefficient (*H*) is essentially what governs the adsorption of GEM into the GSL. A larger *H* allows for more adsorption. *H* is determined by the aqueous concentration of Hg in the water divided by the partial pressure of the GEM in the atmosphere. *H* is known to be temperature dependent and has a slightly larger value for saltier water (Anderson et al. 2008). The range of values for *H*

was determined based on measurements of total Hg in water of the GSL taken by Naftz et al. (2008), the average of the GEM measurements taken as part of this study, and Eq. 3.31. The maximum value of *H* is 0.5 based on an aqueous concentration of 10 ng L^{-1}. A minimum value of *H* is 0.1 based on aqueous concentrations of 2 ng L^{-1}. A sensitivity analysis was run using this range and a "best guess" given by Eq. 3.38, which is a fit to observations given by Anderson et al. (2008). The average value of *H* given by Eq. 3.38 is 0.2912 and is unitless. *H* accounts for ~65% uncertainty in the GEM deposition model. Recall that the flux of GEM is about ten times larger than the flux of GOM or PBM. The final flux of total mercury will experience a much larger change due to the 65% of uncertainty associated with *H* than with the 272% associated with D_p for PBM. Therefore, the uncertainty associated with *H* is the largest source of uncertainty to the total flux.

Based on values given by Stull (1988, His Fig. 9.6), the aerodynamic roughness length (z_0) over relatively calm water could vary from 1×10^{-5} to 1×10^{-3}. A "best guess" was based on an adaptation to Charnock's relationship by Smith (1988):

$$z_0 = \frac{0.011 u_*^2}{g} + \frac{0.11 \upsilon}{u_*} \qquad (4.47)$$

The average value of the "best guess" used by this study is 9×10^{-5}. The resulting uncertainties in the modeled fluxes are 1%, 16%, and 4.5% for GEM, GOM, and PBM respectively.

From this model sensitivity analysis, it can be determined that uncertainty relating to *H* (65%) and z_o (16%) for GEM introduces the greatest error into the model because

the flux of GEM is large compared to the flux of GOM and PBM. This is followed by uncertainty about the PBM particle D_p (272%). All the other sources of uncertainty had a relatively small impact (< 5%) on model results.

4.5 Mercury Pathways into the Great Salt Lake

4.5.1 Dry Deposition

Because the GSL is a shallow (4.45m average depth, see Baskin 2005) terminal lake, the area of the GSL changes significantly with minor changes in lake depth. The height of the water has been measured over time by the USGS (Data available at http://waterdata.usgs.gov/ut/nwis/dv?referred_module=sw&site_no=10010000). Baskin (2005, 2006) studied the bathymetry of the GSL and produced tables for the lake's surface area and volume in relation to the height of the water surface as measured by the USGS. Using these measurements and Baskin's tables, the average surface area of the lake during the measurement period was determined to be 4603 km^2.

The total Hg flux for the year is calculated by multiplying the average hourly flux for each month by the number of hours in the month to get a monthly total (missing data was backfilled using the monthly average flux). Each monthly total was added to obtain the total flux for the whole year, and then converted from ng to µg (see Tables 4.11, 4.2, and 4.3) giving a total flux of 10.7 $\mu g\ m^{-2}\ yr^{-1}$. The product of the annual flux and the surface area of the lake yields the total yearly amount of mercury that has settled into the GSL by atmospheric dry deposition to be 49 kg .

4.5.2 Wet Deposition

The wet deposition of mercury has been measured at the Mercury Deposition Network site UT97, located in West Valley City, Salt Lake County, Utah, (40.7118 N, 111.9609 W) since May 2007. Site UT97 is 43.8 km southeast of UT96 and is the closest wet deposition monitoring location. Wet deposition data were used from UT97 with the most recent full year of data available from 2008. In 2008, 5.0 $\mu g\, m^{-2}$ of mercury was deposited by wet deposition at UT97 (Figure 4.19). As shown in Figure 4.20, this constitutes 29% of the total mercury influx into the Great Salt Lake.

4.5.3 Riverine Influx

A study by Naftz et al. (2009) measured riverine mercury inputs into the GSL using continuous stream flow gauges at six inflow sites and taking intermittent mercury measurements during a 1-year period. Naftz et al. (2009) found that the cumulative total mercury riverine input to the GSL during the year April 1, 2007 to March 31, 2008 was 6 kg or about 1.9 $\mu g\, m^{-2}$, which amounts to only 11.5% of the total flux into the lake (Fig. 4.20).

4.6 Summary

Dry deposition of mercury into the GSL is the most significant pathway of mercury into the lake, accounting for 60% of all the mercury in the lake. Wet deposition accounts for 29% and riverine influx accounts for only 11%. The measurements of mercury from wet deposition, riverine influx, and the output from this dry deposition resistance-in-series model collectively account for a flux of about 17.6 $\mu g\, m^{-2}\, yr^{-1}$ of mercury. Multiplying by the average surface area of the lake during the measurement

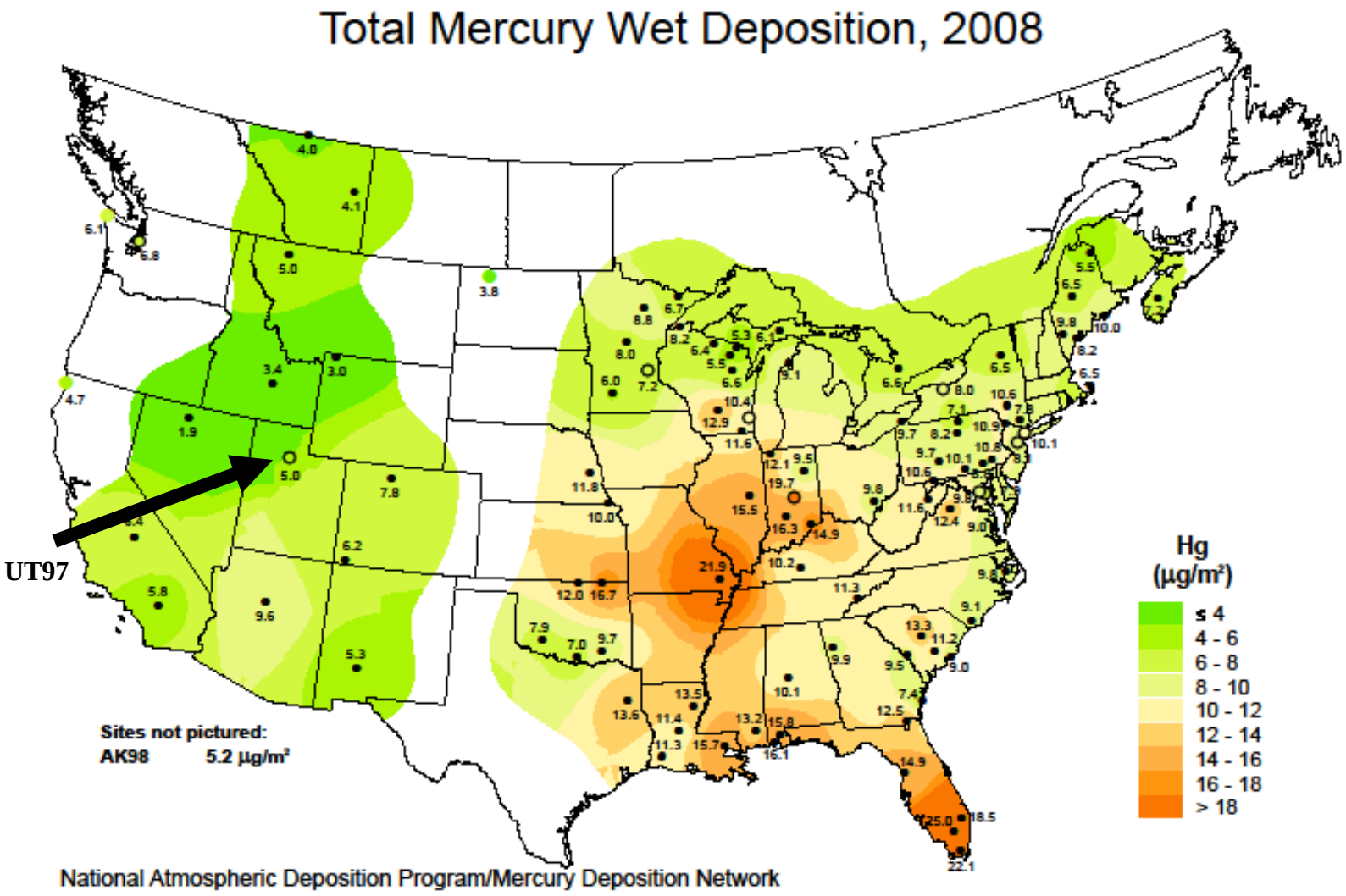

Figure 4.19. Wet deposition of mercury in µg m^{-2} (National Atmospheric Deposition Program)

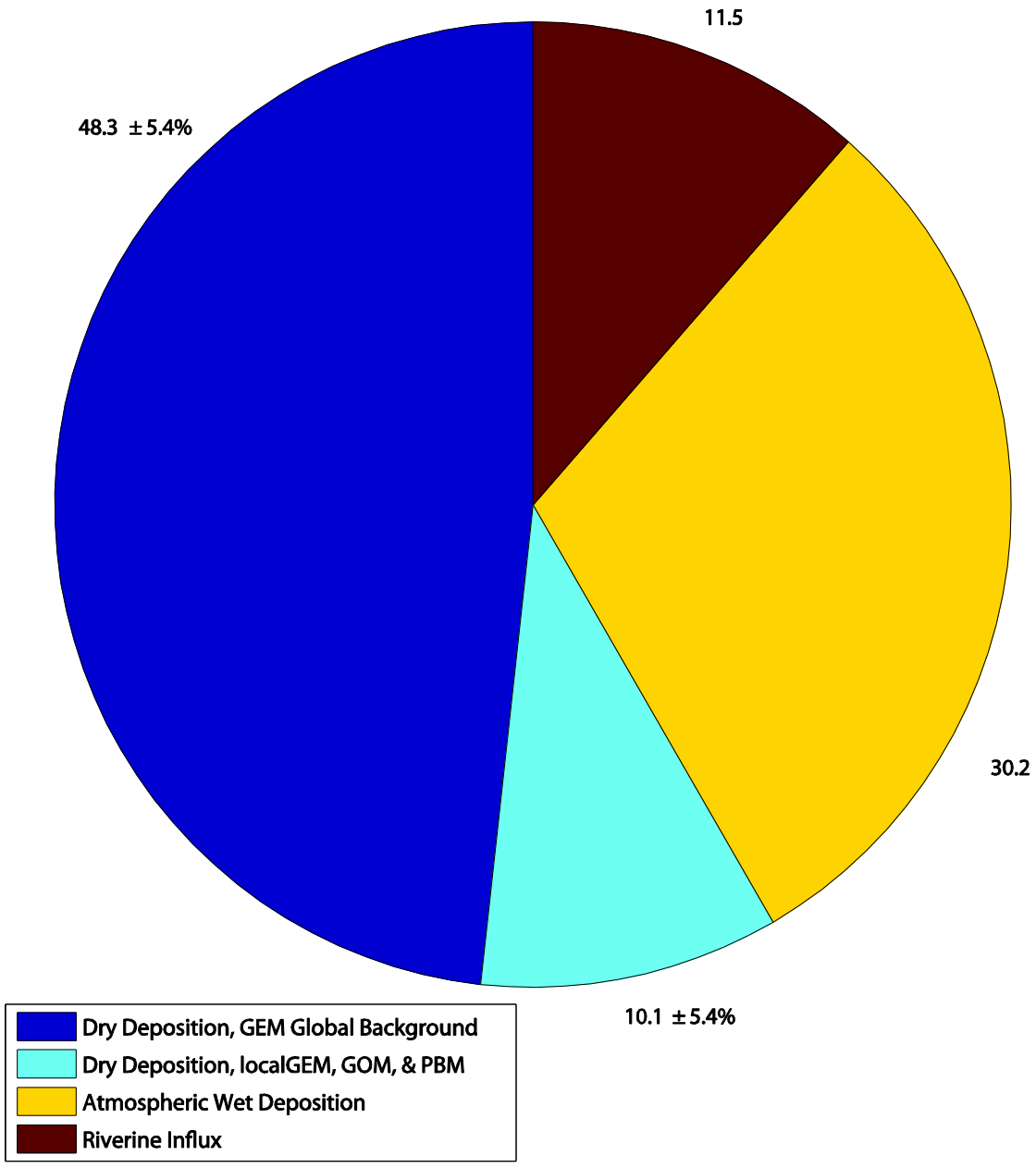

Figure 4.20. Total mercury flux into the GSL.

period would suggest about 81 kg of mercury that has deposited into the lake during the measurement period.

It should be noted that of Hg pathways into the GSL being compared in this section, dry deposition of coarse PBM was not measured as. Therefore, the percentages of Hg influx presented in this section may not be a complete representation of the total Hg entering the GSL. The possible significance of coarse PBM and its contribution to the total flux of Hg into the GSL will be discussed in more detail in Sections 5.1 and 5.2.

CHAPTER 5

CONCLUSIONS

Mercury pollution in the lakes and rivers of the western United States is rapidly becoming an issue in water bodies that have historically been considered rural, isolated, and pristine. Once the Hg enters the ecosystem, it can be transformed into MeHg which is considered toxic and can bioaccumulate up the food chain. This contamination problem is rendering many species of game fish and waterfowl unsuitable for human consumption. The GSL has been identified as one of the most mercury laden-bodies of water within the U.S. with mercury concentrations ranging from 7 to > 100 ng L^{-1} (Naftz et. al 2008) and posing a great risk to the wildlife and industries that use the lake.

The motivation for this research is to aid in identifying and eliminating the sources of Hg to the GSL, and provide insight to the growing number of Hg-related fish advisories being issued for lakes, rivers, and streams in the western United States. The specific goal of this study is to quantify and better understand the dry deposition of Hg into the GSL and then to identify the primary influx pathways of Hg into the GSL. Speciated atmospheric Hg concentrations along with turbulence measurements were collected at a field site, UT96, on the eastern shore of the GSL from July 1, 2009 through June 30, 2010. A resistance-in-series dry deposition model (Wesely and Hicks 1977) was

built for conditions specific to the GSL. The calculated deposition velocities were multiplied by the measured Hg concentrations to produce a dry deposition flux. This flux was compared with wet deposition measurements taken from the National Mercury Deposition Network wet deposition monitoring site (UT97) in West Valley City, Utah, and with Hg measurements from rivers and streams that flow into the lake taken by the USGS.

It was found that the dry deposition flux of atmospheric Hg into the GSL was composed of 82±8.5% of GEM from what is considered the global background; < 6±8.5% of GEM that may be considered local/regional, 7% from GOM, and 4% from PBM on fine particles (Fig. 4.16). (This study did not measure the concentrations of coarse PBM). These collectively make up the dry deposition flux and account for the deposition of 10.7 $\mu g\, m^2\, yr^{-1}$ of Hg into the GSL and make up 60% of the total flux of Hg into the GSL. Wet deposition accounts for 5.0 $\mu g\, m^2\, yr^{-1}$ and makes up 29% of the total flux of Hg into the GSL (National Atmospheric Deposition Program). The riverine input as measured by the USGS accounts for about 1.9 $\mu g\, m^2\, yr^{-1}$ (Naftz et. al 2009) and makes up 11% of the total flux of Hg (Fig. 4.18).

5.1 Comparison with Observations

Traditionally, one of the weaknesses to the dry deposition resistance in-series model has been a lack of observations to compare results with. Fortunately, for the GSL, there have been Hg analysis of sediment cores within the GSL and these can be used as a comparison of total Hg sedimentation within the lake. The sediment cores suggest the

mean annual total Hg input range from 55 $\mu g\, m^2\, yr^{-1}$ to 150 $\mu g\, m^2\, yr^{-1}$, with an average over the last 100 years of 130 $\mu g\, m^2\, yr^{-1}$ (Naftz et al. 2009).

Using the wet deposition flux of 5.0 $\mu g\, m^2\, yr^{-1}$, the riverine influx of 1.9 $\mu g\, m^2\, yr^{-1}$, and the modeled dry deposition flux from this study of 10.7 $\mu g\, m^2\, yr^{-1}$, the cumulative influx of mercury into the GSL is 17.6 $\mu g\, m^2\, yr^{-1}$, or only about 13% of what the sedimentation record shows.

There may be several reasons for the discrepancy between the Hg influx into the GSL and the Hg measured in the sediment cores. Naftz et al. (2009) suggest that some disagreement may enter due to sediment focusing (i.e., the sediments do not settle uniformly across the lake bottom and some measurements may yield higher concentrations of Hg than others). Other sources of discrepancy may be from the lack of measurement of PBM on larger particles (> 2.5 μm) and the potential conversion of GEM to GOM within the marine boundary layer immediately above the lake. The latter two possibilities will be discussed in more detail in Section 5.2.

5.2 Model Strengths and Weaknesses

This dry-deposition model is the first resistance-in-series model built specifically for the conditions of the GSL. There are several attributes that this model includes that makes it more adequate than general dry-deposition models for this application. Some of these attributes are site-specific and continuous Hg and turbulence measurements, correct lake water temperature (Crosman and Horel 2009), viscosity of Hg in salt water coefficient that was adapted to the salinity of the GSL (Isdale et al. 1971), and a Henry's law coefficient specific to GEM and very salty water (Anderson et al. 2008).

The modeled Hg dry-deposition flux is most likely an underestimate of the true dry-deposition flux of Hg into the GSL. This underestimation comes about from several sources within the model, including a lack of measurement of PBM on coarse particles and the conversion of GEM to GOM within the marine boundary layer immediately above the lake.

A study by Keeler et al. (1995) found that the size distribution of PBM in urban Detriot, MI, was bimodal with an average size of fine particles of 0.68 μm and the average size of the large particles was 3.78 μm. Keeler at al. (1995) further showed that in urban and industrialized locations, PBM on large particles (> 2.5 μm) occasionally would reach concentrations near 1 ng m^{-3} and demonstrated a flux that was 4-5 times greater than the fine particles. The Tekran© Model 1130 filters out any particles > 2.5 μm in order to prevent particle buildup on the inside surface of the denuder. The percentage of PBM that is removed could be (and probably is) significant, especially considering PBM has a large V_d, and the frequency of large dust storms experienced in the region.

When using a two-film model to calculate R_c for the dry deposition of gases to a water surface, the assumption is made that the gas does not undergo any chemical change within this constant flux layer. However, it has been suggested that due to the presence of halogens (e.g., Cl, Br, I) in the marine boundary layer above the GSL, GEM will be readily oxidized to GOM, thus significantly increasing the V_d (Schroder and Munthe 1998; Lindberg et. al 2001, 2002; Sprovieri et al. 2003; Peterson and Gustin 2008). It is very likely that some GEM we are measuring atop a 4 m tower could have been

converted to GOM before reaching the water surface. This oxidation might add a significant portion to the Hg flux that is currently not being considered.

While monitoring ambient Hg at site UT96 on the eastern shore of the GSL, occasionally a spike, or event, of anomalously high Hg concentrations would be detected. A local source of these spikes could be identified using HYSPLIT air mass trajectories. Some of these events were isolated or sporadic like fireworks on Independence Day, for example. However, it is possible that some of what was measured as an "event" was actually a continuously emitting local source of Hg which could only be detected when the wind conditions were favorable in ushering the plume over the measurement site. If this is the case, the mean and median Hg concentrations used could have been higher than what was actually measured.

5.3 Future Work

The model weaknesses discussed in Section 5.2 provide opportunities for future research which could add to the accuracy of the dry deposition model presented in this thesis.

Perhaps the area of greatest uncertainty, and therefore the greatest need for further research, is information regarding coarse PBM particles. It has been shown that the size distribution of PBM varies widely between sites, especially between rural and urban sites (Keeler et al. 1995). Future work could include a site-specific size and density distribution of PBM. This would determine if there was an actual need for PBM measurements of coarse particles. The resistance-in-series dry deposition model is very sensitive to particle size. Knowledge about the size distribution would significantly reduce any model uncertainty associated with particle size and density.

Another area of future research would be investigating the most prevalent chemical composition of GOM. This would then lead to specific and accurate Henry's law coefficients and diffusive properties, thus leading to more accurate V_d.

A study of the potential oxidation of GEM to GOM within the atmospheric surface layer above the GSL and at the air-water interface will give more, and much needed information about the amount of GEM that deposits into the lake. In the current model, it is assumed that all GEM remains as GEM throughout the entire deposition process. This assumption is made because no other information is available about GEM conversion. However, should it be determined that this assumption is invalid, revisions to the model should be made to account for the chemical transformation.

Results of this study and the resistance-in-series dry deposition model presented in this thesis suggest that about **17.0±8.5%** of the dry deposition of Hg into the GSL may be coming from local or regional sources (considering GOM as a local/regional source and not a secondary pollutant). Further source apportionment studies should be conducted to identify such sources and could potentially be used to combat the serious and ever-growing problem associated with Hg deposition into the GSL. The areas of further research mentioned herein will also help to fill in missing knowledge gaps and alleviate some of the uncertainty associated with this dry deposition model.

REFERENCES

Andersson, M.E., K. Gardfeldt, I. Wangberg, and D. Stromberg, 2008: Determination of Henry's law constant for elemental mercury. *Chemosphere*, **73,** 587-592.

Banic, C. M., S. T. Beauchamp, R. J. Tordon, W. H. Schroeder, A. Steffen, K. A. Anlauf, and H. K. T. Wong, 2003: Vertical distribution of gaseous elemental mercury in canada. *Journal of Geophysical Research*, **108**, NO. D9, 4264, doi:10.1029/2002JD002116.

Baskin, R.L. 2005: Calculation of area and volume for the south part of the Great Salt Lake, Utah. *U.S. Geological survey Open-File Report* 2005-1327: 6 p.

Baskin, R.L. 2006: Calculation of area and volume for the north part of the Great Salt Lake, Utah. *U.S. Geological survey Open-File Report* 2006-1359: 6 p.

Biswas, A., Blum, J.D., Klaue, B., and G.J. Keeler, 2007: Release of mercury from Rocky Mountain forest fires. *Global Biogeochemical Cycles,* **21**, GB1002, doi:10.1029/2006GB002696.

Bretherton, C., cited 2010: Lecture 6. Monin-Obuhkov similarity theory. [http://www.atmos.washington.edu/2004Q2/547/www/lect6.pdf.].

Brosset, C., 1986: The behavior of mercury in the physical environment. *Water, Air, Soil Pollution*, **34**, 145-166.

Brutsaert, W., 1975: The roughness length of water vapor, sensible heat, and other scalars. *J. Atmos. Sci.* **32**, 2028-2031.

Brutsaert, W., 1979: Heat and mass transfer to and from surfaces with dense vegetation or similar permeable roughness. *Boundary Layer Meteorology*, **16**, 365-288.

Businger, J.A., J.C. Wyngaard, Y. Icumi, and E.F. Bradley, 1971: Flux-profile relationship in the atmospheric surface layer. *J. Atmos. Sci.* **28**, 181-189.

Carpi, A., 1997: Mercury from combustion sources: A review of the chemical species emitted and their transport in the atmosphere. *Water, Air, and Soil Pollution,* **98**, 241-257.

Converse, A.D., A.L. Riscassi, and T.M. Scanlon, 2010: Seasonal variability in gaseous mercury fluxes measured in a high-elevation meadow. *Atmos. Environ.,* **44** 2176-2185.

Crane Company, 1988: Flow of fluids through valves, fittings, and pipe. *Technical Paper No. 410 (TP 410))*.

Crosman, E.T., and J.D. Horel, 2009: MODIS-derived surface temperature of the great salt lake. *Remote Sensing of Environment*, **113,** 73-81.

Deacon, E.L., 1977: Gas transfer to and across an air-water interface. *Tellus,* **29**, 363-374.

Driscoll, C.T., Han, Y., Chen, C.Y., Evers, D.C., Lambert, K.F., Holsen, T.M., Kamman, N.C., and R.K. Munson, 2007: Mercury contamination in forest and freshwater ecosystems in the northeastern United States. *Bioscience*, **57**, 17-28.

Friedli, H.R., Radke, L.F., and J.Y. Lu, 2001: Mercury in smoke from biomass fires. *Geophysical Research Letters,* **28**, 3223-3226.

Friedli, H.R., Radke, L.F., Prescott, R., Hobbs, P.V., and P. Sinha, 2003: Mercury emissions from the August 2001 wildfires in Washington State and an agricultural waste fire in Oregon and atmospheric mercury budget estimates. *Global Biogeochemical Cycles*, **17(2)**, 1039, doi:10.1029/2002GB001972.

Garratt. J.R., and B.B. Hicks, 1973: Momentum, heat and water vapour transfer to and from natural and artificial surfaces. *Quarterly Journal of the Royal Meteorological Society,* **99**, 680-687.

Gbor, P. K., D. Wen, Fan Meng, Fuquan Yang, and James J. Sloan, 2006: Modeling of mercury emission, transport and deposition in North America. *Atmos. Environ.*, **41**, 1135-1149.

Giorgi, F., 1986: A particle dry-deposition scheme for use in tracer transport models. *Journal of Geophysical Research*, **91**, 9794-9806.

Giorgi, F., 1988: Dry deposition velocities of atmospheric aerosols as inferred by applying a particle dry deposition parameterization to a general circulation model, *Tellus,* **40B**, 23-41.

Gustin, M.S., H. Biester, and C.S. Kim, 2002: Investigation of the light-enhanced emission of mercury from naturally enriched substrates. *Atmos. Environ.*, **36**, 3241-3254.

Gustin, M.S., 2003: Are mercury emissions from geologic sources significant? A status report. *Science of the Total Environment*, **304**, 153-167.

Hedgecock, I.M., and N. Pirrone, 2004: Chasing quicksilver: Modeling the atmosphereic lifetime of $Hg^0_{(g)}$ in the marine boundary layer at various latitudes. *Environmental Science and Technology*, **38**, 69-76.

Hicks, B.B., and P.S. Liss, 1976: Transfer of SO_2 and other reactive gases across the air-sea interface. *Tellus*, **28**, 348-354.

Hicks, B.B., D.D. Baldocchi, T.P. Meyers, R.P. Hosker Jr., and D.R. Matt, 1987: A preliminary multiple resistance routine for deriving dry deposition velocities from measured quantities. *Water, Air, and Soil Pollution*, **36**, 311-330.

Hicks, B.B., and Coauthors, 1989: A field investigation of sulfate fluxes to a deciduous forest. *Journal of Geophysical Research*, **94**, 13003-13011.

Hobbs, P.V., 2000: *Introduction to Atmospheric Chemistry*. Cambridge University Press, 262 pp.

Horvat, M., 2005: Determination of mercury and its compounds in water, sediment, soil, and biological samples. *Dynamics of Mercury Pollution on Regional and Global Scales*. Nicola Pirrone and Katheryn R. Mahaffey, Eds., Springer, 153-183.

Isdale, J.D., C.M. Spence, and J.S. Tudhope, 1971: Physical properties of sea water solutions: Viscosity. *Desalinization*, **10**, 319-328.

Jaffe, D. and Coauthors, 1999: Transport of Asian air pollution to North America. *Geophysical Research Letters*, **Vol.26, No.6**. 711-714.

Jaffe, D., I. McKendry, T. Anderson, and H. Price, 2003: Six 'new' episodes of trans-pacific transport of air pollutants. *Atmos. Environ.*, **37**, 391-404.

Jaffe, D., E. Prestbo, P. Swartzendruber, P. Weiss-Penzias, S. Kato, A. Takami, S. Hatakeyema, and Y. Kajii, 2005: Export of atmospheric mercury from asia. *Atmos. Environ.*, **39**, 3029-3038.

Keeler, G., G. Glinsorn, and N. Pirrone, 1995: Particulate mercury in the atmosphere: Its significance, transport, transformation and sources. *Water, Air, and Soil Pollution*, **80**, 159-168.

Krishnan, S. V., B. K. Gullett, and W. Jozewicz, 1994: Sorption of elemental mercury by activated carbons. *Environmental Science and Technology*, **28**, 1506-1512.

Kuss, J., J. Holzmann, and R. Ludwig, 2009: An elemental diffusion coefficient for natural waters determined by molecular dynamics simulation. *Environmental Science and Technology,* **43**, 3183-3186.

Landis, M. S., R. K. Stevens, F. Schaedlich, and E. Prestbo, 2002: Development and characterization of an annular denuder methodology for the measurement of divalent inorganic reactive gaseous mercury in ambient air. *Environ. Sci. Tech.*, **36**, 3000-3009.

Landis, M. S., M. M. Lynam, and R. K. Stevens, 2005: The monitoring and modeling of mercury species in support of local, regional and global modeling. *Dynamics of Mercury Pollution on Regional and Global Scales*. Nicola Pirrone and Katheryn R. Mahaffey, Eds., Springer, 123-151.

Langford, N.J., and R.E. Ferner, 1999: Toxicity of mercury. *Journal of Human Hypertension,* **13**, 651-656.

Lin, C.J., P. Pongprueksa, S. Lindberg, S. Pehkonen, D. Byun, and C. Jang, 2006: Scientific uncertainties in atmospheric mercury models I: Model science evaluation. *Atmos. Environ.*, **40**, 2911-2928.

Lindberg, S. E., S. Brooks, C.J. Lin, K.J. Scott, T. Meyers, L. Chambers, M. Landis, and R. Stevens, 2001: Formation of reactive gaseous mercury in the arctic: Evidence of oxidation of Hg^0 to gas-phase Hg-II compounds after arctic sunrise. *Water, Air, and Soil Pollution: Focus*, **1**, 295-302.

Lindberg, S. E., S. Brooks, C.J. Lin, K.J. Scott, M.S. Landis, R.K. Stevens, M. Goodsite, and A. Richter, 2002: Dynamic oxidations of gaseous mercury in the arctic troposphere at polar sunrise. *Environ. Sci. Technol.*, **36**, 1245-1256.

Lindberg, S., and Coauthors, 2007: A synthesis of progress and uncertainties attributing the source of mercury in deposition. *Ambio*, **36**, 19-32.

Liss, P.S., and L. Merlivat, 1986: Air-sea gas exchange rates: Introduction and synthesis. *The Role of Air-Sea Exchange in Geochemical Cycling*, P. Buat-Menard, Ed., D. Reidel Publishing Company, pp. 113-127.

Liu, B.Y.H., and J.K. Agarwal, 1974: Experimental observation of aerosol deposition in turbulent flow. *Aerosol Science*, **5**, 145-155.

Lynam, M. M., and G. J. Keeler, 2005: Artifacts associated with the measurement of particulate mercury in an urban environment: The influence of elevated ozone concentrations. *Atmos. Environ.*, **39**, 3081-3088.

Lyman, S. N., M. S. Gustin, E. M. Prestbo, and F. J. Marsik, 2007: Estimation of dry deposition of atmospheric mercury in Nevada by direct and indirect methods. *Environmental Science and Technology*, **41**, 1970-1976.

Marsik, F. J., and G. J. Keeler, 2005: Air-surface exchange of mercury over a mixed sawgrass—cattail stand within the Florida Everglades. *Environmental Science and Technology*, **39**, 4739-4746.

Marsik, F.J., G.J. Keeler, and M. S. Landis, 2007: The dry-deposition of speciated mercury to the Florida Everglades: Measurements and modeling. *Atmos. Environ.*, **41** 136-149.

Massman, W.J., 1998: A review of the molecular diffusivities of $H_2O, CO_2, CH_4, CO, O_3, SO_2, NH_3, N_2O, NO,$ and NO_2 in air, O_2 and N_2 near STP. *Atmos. Environ.*, **32**, 1111-1127.

Massman, W.J., 1999: Molecular diffusivities of Hg vapor in air, O_2 and N_2 near STP and the kinematic viscosity and thermal diffusivity of air near STP. *Atmos. Environ.*, **33**, 453-457.

Miller, E., P. Kelly, M. Landis, B. Hartsell, and S. Stefan, 2009: Draft data management standard operating procedure. Version 1.0 4/7/09.

Munthe, J., and W.J. McElroy, 1992: Some aqueous reactions of potential importance in the atmospheric chemistry of mercury. *Atmos. Environ.*, **Vol. 26A, No. 4**, 553-557.

Naftz, D., C. Angeroth, T. Kenney, B. Waddell, N. Darnall, S. Silve, C. Perschon, and J. Whitehead, 2008: Anthropogenic influences on the input and biogeochemical cycling of nutrients and mercury in Great Salt Lake, Utah, USA. *Applied Geochemistry*, **23**, 1731-1744.

Naftz, D., C. Fuller, J. Cederberg, D. Kerbbenhoft, J. Whitehead, J. Garberg, and K. Beisner, 2009: Mercury inputs to Great Salt Lake, Utah: Reconnaissance-phase results. *Saline Lakes around the World: Unique Systems with Unique Values. Natural Resources and Environmental Issues* Vol. **15**, Oren, A., D. Naftz, P. Palacios, and W. A. Wurtsbaugh (Eds). S.J. and Jessie E. Quinney Natural Resources Research Library, Logan, Utah, USA. 37-49. Available at: http://digitalcommons.usu.edu/nrei/vol15/iss1/1.

National Atmospheric Deposition Program (NRSP-3), 2007: NADP Program Office, Illinois State Water Survey, 2204 Griffith Dr., Champaign, IL 61820.

Pacyna, E. G., J. M. Pacyna, F. Steenhuisen, and S. Wilson, 2006: Global anthropogenic mercury emission inventory for 2000. *Atmos. Environ.*, **40,** 4048-4063.

Perrone, N., I. M. Hedgecock, and F. Sprovieri, 2008: New directions: Atmospheric mercury, easy to spot and hard to pin down: Impasse? *Atmos. Environ.*, **42**, 8549-8551.

Peters, K., and R. Eiden, 1992: Modeling the dry deposition velocity of aerosol particles to a spruce forest. *Atmos. Environ.*, **26,** 2555-2564.

Peterson, C., and M. Gustin, 2008: Mercury in the air, water, and biota in the Great Salt Lake (Utah, USA). *Science of the Total Environment*, **405**, 255-268.

Poissant, L., 2000: Total gaseous mercury in Quebec (Canada) in 1998. *The Science of the Total Environment*, **259**, 191-201.

Poissant, L., M. Amyot, M. Pilote, and D. Lean, 2000: Mercury water-air exchange over the upper St. Laurence River and Lake Ontario. *Environmental Science and Technology*, **34**, 3069-3078.

Price, H., D. A. Jaffe, P. V. Doskey, I. McKendry, and T. L. Anderson, 2003: Vertical profiles of O3, aerosols, CO and NMHCs in northeast Pacific during the TRACE-P and ACE-ASIA experiments. *Journal of Geophysical Research*, **Vol. 108 No. D20**, 8799.

Pyle, D.M., and T.A. Mather, 2003: The importance of volcanic emissions for the global atmospheric mercury cycle. *Atmos. Environ.*, **37**, 5115-5124.

Sastry, R., J. Orlemann, and P.J. Koval, 2002: Mercury contamination from metal scrap processing facilities. *Environmental Progress*, **21**, 231-236.

Schroeder, W. H., and J. Munthe, 1998: Atmospheric mercury--an overview. *Atmos. Environ.*, **32**, 809-822.

Schuster, P.F., Krabbenhoft, D.P., Naftz, D.L., Cecil, D.L., Olson, M.L., Dewild, J.F., Susong, D.D., Green, J.R., and M.L. Abbott, 2002: Atmospheric mercury deposition during the last 270 years: A glacial ice core record of natural and anthropogenic sources. *Environmental Science and Technology*, **36**, 2303-2310.

Schwarzenbach, R. P., P. M. Gschwend, and D. M. Imboden, 2003: *Environmental Organic Chemistry*. 2nd ed. John Wiley and Sons. 1312 pp.

Scudder, B.C., Chasar, L.C., Wentz, D.A., Bauch, N.J., Brigham, M.E., Moran, P.W., and Krabbenhoft, D.P., 2009: Mercury in fish, bed sediment, and water from streams across the United States, 1998–2005: U.S. Geological Survey Scientific Investigations Report 2009–5109, 74 p.

Seinfeld, J. H., and S. N. Pandis, 2006: *Atmospheric Chemistry and Physics: From Air Pollution to Climate Change*. 2nd ed. John Wiley and Sons, 1203 pp.

Selin, N. E., D. J. Jacob, R. J. Park, R. M. Yantosca, S. Strode, L. Jaegle, and D. Jaffe, 2007: Chemical cycling and deposition of atmospheric mercury: Global constraints from observations. *Journal of Geophysical Research*, **112**, D02308, doi. 10.1029/2006JD007450.

Selin, N. E., and D. J. Jacob, 2008: Seasonal and special patterns of mercury wet deposition in the United States: Constraints on the contribution from North American anthropogenic sources. *Atmos. Environ.*, **42**, 5193-5204.

Skov, H., and Coauthors, 2006: Fluxes of reactive gaseous mercury measured with a newly developed method using relaxed eddy accumulation. *Atmos. Environ.*, **40**, 5452-5463.

Slinn, S.A., and W.G.N. Slinn, 1980: Predictions for particle deposition on natural waters. *Atmos. Environ.*, **14,** 1013-1026.

Slinn, W.G.N, and S.A. Slinn., 1982: Prediction for particle deposition on vegetative surfaces. *Atmos. Environ.,* **16,** 1785-1794.

Smith, S.D., 1988: Coefficients for surface wind stress, heat flux, and wind profiles as a function of wind speed and temperature. *Journal of Geophysical Research*, **93,** 15,467-15,472.

Sprovieri, F., N. Perrione, K. Gärdfeldt, and J. Sommar, 2003: Mercury speciation in the marine boundary layer along a 6000 Km cruise path around the Mediterranean Sea. *Atmos. Environ.*, **37**, S63-S71.

St. Denis, M., X. Song, J. Y. Lu, and X. Feng, 2005: Atmospheric gaseous elemental mercury in downtown Toronto. *Atmos. Environ.*, **40**, 4016-4024.

Strode, S. A., L. Jaegle, N. E. Selin, D. J. Jacob, R. J. Park, R. M. Yantosca, R. P. Mason, and F. Slemr, 2007: Air-sea exchange in the global mercury cycle. *Global Biogeochemical Cycles*, **21**, GB1017, doi:10.1029/2006GB002766.

Stull, R.B., 1988: *An Introduction to Boundary Layer Meteorology,* Kluwer Academic Publishers, 666.

Tekran©, 2006a: Model 1130 Mercury Speciation Unit user manual, Rep. No. v. 2.02. Tekran© Incorporated, Toronto, ON.

Tekran©, 2006b: Model 1135 Particulate Mercury Unit user manual, Rep. No. v. 1.20. Tekran© Incorporated, Toronto, ON.

Tekran© 2006c: Model 2537B Ambient Mercury Vapor Analyzer user manual, Rep. No. v. 3.01. Tekran© Incorporated, Toronto, ON.

Utah Department of Environmental Quality, cited 2010: Health Effects. [Available online at http://www.mercury.utah.gov/health_effects.htm].

Utah Department of Environmental Quality, cited 2010: Mercury Toxicity. [Available online at http://www.mercury.utah.gov/mercury_toxicity.htm].

Utah Department of Health, Utah Department of Natural Resources, Utah Department of Environmental Quality, cited 2010: Utah Waterfowl Advisories. [Available online at http://waterfowladvisories.utah.gov].

Utah Department of Health, Utah Department of Natural Resources, Utah Department of Environmental Quality, cited 2010: Utah: Mercury Sampling Sites and Cunsuption Advisories. [Available online at http://www.fishadvisories.utah.gov/map.htm].

Utah Department of Health Bureau of Epidemiology Environmental Epidemiology Program, 2007: An evaluation of mercury concentrations in fish sampled from streams, lakes and reservoirs in Utah for years 2004-2006. [Available online at http://health.utah.gov/enviroepi/activities/hha/Fish%20Advisories/FishHgStatewide2007Final.pdf].

Vidic, R. D., M.T. Chang, and R. C. Thurnau, 1998: Kinetics of vapor-phace mercury uptake by vergin and sulfer-impregnated activated carbons. *Journal of Air and Waste Management*, **48**, 247-255.

Waddell, B., C. Cline, N. Darnall, E. Boeke, and R. Sohn, 2009: Assessment of contaminants in the wetlands and open waters of the Great Salt Lake, Utah 1996-2000 final report. U.S. Fish and Wildlife Service Ecological Services, Utah Field Office 2369 W. Orton Circle, Salt Lake City, Utah 84119.

Wanninkhof, R., 1992: Relationship between wind speed and gas exchange over the ocean. *Journal of Geophysical Research*, **97**, 7373-7382.

Weill-Penzias, P., M. S. Gustin, and S. N. Lyman, 2009: Observations of speciated atmospheric mercury at three sites in Nevada: Evidence for a free tropospheric source of reactive gaseous mercury. *Journal of Geophysical Research,* **114,** D14302, doi: 10.1029/2008JD011607.

Weiss-Penzias, P., and D. Jaffe, 2004: Influence of long-range-transported pollution of the annual and diurnal cycles of carbon monoxide and ozone at Cheeka Peak Observatory. J*ournal of Geophysical Research*, **Vol. 109**, D23S14

Weiss-Penzias, P., D. A. Jaffe, P. Swartzendruber, J. B. Dennison, D. Chand, W. Hafner, and E. Prestbo, 2006: Observations of Asian air pollution in the free troposphere at Mount Bachelor Observatory during the spring of 2004. *Journal of Geophysical Research,* **Vol. 111**, D10304.

Wesley, M.L., and B. B. Hicks, 1977: Some factors that affect the deposition rates of sulfur dioxide and similar gases on vegetation. *Journal of the Air Pollution Control Association,* **27**, 1110-1116.

Wesely, M.L., 1989: Parameterization of surface resistances to gaseous dry deposition in regional-scale numerical models. *Atmos. Environ.,* **23 no.6** 1293-1304.

Wesely, M.L., and B.B. Hicks, 2000: A review of the current status of knowledge on dry deposition. *Atmos. Environ.,* **34**, 2261-2282.

Wiedinmyer, C., and H.R. Friedli, 2007: Mercury emission estimates from fires: An initial inventory for the United States. *Environmental Science and Technology*, **41**, 8092-8098.

Zhang, L., S. Gong, J. Padro, and L. Barrie, 2001: A size-segregated particle dry deposition scheme for an atmospheric aerosol module. *Atmos. Environ.,* **35**, 549-560.

Zhang, L., J.R. Brook, and R. Vet, 2003: A revised parameterization for gaseous dry deposition in air-quality models. *Atmospheric Chemistry*, **3**, 1777-1804.